2008-12-17

Characterization of the Thermal Transport Through a Temporally-Varying Ash Layer

Darron Palmer Cundick
Brigham Young University - Provo

CHARACTERIZATION OF THE THERMAL TRANSPORT THROUGH A TEMPORALLY-VARYING ASH LAYER

by

Darron Palmer Cundick

A thesis submitted to the faculty of

Brigham Young University

in partial fulfillment of the requirements for the degree of

Master of Science

Department of Mechanical Engineering

Brigham Young University

April 2009

BRIGHAM YOUNG UNIVERSITY

GRADUATE COMMITTEE APPROVAL

of a thesis submitted by

Darron Palmer Cundick

This thesis has been read by each member of the following graduate committee and by majority vote has been found to be satisfactory.

Date	R. Daniel Maynes, Chair
Date	Dale R. Tree
Date	Matthew R. Jones

BRIGHAM YOUNG UNIVERSITY

As chair of the candidate's graduate committee, I have read the thesis of Darron P. Cundick in its final form and have found that (1) its format, citations, and bibliographical style are consistent and acceptable and fulfill university and department style requirements; (2) its illustrative materials including figures, tables, and charts are in place; and (3) the final manuscript is satisfactory to the graduate committee and is ready for submission to the university library.

Date

R. Daniel Maynes
Chair, Graduate Committee

Accepted for the Department

Larry L. Howell
Graduate Coordinator

Accepted for the College

Alan R. Parkinson
Dean, Ira A. Fulton College of Engineering and Technology

ABSTRACT

CHARACTERIZATION OF THE THERMAL TRANSPORT THROUGH A TEMPORALLY-VARYING ASH LAYER

Darron Palmer Cundick

Department of Mechanical Engineering

Master of Science

Ash deposits in commercial coal-fired boilers frequently pose serious maintenance challenges and decrease thermal efficiency. A better understanding of fundamental thermal transport properties in ash deposits can help mitigate their negative effects. In order to characterize the thermal properties of boiler-side deposits, this work presents a thermal transport model and in-situ measurements of effective thermal conductivity in coal ash deposits.

A simple model of the thermal transport through an ash deposit, with and with out slagging, was developed. The model approximates the deposit by dividing it into four regimes: particulate, sintered, solidified slag, and molten slag. The development of this model was auxiliary to the primary focus of this study: the in-situ measurement of effective thermal conductivity of ash deposits.

Deposits of loosely-bound particulate ash were obtained experimentally using a down-fired drop tube reactor. Pulverized coal was fired and deposits were collected on an instrumented deposition probe. An approach is presented for making in-situ measurements of the temperature difference across the ash deposits, the thickness of the deposits, and the total heat transfer rate through the ash deposits. Using this approach, the effective thermal conductivity was determined for coal ash deposits formed under oxidizing and reducing conditions. Three coals were tested under oxidizing conditions: IL #6 Crown III coal, IL #6 Patiki coal and WY Corederro coal. The WY coal exhibited the lowest range of effective thermal conductivities (k_e =0.05 to 0.175 W/m·K) while the IL #6 coals showed higher effective thermal conductivities (k_e =0.2 to 0.5 W/m·K). The IL #6 Crown III coal and the WY Corederro coal were also tested under reducing conditions. A comparison of the ash deposits from these two coals, formed under oxidizing or reducing conditions, showed larger effective thermal conductivities in deposits formed under reducing conditions. The IL #6 Crown III coal exhibited the greatest increase (as high as 50%) in k_e, under reducing conditions, over that measured in oxidizing conditions. For all of the experiments conducted, an increase in effective thermal conductivity with deposit thickness was observed, with sintering likely causing the increase in k_e.

ACKNOWLEDGMENTS

This research would not have been possible without the generous help from several faculty and fellow students. To Professors Dale Tree and Matthew Jones, I am very grateful for their encouragement, attention to detail, and instruction. It has been a privilege to be under the mentorship of my adviser, Professor Daniel Maynes. His expertise, guidance, and professionalism are truly appreciated. In particular, I acknowledge my parents for all of their support, their examples, and their leadership throughout my formal and informal education. Finally, I am grateful to Autumn for her love and understanding.

TABLE OF CONTENTS

LIST OF TABLES

LIST OF FIGURES

NOMENCLATURE

Acronyms

UDF	user defined function
SLM	standard liters per minute
ALM	actual liters per minute

Symbols

A	area
a	experimentally determined constant
b	experimentally determined constant
C_p	specific heat of air
C	pressure correction coefficient
G	mass capture fraction
Gr_L	Grashof number based on a characteristic length
g	gravitational constant
$\bar{h}$	average convection coefficient
k	thermal conductivity
k_i	thermal conductivity of the i^{th} layer
k_e	effective thermal conductivity
L	length of deposit probe test section,
L_c	characteristic length
L_s	molten slag layer thickness (at steady-state)
$\dot{m}$	mass rate
$\dot{m}''$	mass flux
$\dot{m}_{slag}$	mass flux of molten slag
n	power-law exponent
P_{calc}	calculated pressure
P_{act}	actual pressure
$\dot{Q}$	total heat transfer rate
q_{conv}	convective heat flux
q_{cond}	conductive heat flux
q''	heat flux
q''_s	heat flux at the surface
q''_x	heat flux in x-direction
R	radius
R_{air}	gas constant for air
Re_D	Reynolds number based on diameter
Re_L	Reynolds number based on a characteristic length
R_{tot}	total thermal resistance
r	radial position
T	temperature
T_{avg}	average temperature
T_{axial}	axial temperature
T_i	temperature of the i^{th} layer

T_m	mixed mean temperature
T_p	temperature of the probe
T_w, T_{wall}	temperature of the wall
T_{sur}, T_s	temperature of the surface
T_{sint}	effective sintering temperature
T_∞	temperature of the free stream fluid
η	time
t	deposit thickness
u	velocity, uncertainty
u_{max}	maximum velocity
u_{cl}	centerline velocity
$\overline{u}$	average velocity
x	position along x-axis
x_i	thickness of i^{th} ash layer
y	position along y-axis

Greek Symbols

β	expansion coefficient
μ	absolute viscosity
ν	dynamic viscosity
ρ	density
ρ_{sl}	density of molten slag
$\overline{\rho}$	average density
θ	tangential position

1 Background

Beginning with the Industrial Revolution, coal has been an important source of raw energy, literally fueling the progress of nations and technologies. It continues to be a dominant and very valuable source of energy in the modern world. Widely distributed and abundant, coal provides a significant portion of the total energy consumed in the United States. In 2007 coal-fired power plants produced approximately 48.2% of the nation's electrical power [1]. Electricity is produced when burning coal releases heat which is then transferred to water, generating steam at high temperature and pressure. This steam then drives turbines to generate electrical power. During the combustion process, inorganic constituents present in the coal form ash. A critical part of power plant operation and design depends upon the ash which unavoidably adheres to heat exchanging-surfaces, forming undesirable deposits. Ash build-up results in substantial increases in the overall thermal resistance of such heat exchangers, and it decreases efficiency and poses additional problems and challenges in power plant maintenance and design. An improved fundamental understanding of the thermal transport characteristics of ash deposits is necessary to advance the reliability, efficiency, and flexibility of this critically important energy resource. This work introduces a simplified model of the thermal transport through an ash deposit on a vertical surface. Further, it presents an

experimental method and the results of in-situ thermal conductivity measurements of coal ash deposits formed under both oxidizing and reducing conditions.

1.1 Coal as an Energy Source

Coal is mined throughout the United States. The constituents and properties of coal may vary significantly from mine to mine: therefore, the type of coal supplied to a power plant must be considered. Coal is commonly classified by its relative heating value. The four major types, ranked highest to lowest in heating value, are anthracite, bituminous, sub-bituminous, and lignite. In general, high-rank coals are common in the eastern United States, particularly throughout the Appalachian Mountains, while low-rank coals are found more commonly in the western United States. Typically, bituminous and sub-bituminous coals are fired in power plants which generate electricity. Different advantages and challenges are associated with firing either type.

To produce electrical energy a power plant burns large quantities of coal in a boiler to heat water and generate steam, which powers turbines. Before being fired inside a power plant, coal usually must be prepared. Raw fuel is commonly pulverized (average size is on the order of 75 μm) and fed into the boiler either dry or mixed with water as a slurry.

Commercial boilers (also known as combustors) operate under oxidizing conditions, meaning the coal is completely burned out in the combustion process. Large coal combustors will typically fire up to several hundred tons of coal an hour and follow a construction layout similar to Figure 1-1. Prepared coal is injected into a cavernous

boiler section through ports located in the lower walls or bottom. Here the coal rapidly mixes and reacts with air and burns, creating a region of intense heat or a “fireball.”

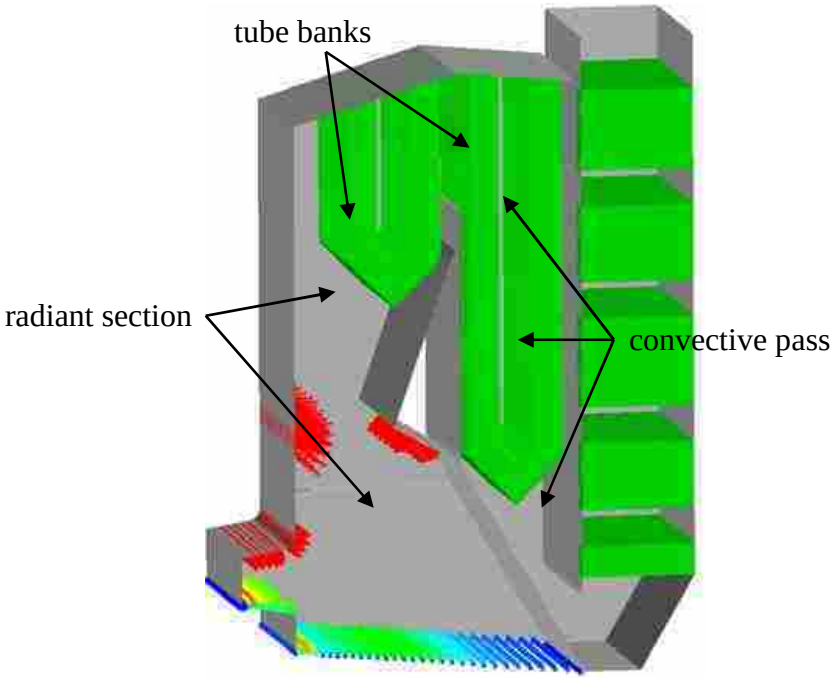

Figure 1-1. The Boiler of a Typical Coal Combustor [2]

In a combustor the boiler is made up of two major sections, distinguished by their dominant modes of heat transfer to the boiler tubes. The radiant section of the boiler is where the coal and air are injected and where the fireball resides. Here, the majority of heat energy is transferred, by radiation, from the fireball to tube banks along the walls. Combustion products are then routed through the convective pass section of the boiler where additional energy is transferred, primarily by convection, to steam flowing through multiple tube banks. The products of combustion then pass through re-heaters and economizers. Subsequently, the exhaust gases flow through fly ash collectors and scrubbers, before venting to the atmosphere. In complete combustion, the carbon and

hydrogen in the coal react with oxygen to produce carbon dioxide and water vapor. Various oxides, fine particulate material, and some heavy metals are also present in the exhaust gases. These pollutants can be removed through various control devices prior to venting. Non-combustible elements including silicon, aluminum, iron, and calcium, will condense or coalesce into "ash."

Much less common are power plants which run an Integrated Gasification Combined Cycle (IGCC). These power plants use a type of boiler known as a gasifier and are an emergent technology. They are designed to first pyrolyze the coal under fuel-rich conditions in order to produce a mixture of carbon monoxide and hydrogen gases, generally referred to as synthesis gas or "syngas." Figure 1-2 shows the cylindrical boiler portion of a typical gasifier. Coal is typically fed from the top into the main boiler section where it reacts with oxygen in a fuel-rich high-pressure environment (reducing conditions). As with combustors, heat is collected by tube banks in the boiler (or in additional downstream sections) and the resulting steam is fed to turbines for power generation. The syngas must be cleaned of ash particles before it enters a turbine combustor which operates a Brayton thermodynamic cycle to produce additional energy. With rising energy prices and renewed vigor the in development of "greener" energy, the IGCC is of particular interest as it lends itself well to the capture and sequestration of carbon dioxide [3]. The radiant section of gasifiers is usually designed to operate at temperatures above the melting point of the accumulated ash. As a result, molten ash can form viscous slag layers that flow down the interior walls of the gasifier. This slag must be removed from the bottom of the gasifier.

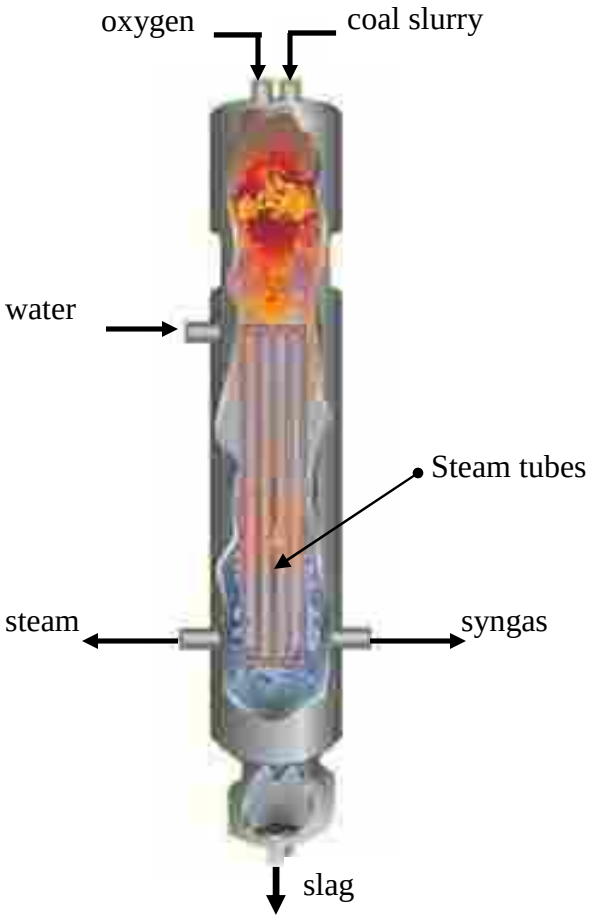

Figure 1-2. The Geometry of a Typical Boiler Section of a Gasifier [4]

1.2 Ash Deposits

In coal-fired power plants the non-combustible constituents of the fuel are a principle factor determining the boiler size, combustion reactants-to-steam heat transfer characteristics, and boiler-side surface corrosion behavior [5]. Inorganic solids in the fuel may be converted to a gas or liquid when burned, but the majority of the mass remains in the solid phase. The combination of all condensed and solid phase material remaining unburned is classified as ash. These deposits collect on refractory surfaces and on boiler tubes (see Figure 3-1). The radiant and convective pass sections of a combustor are

particularly sensitive to the build up of ash deposits [6]. Accumulated ash on boiler tubes and walls creates a variety of problems including reduced heat transfer, increased corrosion, and flow blockage. Several methods are necessarily employed in reducing and removing ash deposits within coal-fired power plants. In combustors, deposits may be forcefully removed by "soot blowing" (the forceful removal of ash by pressurized air or steam) or they may be made to detach by methods utilizing thermal shock. If removal by soot blowing or by other methods is unsuccessful, the resulting large deposits can increase the frequency of planned shut-downs or even produce catastrophic failures if they suddenly detach and fall, causing damage to steam tubes or boiler walls [6]. Gasifiers are typically designed to slag, with the molten ash flowing out the bottom. Excess slag, however, hastens corrosion, increases blockage, and decreases efficiency [5]. To better understand and control ash and its effects within boilers, the properties and behaviors of ash deposits have been studied by many researchers in industry and academia. In the continuing effort to improve heat transport and decrease maintenance costs, understanding the thermal properties of ash deposits is of acute interest. These properties include thermal conductivity and surface emittance.

1.3 Motivation

Characterizing the thermal transport through coal ash deposits is a major step toward mitigating their effects through better boiler maintenance and design. Coal combustors and gasifiers are capable of operating throughout a wide range of temperatures and fouling and slagging conditions. Maximum efficiency, however, is obtained only over a narrow band of conditions. Practical boiler operation inevitably

deviates from this narrow peak-efficiency range because of necessary maintenance and limitations in both thermal transport and materials. Thermal transport in boilers is directly influenced by the surface emittance and thermal conductivity of ash deposits. Consequently, boiler size and design is significantly influenced by the effects of these deposits [5, 7, 8]. The ability to model the thermal transport through ash deposits is essential for boiler design optimization and for efforts aimed at improving boiler reliability, flexibility, and overall efficiency.

Experimental measurements can provide fundamental understanding of the thermal conductivity of ash deposits. The formation of deposits in combustors and gasifiers is thought to be sensitive to their surroundings, including differences respective of oxidizing and reducing conditions [7, 9, 10]; consequently, experimental data for both conditions are needed to accurately characterize the deposits. Further, because of the sensitivity of ash deposits to their environment, in-situ measurements made under oxidizing and reducing conditions are necessary to better understand the effective thermal conductivity of these deposits.

1.4 Research Objectives and Contributions

The objectives of this work are to: 1) develop a conceptual and numerical model of the thermal transport in a growing ash deposit; 2) exercise the model with the commercial modeling package FLUENT for a typical combustion scenario; 3) develop an experiment to measure in-situ effective thermal conductivity; and 4) obtain in-situ measurements of effective thermal conductivity for different coals under oxidizing and reducing conditions.

The thermal transport model characterizes an ash deposit by multiple regimes (or sections), upon which effective thermal conductivity and other properties are dependent. By casting the model as a User Defined Function (UDF), it may be integrated with the commercial modeling package FLUENT and used to predict the heat flux and surface temperature profiles in a scenario simulating a typical coal boiler. The experimental work focuses on collecting ash deposits to make in-situ measurements of temperature, heat flux, and thickness in order to obtain the effective thermal conductivity. Three types of coal are utilized.

This work presents three primary contributions to the understanding of the thermal transport through ash deposits:

1. A thermal transport model of the vertical wall of the radiant section of a boiler with a developing ash deposit, including a molten slag layer.
2. An in-situ experimental approach to measure the effective thermal conductivity of a growing ash deposit. The approach is employable for both oxidizing and reducing conditions.
3. Effective thermal conductivity data acquired by using the in-situ experimental approach (2) for three coals in oxidizing conditions and two coals in reducing conditions.

1.5 Delimitations

The limitations in the scope of this work are here described. The thermal transport model does not develop an expression for the ash deposit thermal conductivity; rather, this property depends on ash morphology and enters into the model as an input.

While it does account for energy transfer by convection and radiation (required as inputs), the model does not specifically develop these modes of transport. The model also does not calculate the actual deposition or any erosion of the ash. In its present state, the model must run in conjunction with FLUENT and is not a stand-alone program.

Experiments conducted are of ash deposits obtained from firing pulverized coal only. Further, the experimental portion of this study involves only rigid "particulate" ash deposits with no slag layers. Lastly, all of the data were collected for fairly thin horizontal deposits collected on a cylindrical probe.

1.6 Overview

This document explains a model of thermal transport through an ash deposit. It also provides the experimental approach and measurements of the thermal conductivity of deposits, formed in both oxidizing and reducing conditions. First, Chapter Two reviews relevant prior work and summarizes previous research on the modeling, prediction, and the experimental measurement of thermal conductivity. Chapter Three comprises the analytical and computational work that models the thermal transport through a temporally-varying ash deposit. An analysis of thermal transport is provided, followed by the method for constructing the model. Details of the development of the model as a User Defined Function and its integration with FLUENT are discussed. An illustrative scenario, in which the model is implemented, and the results from the UDF are presented. Chapter Four addresses the experimental portion of this work, giving an overview of experimental facilities and equipment. This chapter details the set-up and instrumentation, and it explains the experimental procedure. The method of analysis of

the raw data and the calculations of effective thermal conductivity are also provided. Chapter Five presents the experimental results. Finally, conclusions are discussed in Chapter Six.

2 Prior Work

A review of prior work draws attention to the complexity of ash deposit thermal transport properties and the limited ability of available models to adequately characterize ash deposits, including slag layers. Additionally, because of the sensitivity of ash deposits to their environments, there is a need for in-situ data of the thermal transport properties for each type of fuel to be better utilized. The literature review focuses on previous studies of thermal transport models and on experimental measurements of effective thermal conductivity.

2.1 Modeling of Thermal Transport through Coal Ash Deposits

A significant amount of work has previously been done in modeling and predicting thermal transport through ash deposits. Typically, a deposit with known properties is layered on top of a substrate of known temperature. Given appropriate boundary conditions and the effective ash thermal conductivity, the net heat flux through the deposit may be determined.

Central in a thermal transport model is the determination of the ash deposit properties, in particular, the thermal conductivity and surface emittance. These thermal properties are dependent upon ash deposit morphology, chemical composition, and temperature. A larger ash deposit can exhibit significant variations in morphology (i.e.

varying degrees of sintering and slagging) and temperature; therefore, the changes in the properties of the deposit need to be accounted for. Fully comprehensive ash deposit models, combining deposition mechanisms, morphological variations, and complete thermal transport, are notably complex due to the coupling of the governing equations for the balance of mass, momentum, and energy. This complexity has been worked around somewhat by considering only thinner, or at least practically uniform, deposits (of all one morphology) and also by dividing the ash layer into effective sections or "regimes," each with distinct properties. Robinson and coworkers at Sandia National Labs developed a two-layer model consisting of unsintered and sintered regimes [11]. By using constant properties in two distinct structures of ash, they modeled the effective thermal conductivity of sintered ash deposits and also used the model to set bounds on the effective thermal conductivities expected. Researchers at Reaction Engineering International have addressed the challenges of determining ash slag characteristics and boiler performance by creating a computational model that utilizes a two-layered ash deposit, including a slagging layer [8, 12, 13]. The model consists of solidified slag and molten slag layers over a refractory lining. Thermal conductivities and other properties for the two layers are obtained from experimental data and input to the model.

In an effort to characterize the morphological and thermal changes throughout an ash deposit, many studies have focused on developing models for inter-particle thermal conductivity by examining the deposit microstructure [14]. Such particle-level modeling has been researched extensively by examining packed beds and considering the structure and the extent of porosity in two-phase or two-material systems [15]. However, these

systems are limited in their ability to approximate an ash deposit with varying degrees of sintering and slagging.

Indeed a more elegant model of a deposit would be one that exhibits variable thermal properties throughout the ash deposit. One approach toward accomplishing this is to correlate variations in the deposit to experimental data, rather than dividing the ash deposit into different regimes with constant properties. In his work, Anderson has developed a model incorporating a variable effective thermal conductivity for non-slagging deposits. Within his model, the thermal conductivity is a function (correlated to experimental data) of temperature and therefore a function of the degree of sintering in the deposit as a whole [5].

A detailed model for the effective thermal conductivity throughout an entire ash deposit, which includes layers ranging from unsintered to molten slag, is currently not practical. This is because purely analytical models are limited by the complexity of the continuous variation in morphology and thermal properties throughout the ash deposit. Models of ash deposits utilizing experimental data are inhibited by the lack of sufficient property data available for the full range of the deposit's characteristics, including the transition from stationary to molten ash layers. This work proposes a method of approximating ash deposits by incorporating additional regimes. Specifically, the deposit is characterized into four regimes: particulate, sintered, solidified slag, and molten slag. This simple model accommodates stationary and slagging ash deposits by extending the idea of using multiple regimes. By approximating ash ranging from stationary particulate layers to flowing molten slag layers, this approach is a step toward better modeling the conductive thermal transport in morphologically complex ash deposits.

The usability of a model is important for any practical implementation. A thermal transport model that can be integrated with additional thermodynamic or hydrodynamic models within a CFD or other multi-physics modeling package will prove more useful than one which is stand-alone. Kaer has integrated a model for the thermal conductivity of ash deposits with combustion models in FLUENT. He developed a model of the thermal resistance due to a homogeneous ash deposit, the growth of which is governed by an additional deposition model [2]. The model aided in predicting the heat flux and temperature distributions in a combustor boiler. Additional work by Kaer similarly integrated a model for sintered deposits using two-layers (regimes). Engineers at Reaction Engineering International have produced two-layer models for steady-state slag deposits integrated within commercial CFD code in FLUENT [2, 8].

This work presents a thermal transport model for morphologically complex ash deposits that is executed by FLUENT. This model consists of four regimes. Integration with FLUENT facilitates the model's ease of use. Additionally, integration allows the thermal transport model to couple with other models which govern ash deposit properties. This model is intended as a framework for the future integration of more rigorous models of ash deposit deposition, thermal conductivity, and emittance.

2.2 Experimental Measurements of Thermal Conductivity

The effective thermal conductivity of ash deposits is highly dependent upon the composition, morphology, and temperature of the ash. Consequently, several experimental studies have been conducted to characterize these properties in deposits formed by firing coal. Deposited ash will generally sinter and become denser with time,

depending heavily upon temperature, and it has been shown that internal radiation becomes significant at higher temperatures and must be accounted for in determining the overall effective thermal conductivity [7, 16]. Anderson et al. and Rezaei et al. extensively investigated the influence of temperature and consequent sintering on ash deposits [10, 17]. Measured values for thermal conductivity have been observed to increase by more than an order of magnitude due to sintering behavior and elevated temperatures [7, 10, 11, 16]. Additionally, the emittance of ash layers can vary widely, also depending on the deposit properties. Due to the large range of variation in ash deposits, experimental measurements are necessary to observe coal-specific and condition-specific behaviors. The characterization of the thermal properties of additional types of coal would therefore extend the knowledge base to those specific coals.

The majority of previous experiments have involved the ex-situ examination of changes in effective thermal conductivity, with in-situ experimentation on deposits uncommon. Hwang et al. and Butler et al. [18, 19], have studied heat fluxes and surface temperatures, shedding light on trends and profiles as might be found in typical coal-fired boilers. Accurate characterization of the thermal properties of ash deposits is quite complex due to the strong and coupled dependencies on thermal and physical properties. Robinson et al. have presented cases for the importance of in-situ examination to determine accurate deposit properties under operating-boiler conditions [11]. Ash deposit morphology, in particular, is very complex and strongly influences the effective thermal conductivity. Morphologic behavior itself is highly dependant upon thermodynamic, hydrodynamic, and geometric conditions. As a result, ex-situ samples exhibit subtle yet influential differences from their in-situ counterparts [9]. Researchers

at Sandia National Laboratories have successfully measured in-situ thermal conductivity for a handful of coal and biomass blends in oxidizing conditions [9, 11]. However, in-situ experiments are relatively few. Additionally, there is very little experimental data for deposits formed and measured in-situ under reducing conditions. A better fundamental understanding of thermal conductivity will result from further studies of in-situ deposits. This work contributes an experimental approach to obtain in-situ measurements, and it presents the results of effective thermal conductivity for ash deposits obtained under oxidizing and reducing conditions for three different types of coal.

3 Modeling the Thermal Transport through a Growing Ash Deposit

A model was developed in a parallel effort with the primary focus of this work, the experimental measurement of effective thermal conductivity of ash deposits. This chapter presents a simplified model for the thermal transport through a growing ash deposit on a boiler wall. The model utilizes a multi-regime ash structure to better capture changes in the ash morphological and thermal properties. It is developed as a User Defined Function, compatible with FLUENT, to aid in the prediction of surface temperature and heat flux profiles typical of coal-fired boilers.

A simplified one-dimensional conduction model has been developed to characterize the heat transport through a growing ash deposit (conjugate heat transfer is neglected in the model). The model may aid in the design of power plants and in understanding how ash deposits influence the overall thermal transport. The thermal transport from the fireball to an array of closely-spaced water tubes was modeled by one-dimensional heat transfer through a composite thermal resistance. This thermal resistance path consisted of conduction through the tube wall and layers of ash, and it included convective and radiative transport at the ash deposit surface.

Figure 3-1 illustrates an array of tubes positioned closely to one another. This configuration, common in coal-fired power plants, is called a tube “bank” and its

geometry is such that it may be modeled effectively as a wall or flat surface. This approximation was made by considering that the tubes' radii are much smaller than their lengths and their collective width. Therefore, heat transfer to this surface was considered one-dimensional in this model.

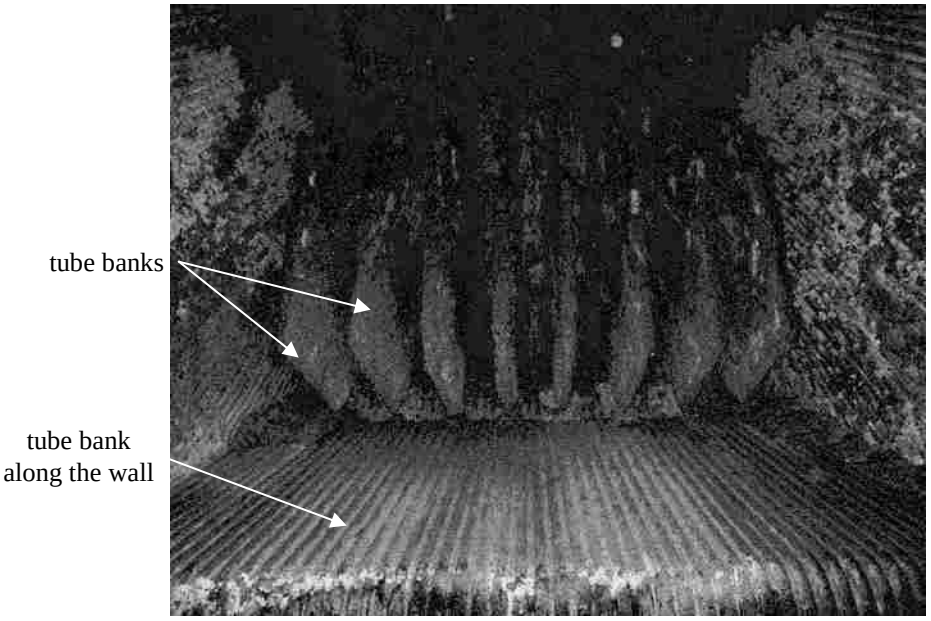

Figure 3-1. Tube Banks with Ash Deposits Inside a Boiler; Pictured from the Bottom Looking Up along the Wall. Photo by Lars Fenger [2]

An initially clean surface will collect ash and become increasingly thermally insulated. The model considered the ash build-up and predicted the temporal behavior of temperature and total heat flux. Deposits on heat transfer surfaces begin with very porous layers of loosely-bound particulate material. As the deposits grow, the layers of ash nearest the deposit surface will increase in temperature and begin to sinter. While sintering can increase thermal conductivity locally, the net thermal resistance through the growing ash deposits will generally increase. If the deposits continue to grow, the

deposit surface can eventually reach an effective melting point of the ash constituents, and a molten slag layer will form [7]. Further deposition and thickening of the molten slag layer can insulate deeper levels of molten slag, causing these deeper slag layers to re-solidify. In this model, the gradation of deposit morphology (and consequently thermal properties) was approximated by dividing the deposit into four primary "regimes": particulate, sintered, solidified slag, and molten slag. Figure 3-2 illustrates these regimes schematically.

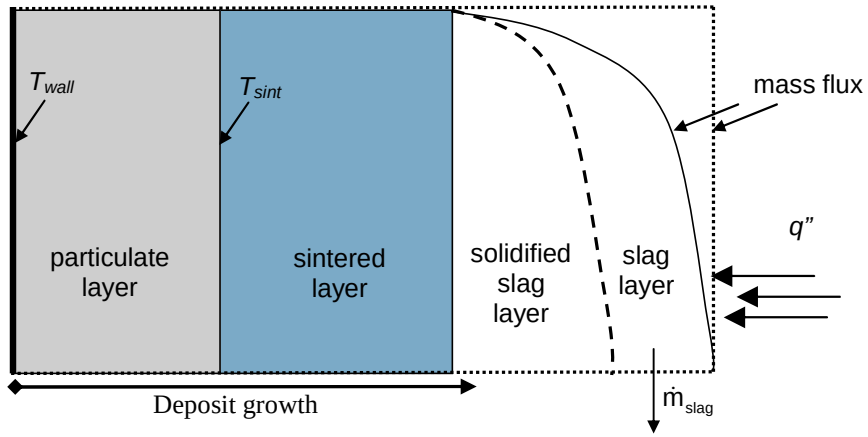

Figure 3-2. Ash Deposit 4-Layer Model

The transition between regimes in the model was defined by an effective temperature at each regime boundary (i.e. effective "sintering" and "slagging" temperatures). Ash in each regime was characterized by averaged properties typical of that layer. Values for these properties, including density, emittance, and thermal conductivity, were obtained from the literature and supplied as inputs; they were treated as constants throughout each regime. The model requires other inputs and assumptions including a specified wall (tube bank) temperature, a specified uniform mass deposition

rate for each regime, and specified boundary temperatures of the surrounding domain (i.e. the top, bottom, and center of the boiler). All of the required inputs are given in Table A-1 in Appendix A.

3.1 Analysis of Ash Deposit Thermal Transport

Consider an ash deposit growing on the vertical side-wall of a boiler as illustrated in Figure 3-2 and described previously. The thickness, $\Delta x_i(y)$, of the ash layer that forms in a time step, Δt, is determined by the local mass flux reaching the surface and the ash deposit density:

$$\Delta x_i(y) = \frac{\dot{m}'' G(\Delta t)}{\rho_a} \qquad \textbf{(3-1)}$$

ρ_a is the ash deposit density, G is the captured mass fraction, and $\dot{m}''$ is the local deposition mass flux. At any instant the total heat flux through a growing ash deposit is governed by both radiation and convection on the boiler side of the ash deposit surface and by conduction through the deposit to the wall. The ash will exhibit variations in morphology throughout the entire deposit. The thermal conductivity, which is strongly dependent upon morphology and temperature, will in turn exhibit spatial variations. Assuming a quasi-steady thermal transport and neglecting conjugate heat transfer (i.e. heat conduction in the transverse direction) the wall-normal heat flux through the ash layer may be expressed by Eq. (3-2).

$$q''_x(y) = \frac{1}{R''_{tot}(y)}\left(T_w - T_{sur}(y)\right) = \sum_i \frac{k_i}{\Delta x_i(y)}\Delta T_i \qquad \textbf{(3-2)}$$

$R''_{tot}(y) = \sum_i \Delta x_i(y)/k_i$ is the total thermal resistance to heat transfer in the *x*-direction, and Δx_i, ΔT_i, and k_i are the respective thickness, temperature difference across, and thermal conductivity of the i^{th} layer of the ash deposit. Summation of the resistances of each layer, over the entire thickness of the ash deposit, yields the local total thermal resistance. In the present model the thermal conductivity, k_i, is assumed to be constant for each Δx_i layer. T_w is the temperature of the vertical wall, and $T_{sur}(y)$ is the surface temperature of the deposit. The heat flux to the ash deposit surface consists of a convective portion and a radiative portion:

$$q''_s = q''_{conv} + q''_{rad} \qquad \textbf{(3-3)}$$

This flux depends upon the combustion and local flow characteristics. Provided that a wall temperature is specified, the heat flux is determined by FLUENT's solution to the Energy Equation. The total surface-normal heat flux derived from FLUENT, q''_s, and the conductive heat flux described by Eq. (3-2) must be equal, under the assumption of a quasi-steady state condition with negligible conjugate heat conduction.

3.2 Analysis of Steady-State Slagging

An ash deposit grows due to entrained ash adhering to the wall. A constant and spatially uniform ash mass flux, $\dot{m}''$, will produce a deposit thickness which increases

linearly with time, as expressed by Eq. (3-1). This model is valid for an ash deposit in the solid phase. However, under slagging conditions, a molten surface layer will form and flow due to gravity as illustrated in Figure 3-3, and the layer will eventually reach a steady-state.

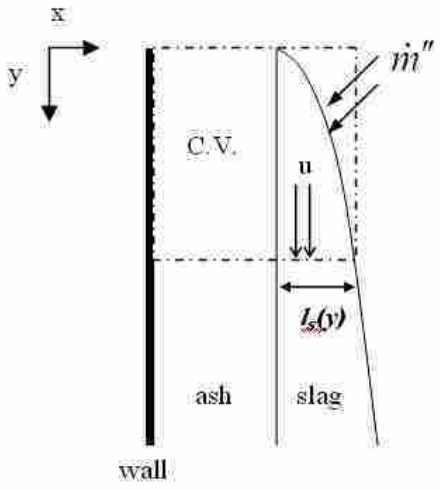

Figure 3-3. Ash Deposit Mass Balance Control Volume

Due to the high viscosity and low velocities of the slag, the Reynolds number is small and the flow is in the creeping regime. Consequently the nonlinear convective terms from the differential equations of motion exert negligible influence. Further, for steady-state conditions the unsteady terms may be neglected. Under these conditions the *y*-component (direction parallel to the wall) of the Navier-Stokes equations reduces to:

$$\frac{\partial}{\partial x}\left(\mu \frac{\partial u}{\partial x}\right) = -\rho_{sl} g \qquad \textbf{(3-4)}$$

u is the local slag velocity in the y-direction, ρ_{sl} is the slag density, and g is the gravitational constant. The average viscosity of the slag layer, μ, was determined using an Urbain viscosity model, where the viscosity was evaluated at the average slag temperature [20].

$$\mu = aTe^{\left(\frac{b\cdot 10^3}{T}\right)} \tag{3-5}$$

The constants a and b are determined from the chemical composition of the coal.

Assuming, at any y-location, that the slag viscosity and density are constant at the average slag temperature, Eq. (3-4) can be integrated twice to obtain

$$u = \frac{\rho_{sl} g}{\mu}\left(-\frac{1}{2}x^2 + x l_s(y)\right) \tag{3-6}$$

where $l_s(y)$ is the height-dependent (y-direction) steady-state thickness of the slag layer. Assuming that all further deposited ash on a molten slag layer will also melt, a mass balance requires that the total ash deposited on the slagging layer be balanced by the total mass flow of slag downward. For a constant deposition rate over the control volume region of interest (see Figure 3-3), this balance may be expressed by Eq. (3-7).

$$\int_0^{l_s(y)} \rho_{sl} u dx = \dot{m}'' y \tag{3-7}$$

Upon substitution of the parabolic velocity distribution (Eq. (3-6)) into equation (3-7) and integrating, the height-dependent steady-state thickness of the slag may be expressed as

$$l_s(y) = \left(\frac{3\mu \dot{m}'' y}{(\rho_{sl})^2 g} \right)^{1/3} \quad \textbf{(3-8)}$$

Substituting $l_s(y)$ from Eq. (3-8) into Eq. (3-6) and then evaluating Eq. (3-6) at $x = l_s(y)$ (at the surface) yields the maximum slag velocity as a function of y, μ, ρ_{sl}, and $\dot{m}''$:

$$u_{\max} = \frac{(3\dot{m}'' y)^{2/3}}{2(\mu \rho_{sl}/g)^{1/3}} \quad \textbf{(3-9)}$$

Also, the average slag velocity may be expressed by Eq. (3-10).

$$\bar{u} = \frac{(3\dot{m}'' y)^{2/3}}{3(\mu \rho_{sl}/g)^{1/3}} \quad \textbf{(3-10)}$$

These equations allow a steady-state molten slag thickness to be determined as a function of temperature and vertical position. The model uses this slag thickness profile to calculate the time-of-formation and temperature distribution of the molten and solidified slag layers.

3.3 Thermal Transport UDF Development and Implementation

A commercial CFD program (FLUENT) was used to model a simplified scenario exhibiting an ash layer with slagging, where high heat transfer rates are achieved primarily through radiation. The thermal transport model was embodied as a UDF which can be "hooked" to FLUENT. The Thermal Transport UDF was written to model the effects of a developing ash deposit on a surface or wall. A properly compiled and integrated UDF may be called and run within FLUENT's own solver.

3.3.1 Overview of the Thermal Transport UDF

Within the computational model, the ash layers do not directly exist in FLUENT. Rather, they exist in the Thermal Transport UDF, which conveys their cumulative thermal effects to FLUENT via surface temperature information. The Thermal Transport UDF solves the steady-state thermal transport through layers of ash. The model adds layers to simulate the growth of an ash deposit with time. Using the ash surface temperature as a boundary condition, FLUENT iterates through its own steady-state energy solver at each time step and returns a solution to the net heat flux to the same boundary. The heat flux calculated by FLUENT is then passed back to the UDF and used to calculate a surface temperature of the developing ash deposit (Eq. (3-2)). This newly-calculated surface temperature is compared to the surface temperature provided as an input to FLUENT, and if needed, the surface temperature is updated and again passed to FLUENT as a boundary condition for successive iterations. In this way, by the exchange of surface temperature and net heat flux, the Thermal Transport UDF and FLUENT are

coupled. Figure 3-4 diagrams the overall flow of information and the coupling of FLUENT and the Thermal Transport UDF required to obtain a solution.

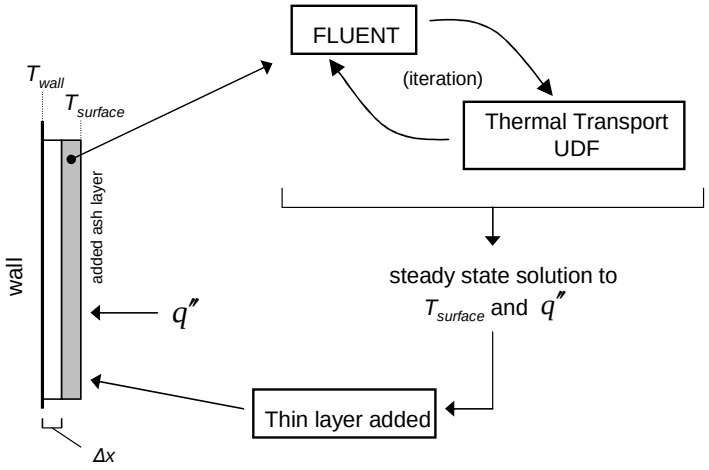

Figure 3-4. Schematic Illustration of the Numerical Iteration of the Thermal Transport Model with FLUENT

3.3.2 Operation of the Thermal Transport UDF

Before the Thermal Transport UDF begins, required inputs must be made available in FLUENT. This is done by executing a separate UDF which reads the input constants from a text file and then stores them in user-defined memory within FLUENT. These constants include the emittance, density, and effective thermal conductivity for each of the four ash deposit regimes (see Table A-1 in Appendix A). The Thermal Transport UDF begins by first computing the heat fluxes and deposit thicknesses at the particulate/sintered regime transition and at the sintered/slag regime transition. To accomplish this, the Thermal Transport UDF simulates a complete particulate layer which has just reached the sintering transition point. The effective sintering temperature is assigned to the boundary. FLUENT uses the boundary temperature to compute a total

heat flux, based on solution to the Energy Equation. This heat flux is the heat flux through the entire particulate regime, and it is used to compute the thickness of the deposit at this point (when a complete particulate layer exists) by Eq. (3-2). This thickness represents the maximum particulate layer thickness. Similar steps are followed using the transition temperature, from a sintered ash deposit to a slagging ash deposit, to determine the maximum thickness of the sintered regime. The Thermal Transport UDF assigns the effective slagging temperature to the boundary, simulating complete particulate and sintered layers of ash. A solution to the heat flux through the complete particulate and sintered ash layers is obtained by solution to the Energy Equation in FLUENT. The heat flux through and temperature difference across the layers are used to compute their cumulative thickness by using Eq. (3-2). The time required to form the particulate and sintered layers is subsequently computed from their thicknesses by using Eq. (3-1) and an input mass deposition flux rate, $\dot{m}''$.

Next, the steady-state slag surface temperature and the heat flux for a fully developed molten slag layer (on top of particulate and sintered layers) are computed by iteration. While the particulate and sintered layers are considered static, the slag layer is molten and will run down a vertical or inclined boundary. Consequently a mass balance must be used in addition to an energy balance in order to determine the surface temperature and heat flux. A surface temperature of the slag layer is initially guessed, and a heat flux will be returned by FLUENT. Using a modified Urbain viscosity model (Eq. (3-5)) an average viscosity for the slag layer is calculated using the average temperature of the slag layer. A mass balance may be used to yield the layer's thickness, by Eq.(3-8), and the slag surface temperature is then recalculated. Comparison of the

previously input and recalculated surface temperatures drives successive iterations to convergence. The result is a known surface temperature and a known net heat flux (both functions of vertical position) of the steady-state slag layer. At this point the full deposit is characterized piece-wise, with known regime transition temperatures and known heat fluxes and thicknesses of complete particulate, sintered, and molten slag regimes, with the exception of the solidified slag layer.

After determining the heat flux, surface temperature, thickness, and elapsed time for the regime transition points and the steady-state slagging layer, the Thermal Transport UDF starts with a clean wall (boundary) and allows an ash deposit to develop. The Thermal Transport UDF monitors and records the surface temperature, heat flux, thickness, and elapsed time data as the deposit develops. To grow the deposit and obtain this data within the regimes themselves, small time steps are specified and corresponding layers of ash are deposited, as described by Eq. (3-1). Individual layers of ash are considered "thin", meaning that the thermal mass of each added layer is negligible. An analysis of the Fourier number shows a rate of thermal transport much greater than the rate of energy storage for layers of ash added in the model. Therefore, the solution to energy transport by steady-state analysis is appropriate in the model. The steady-state heat transfer is solved for each added layer by again assuming a surface temperature and iterating on Eq. (3-2), with FLUENT's solver. During the iteration process, the surface temperature is recalculated and compared to the temperature of the previous iteration. Adjustments are made to the surface temperature in successive iterations until convergence is reached, and then another layer of ash is added to the deposit and the

process repeated. In this manner, the Thermal Transport UDF "marches" through time and data is recorded, upon convergence in surface temperature, for each layer.

The process of adding layers (time steps) and then solving for the steady-state conditions continues until the surface reaches the slagging temperature, when transition to the molten slag regime occurs. For simplification of the required calculations, the slag layer is computed similar to the particulate and sintered layers in that the molten slag is treated as a rigid layer; accumulating ash remains stationary in the "molten" slag layer although it is given the thermal properties of molten slag. The slag layer grows uniformly until it reaches a steady-state thickness described by Eq. (3-8).

Importantly, the addition of slag can further insulate the previously deposited layers of ash beneath it, including previous molten slag layers, and some of this molten slag will cool below the effective slagging temperature and solidify. In the model, when the deposit surface transitions to molten slag, the solidified slag layer grows simultaneously with the molten slag layer. Upon advancing one time step, all of the added mass is modeled as a molten slag layer. Iteration on Eq. (3-2) results in a converged solution to the surface temperature and heat flux for the added molten slag layer.

The extent of the frozen slag layer is then determined. First, all of the mass added in a time step is considered molten slag, according to Eq. (3-1). Assuming that the density of the solidified slag and molten slag layers is equal, a mass (per unit area) balance was written as

$$m'' = \rho_{solid} t_{solid} + \rho_{slag} t_{slag} \quad \textbf{(3-11)}$$

where ρ and t are the density and thickness of the respective regimes. The thickness of the solidified slag layer was then computed by Eq. (3-12) which utilizes the solidified slag thickness known from the previous time step.

$$t_{slag} = \frac{m'' + \rho_{solid} t_{solid}}{\rho_{slag}} \quad \textbf{(3-12)}$$

The newly deposited molten slag layer will insulate some of the deeper layers of the molten slag regime, resulting in unknown thicknesses of the solidified slag and molten slag regimes for the current time step. The solidified slag regime thickness can also be determined by equating the heat flux through the slag layer and the heat flux through the composite sintered, solidified slag, and molten slag layers:

$$q'' = \frac{1}{\left(\frac{t_{slag}}{k_{slag}}\right)}\left(T_s - T_{slag}\right) = \frac{1}{\left(\frac{t_{slag}}{k_{slag}} + \frac{t_{solid}}{k_{solid}} + \frac{t_{\sin t}}{k_{\sin t}}\right)}\left(T_s - T_{\sin t}\right) \quad \textbf{(3-13)}$$

Solving Eq. (3-13) for t_{slag} yields the solidified slag regime thickness in terms of the temperature difference across the sintered regime, the thickness and effective thermal conductivity of the sintered regime, and the heat flux through the deposit for the current time step:

$$t_{solid} = k_{solid}\left(\frac{T_{slag} - T_{\sin t}}{q''} - \frac{t_{\sin t}}{k_{\sin t}}\right) \quad \textbf{(3-14)}$$

The heat flux for the current time step, in Eq. (3-14), is obtained from FLUENT's solution to the Energy Equation, which in turn is computed from a deposit surface temperature. The molten slag regime thickness computed using Eq. (3-12) is used with the heat flux obtained by FLUENT to re-calculate the deposit surface temperature:

$$T_s = \frac{q'' t_{slag}}{k_{slag}} + T_{slag} \quad \textbf{(3-15)}$$

The new deposit surface temperature obtained by Eq. (3-15) is passed to FLUENT and an updated heat flux computed. The updated heat flux is used in Eq. (3-14) to compute an updated solidified slag regime thickness, t_{solid}. The updated solidified slag regime thickness is then inserted into Eq. (3-12) to obtain an updated molten slag regime thickness. Iterations on Eqs.(3-12), (3-14), and (3-15) continue until a converged molten slag regime thickness is obtained. This converged molten slag regime thickness will be smaller than the molten slag regime thickness of the previous time step plus the thickness of the molten slag layer added for the current time step. The difference between the two thicknesses is equivalent to the solidified slag layer thickness added for the current time step. This additional thickness of the solidified slag layer is added to the existing solidified slag layer regime thickness. A result of the simultaneous growth of the solidified slag and molten slag regimes is that the physical location of the interface between the slag regimes moves. The process of adding molten slag layers and

determining the thickness of the frozen slag layer continues until the molten slag layer reaches the full steady-state thickness determined previously in the UDF (see Eq. (3-8)). When the steady-state slag layer thickness is reached, the ash deposit is considered fully developed and the model is complete. Final results are written to a file. Details of how to execute the Thermal Transport UDF in FLUENT, a more detailed flow chart of the UDF, and the source code are provided in Appendix C.

3.4 Assumptions and Limitations of the Thermal Transport UDF

In the development of the ash deposit, it is assumed that the particulate and sintered portions of the deposit are rigid and that once formed, a layer will not change morphological state (regime) except in the case of solidifying slag layers. Also, the ash deposit is not created directly in FLUENT; it exists only in the Thermal Transport UDF. This means that the ash deposit cannot influence the flow characteristics in the domain in FLUENT. Among the required inputs for the Thermal Transport UDF are known (and constant) deposition rates for each of the regimes. The UDF uses these values to initially compute the steady-state regime layer thicknesses before growing the ash deposit. This was done to facilitate the ease of convergence of the heat flux and thickness for each regime transition. This requirement, of known deposition rates, could be problematic if the UDF is coupled to a model of the deposition rate. The Thermal Transport UDF could be modified to compute the regime transitions as the deposit grows, thus eliminating this particular limitation.

Several important conditions are required in employing the Thermal Transport UDF. The operator may exercise the Thermal Transport UDF on any straight one-

dimensional boundary; the UDF will not function on curved surfaces or on two or three-dimensional surfaces. The boundary may lie in any orientation within the x-y plane. The boundary must also be stationary.

It is important to note that in many real-world cases, a slagging deposit is not reached. The Thermal Transport UDF is designed to continue iterating until stead-state slagging condition exists. Early termination of the program may be required when no slag layer is desired. In cases where slagging is not wanted, other conditions, such as deposit thickness or surface temperature, may be monitored to determine how long the UDF is allowed to run.

3.5 Illustration of the Thermal Transport UDF

A simple scenario was created to exercise the Thermal Transport UDF and to illustrate its functionality. A rectangular domain was considered which represents the radiant boiler portion of a gasifier. Figure 3-5 illustrates the geometry and boundary conditions of the scenario considered. The domain boundaries were set to fixed temperatures, with the centerline boundary exhibiting a linearly varying temperature distribution ($T_{centerline} = 7.5y + 1700$) (Kelvin), approximating a large fireball source near the bottom of the gasifier. A quad mesh (3200 cells total) was constructed over the domain with greater refinement near the wall boundary whereon the UDF operates.

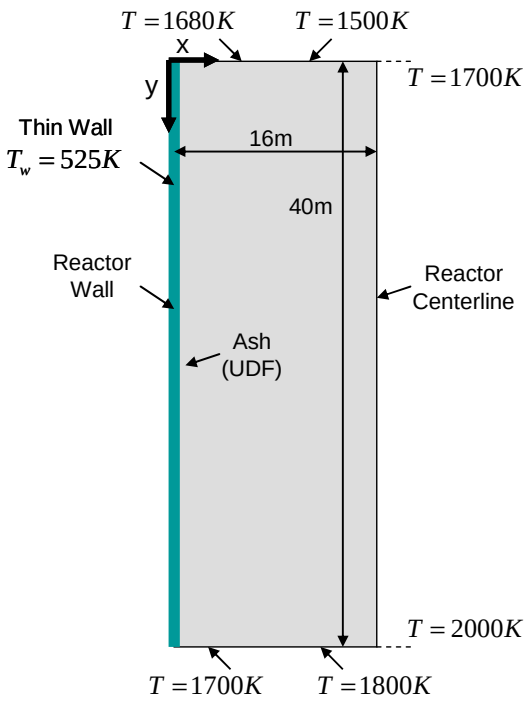

Figure 3-5. The Domain for the Illustrative Scenario in FLUENT

For this simple case, the domain is considered quiescent (convection is turned off), and heat transfer to the deposit occurs dominantly by radiation. Consequently, only the energy equation is solved in FLUENT. The gas in the domain is set to be air. Other inputs to the UDF are supplied by a text file and are listed in Table A-1. Details of how to execute the Thermal Transport UDF in FLUENT are discussed in Appendix C.

The UDF successfully produced spatial and temporal profiles for the deposit surface temperature and deposit thickness on the inside wall of a gasifier. Data were generated for the deposit thickness, temperature, and net heat flux. The ash surface temperature distribution along the wall, at four instances in time, is shown in Figure 3-6 as a function of vertical position *y*:

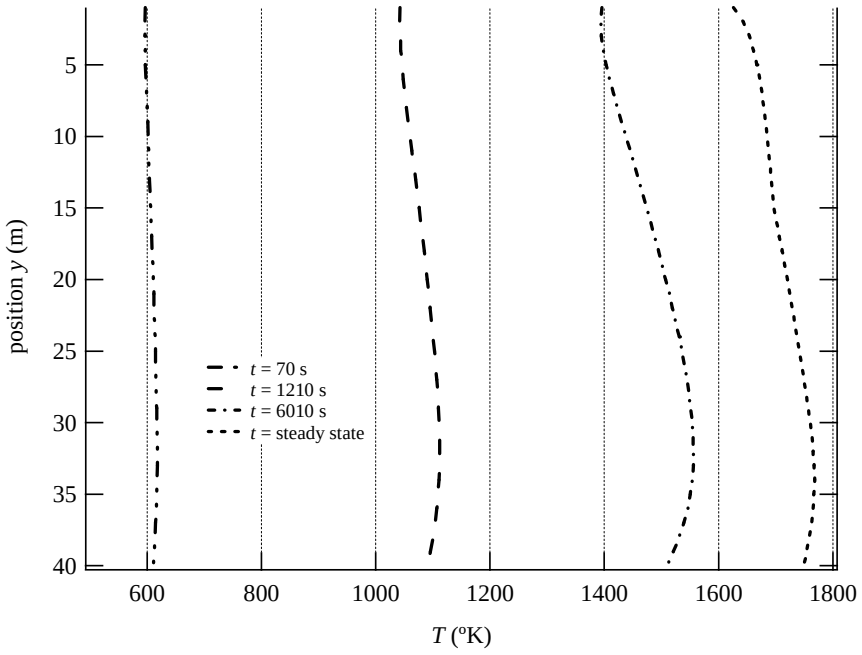

Figure 3-6. Ash Surface Temperature Profiles at *t* = 70 s, 1210 s, 6010 s, and at steady-state

As expected, the ash surface temperature increases in magnitude with time. At steady state, significant thermal resistance is evident, the maximum surface temperature increasing approximately 1220 K from the clean wall condition. Local temperatures are a maximum nearer the simulated "fireball" (located in the bottom fourth of the domain) within the boiler. This maximum temperature is slightly above the bottom of the domain (about y = 31 m) due to the imposed cooler wall temperature of the bottom boundary (y = 40 m). Also, the temperature variation along the wall becomes more pronounced with time (and deposit thickness).

Spatially resolved heat flux profiles, corresponding to the same times illustrated in Figure 3-6, are shown in Figure 3-7. The peak heat flux magnitudes decrease with time, from nominally 700 kW/m^2, and eventually reach steady-state values of around 250 kW/m^2. This behavior is in good accordance with the temperature profiles shown in

Figure 3-6. The total radiative transport changes relative to the difference between the radiation source and surface temperatures. As the deposit grows, the surface temperature increases and the net heat flux through the deposit decreases. The large decrease in the maximum heat flux (about 450 kW/m^2) illustrates the highly insulating properties of the ash. Maximum heat fluxes are also observed to occur near the bottom of the wall, closer to the fireball.

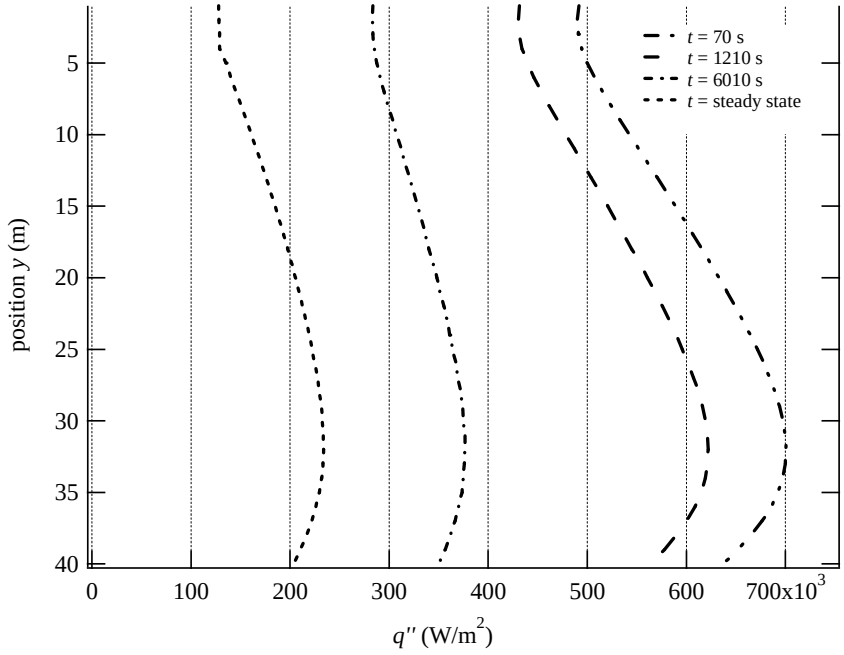

Figure 3-7. Wall Heat Flux Profiles at t = 70 s, 1210 s, 6010 s, and at Steady State

Figure 3-8 shows the deposit surface temperature and surface heat flux plotted as functions of elapsed time, at the position y = 31 m. This vertical location is approximately where q'' is a maximum along the wall throughout the deposit growth. Note the different regimes indicated. At an elapsed time of about 550 seconds, the depositing ash layer transitions to a sintered structure. The deposit continues to develop

until the effective slagging temperature (1600 K) is reached at 7100 seconds or after approximately two hours. A steady state slagging condition was reached after approximately 8.5 hours. It can be seen that the surface temperature rises very rapidly with the formation of the particulate and sintered regime layers. Most of the temperature increase and the heat flux decrease occur while the developing deposit is in the particulate and sintered regimes. This is due to the smaller effective thermal conductivity of these layers.

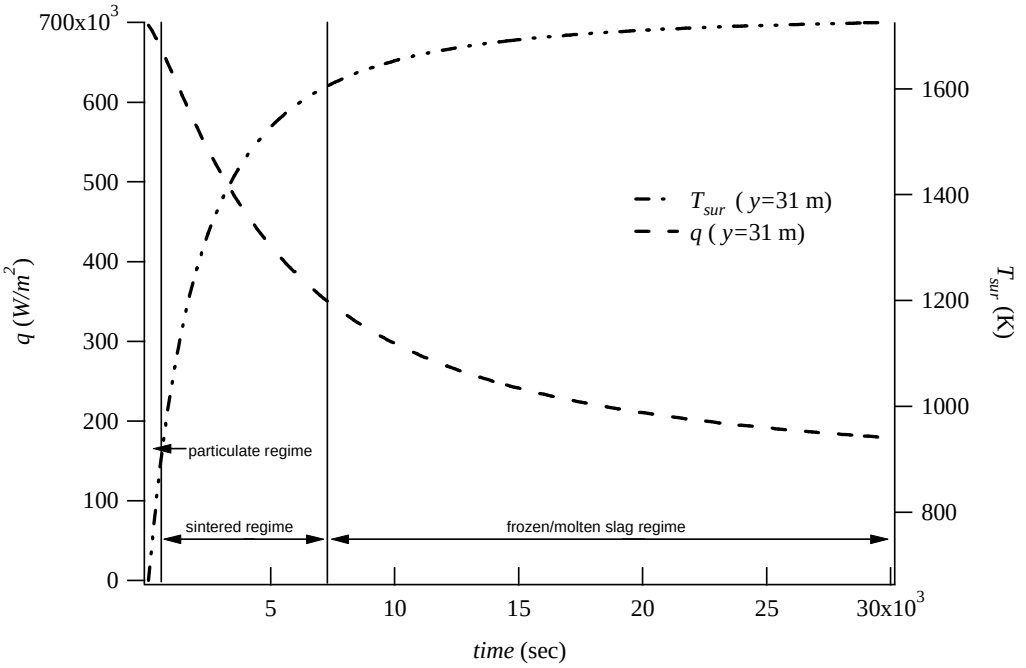

Figure 3-8. Heat Flux (left axis) and Ash Surface Temperature (right axis) as a Function of Time, at Position *y* = 31 m.

Figure 3-9 shows the total ash deposit thickness, at a time of 8400 seconds, plotted versus vertical position. Note that the horizontal axis represents vertical position, with $y = 0$ corresponding to the top of the boiler (see Figure 3-5). Specific thicknesses

(L) are shown for the particulate layer, the sintered layer, the solidified slag layer, and finally the molten slag layer.

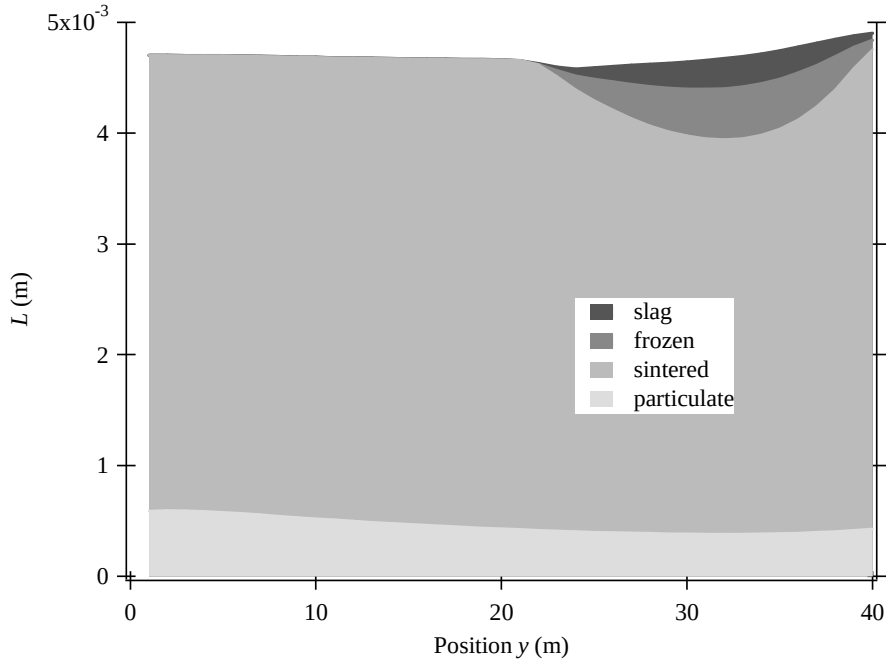

Figure 3-9. As Regime Layers and Thicknesses at 8400 s vs. Vertical Wall Position

At this time, slag is only present over the lower third of the wall. In the area where slagging exists, the deposit surface temperature has increased beyond the slagging temperature, while accumulating ash is still forming a sintered deposit farther up the wall (y < 20 m). This behavior is consistent with the variation in the fireball temperatures imposed at the centerline, as illustrated in Figure 3-5.

Figure 3-10 illustrates the thickness of a fully developed ash deposit when the entire surface has reached a steady-state slag thickness. For this scenario, the total deposit thickness ranges from 12 mm (at y = 1 m) to 20 mm (at y = 12 m) thick.

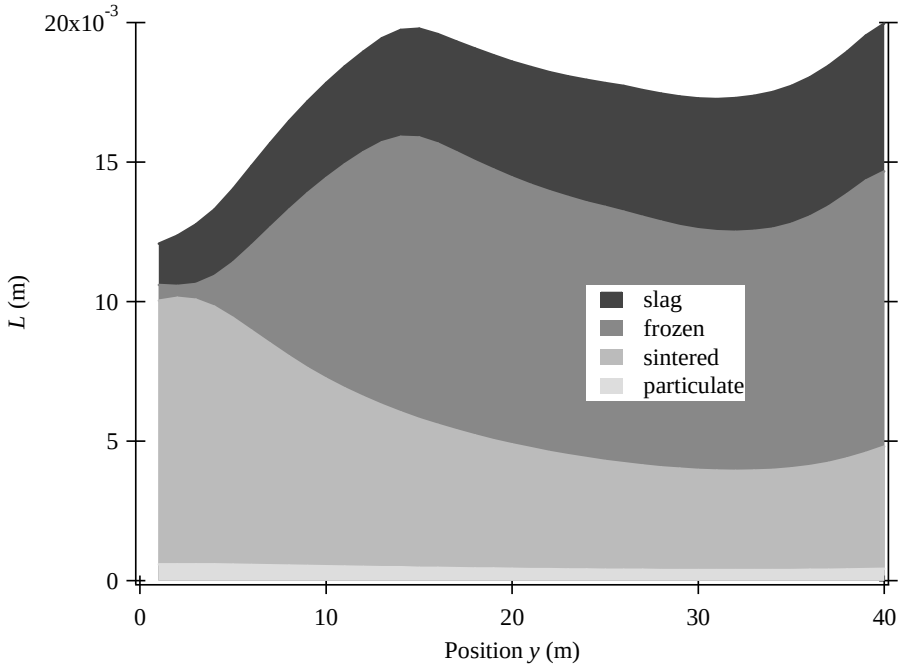

Figure 3-10. Ash Regime Layers and Thicknesses at Steady-State Conditions vs. Vertical Position

Large variations in the size of the sintered layer are evident, with the sintered layer near the bottom of the wall being nearly twice the size of the layer near the top. At steady state, the solidified slag layer (at y = 30 m) has increased significantly from its previous thickness, at 8400 seconds (shown in Figure 3-9). This increase is due to the simultaneous growth of both the slag and solidified slag layers. At steady state the solidified slag layer makes up a majority of the deposit along the wall. The slag layer grows consistently thicker with position down the wall according to the steady-state solution. (Eq. (3-8)). However the solidified slag layer grows proportionately more rapidly from the top to position y = 14 m. This behavior results from the increasing thermal resistance due to the slag layer and to spatial variations in energy transport from the fireball source.

3.6 Summary

A model describing the thermal transport through a growing ash deposit was developed and implemented in a user defined function, within FLUENT. Variations in deposit morphology and thermal properties were modeled by approximating the ash deposit using four regimes. By accepting inputs for deposit properties (based upon regime), the Thermal Transport UDF iterated in parallel with FLUENT's steady-state energy solver and computed the surface temperature and net heat flux for successive layers of ash. Boundary conditions were chosen to demonstrate the model's ability to produce transient results for a fully developed ash deposit with slag. Deposit thickness, surface temperature, and heat flux were calculated both spatially along the boiler wall and temporally. The deposit was shown to grow to a steady-state thickness of 15 mm to 20 mm. The deposit layer produced a 70% reduction in the heat flux at steady-state (from that at t = 70 s), with approximately 50% of the reduction occurring within the formation of the particulate and sintered layers. A significant increase in surface temperatures, to above 1700 K, accompanied the decrease in the net heat flux.

4 Experimental Method

To gain a better understanding of the behavior of effective thermal conductivity, ash deposits from three different coals were collected and measurements made to determine the effective thermal conductivity. By obtaining in-situ measurements, the thermal conductivity was determined for particulate ash deposits formed under both oxidizing and reducing conditions, for three coals. Table 4-1 shows a summary of the equivalence ratios for each of the coals and conditions tested.

Table 4-1. Summary of Stoichiometry Equivalence Ratios for the Experiments of Three Coals

coal	oxidizing	reducing
IL #6 Patiki	0.92	n/a
IL #6 Crown III	0.73	2.33
WY Corederro	0.71	3.10

4.1 Experimental Equipment

Experimental work was primarily conducted using equipment and resources housed in building B-41, on campus at Brigham Young University in Provo, UT. Experiments were carried out using a multi-fuel reactor (MFR). This reactor is designed as a down-fired drop tube and can accept a variety of fuels which can be fed into it at different axial locations. The reactor tube is made of silicon carbide ceramic and

measures six inches in diameter (inside) by 14 feet in length. The tube is composed of seven sections, each 24 inches in length, and each tube section is supported by two ¼-inch-thick plates also made of silicon carbide ceramic. The plates are in turn held in place by an octagonal steel frame. The octagonal steel frames of all of the sections are supported by a large central steel I-beam. Evenly placed around each section are four electrical heating elements (Micropyretics International resistance heaters). The heating elements are enclosed by 3 inches of stiff insulation, arranged in an octagonal form along the steel supporting frame. The tube section, support plates, octagonal steel frame, heating elements, and insulation enclosure make up one section (or module) of the reactor, as shown in Figure 4-1.

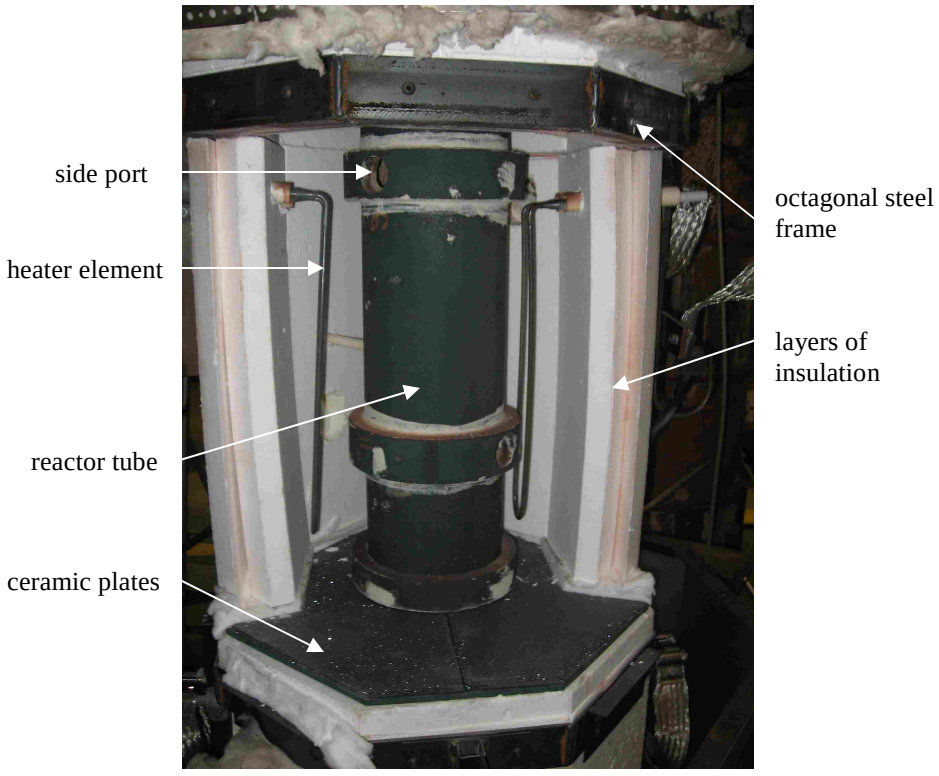

Figure 4-1. View of the Inside of a Reactor Module

Coal was injected vertically at an axial location of choice in the drop tube. The coal mixed with an additional air stream and combustion occurred inside the tube. All combustion products and gasses were exhausted by a fan at the exit of the reactor. The thermal conductivity experimental set-up, at the reactor exit, is pictured in Figure 4-2. A 12-inch gap exists between the reactor exit and the exhaust fan intake (at the level of the optical table). The reactor exit is open to the lab and this gap allows access to the reactor exhaust flow.

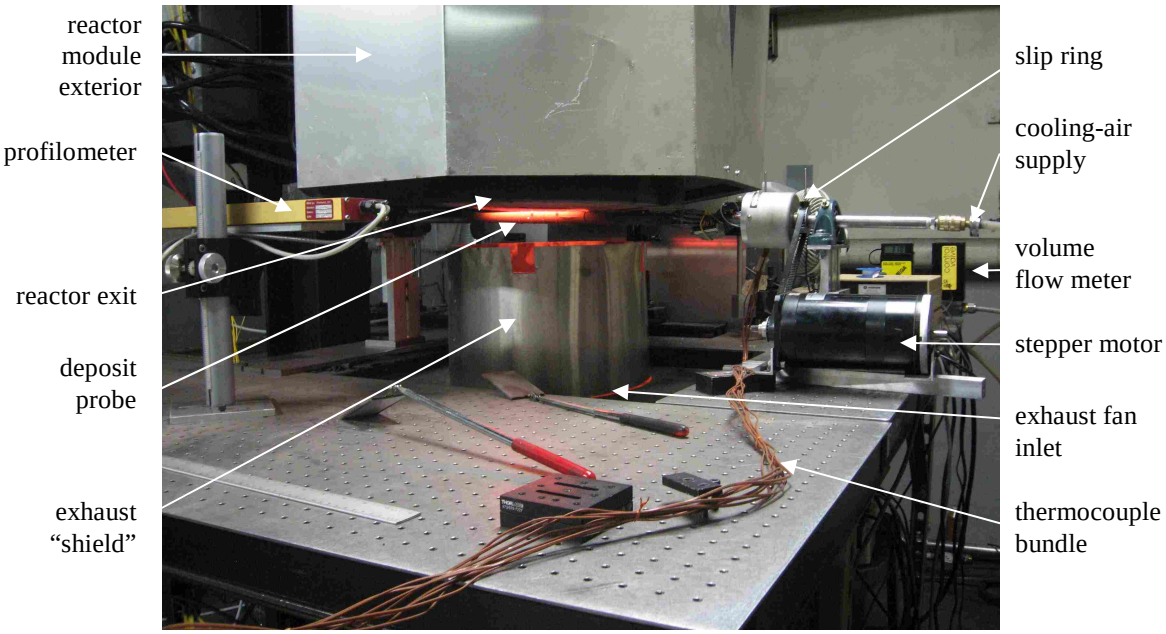

Figure 4-2. View of the Experimental Set-up at the Reactor Exit

A cylindrical "shield" of aluminum was used to appropriately direct the exhaust fan intake and ensure that reactor exhaust products were removed from the lab. There is approximately a 3-inch gap between the top of the cylindrical exhaust shield and the exit of the reactor to allow optical access to the deposition probe.

The four heating elements of each section, used to control the wall temperature of each tube section, are jointly controlled by a Chromolox control unit. Each of the reactor sections' seven control units is in an electrical control panel in the lab. Each section may be independently heated, the temperature being controlled by a percentage of signal or "power" to the heaters, or a temperature set-point entered using the section's control unit. Each heating element has two electrical leads, each connected to a large braided wire. This braided wire then junctions with 00 gage insulated compound copper wire. The junction between each braided wire and the copper wire was made by an aluminum connector (see Figure 4-3). Each reactor section is powered by a transformer, supplied by a 400 VAC source.

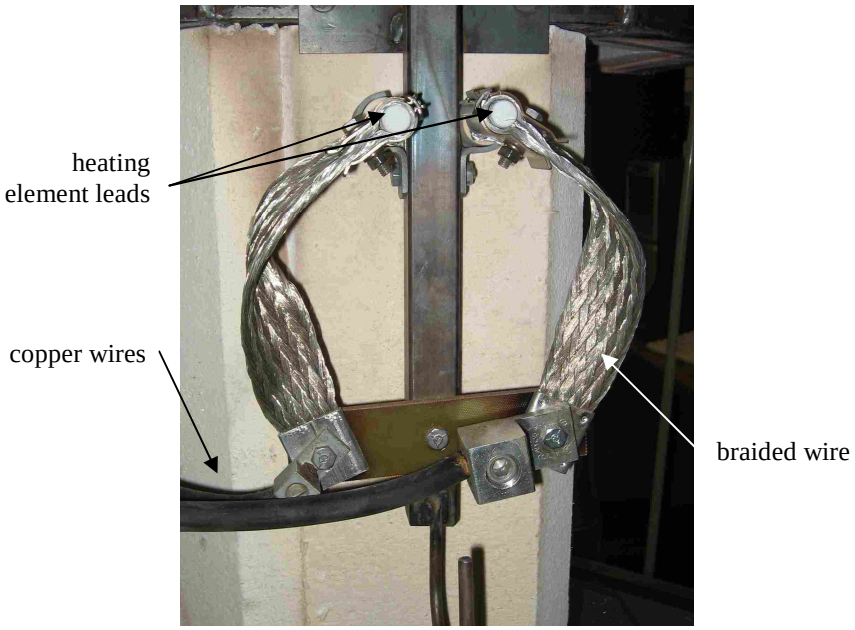

Figure 4-3. Detail of Heating Element Wiring

Additional support equipment includes a Horriba model PG-250 gas analyzer, an Omega FMA 5544 gas mass flow meter, and a Compumotor stepper motor, used to

control rotation of the ash deposition probe. Also, two desktop computers with DAQ equipment (National Instruments) and LabVIEW version 8.2.1 software were used for data acquisition.

4.2 Fuel Feed System

Pulverized coal was entrained in an air stream and then injected into the reactor. A fuel feed system was employed to control the rate at which coal was fed into the reactor. This system is an Acrison loss-in-weight controlled feeder, consisting of a hopper and a motor-driven auger, mounted on top of a scale. The hopper feeds coal by an auger, and the scale provides feedback to a mass control unit. The hopper itself was pressurized by the entrainment-air supply. Care was taken to equalize pressures seen on either side of the auger to avoid irregular back up or discharge of coal. Figure 4-4 shows the configuration of the coal feed hopper system. Coal dispensed by the auger was immediately entrained into an air stream flowing past the end of the auger feed. This entrainment set up is shown in detail in Figure 4-5. Compressed air flowed past the auger exit, entrained the dispensed pulverized coal, and continued to the fuel lance which was placed through one of the several side ports in the reactor tube wall. The fuel lance was designed to inject the air-coal mixture vertically downward. This reduced the overall turbulence and consequent impaction of coal along the reactor walls. The desired effect was to reduce the collection of ash on the walls and, therefore, increase the ash flux at the reactor exit.

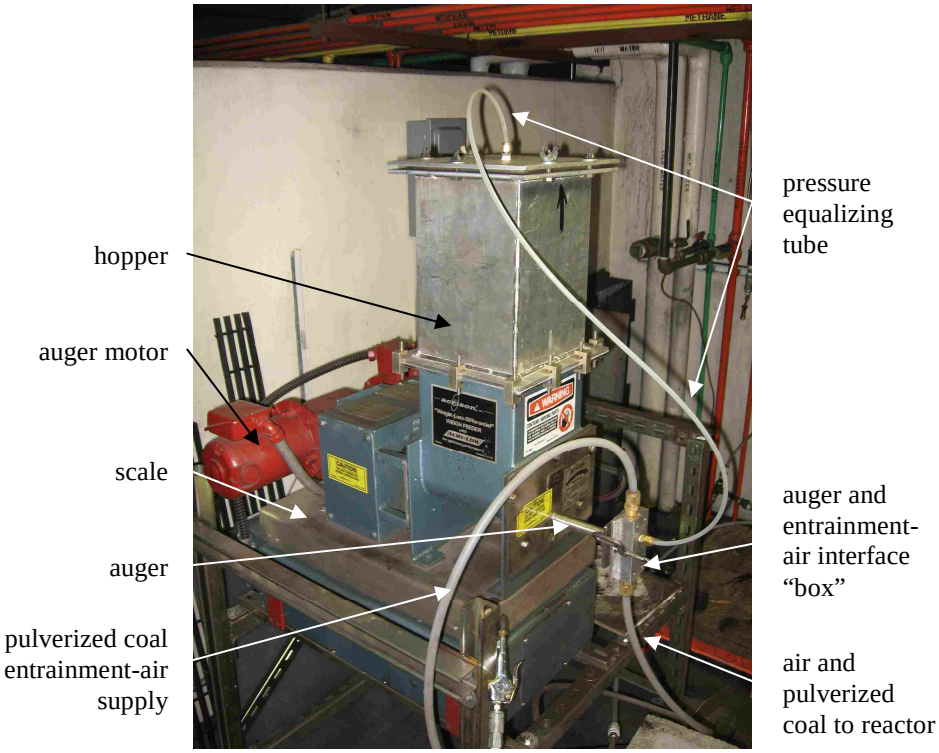

Figure 4-4. Fuel Feed System

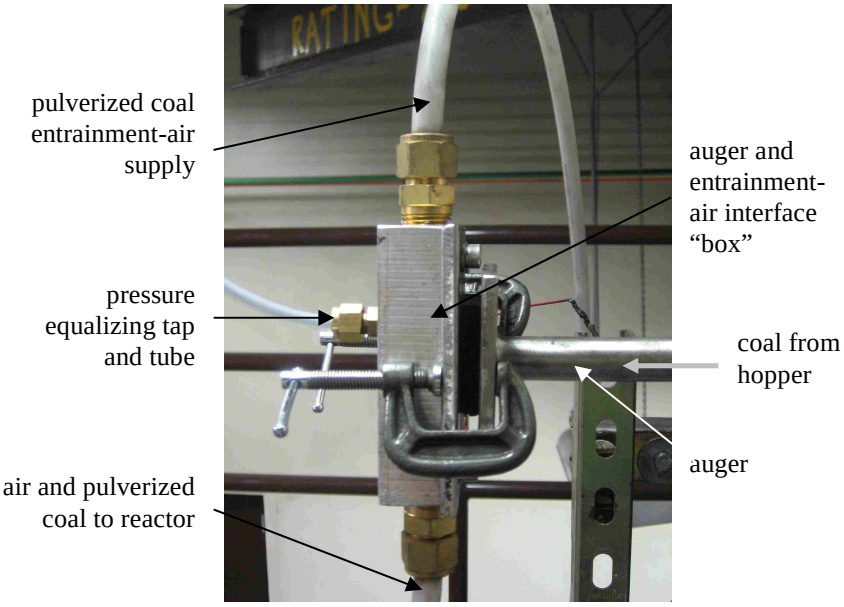

Figure 4-5. Detail of the Auger and Entrainment-Air Box for the Fuel Feed System

It is important to note that the current fuel feed system is the result of much work and experimentation as some major challenges were confronted. The basic difficulty encountered with feeding coal into the reactor was in obtaining a steady and consistent flow of fuel. It was found that some positive pressure will exist inside the reactor, and this pressure fluctuated rapidly with variations in temperatures and in fuel and air feed rates. These fluctuations were readily seen upstream of the fuel lance where coal was entrained, and they adversely affected the coal mass flow rates. It proved challenging to maintain the coal sufficiently entrained in the air stream while maintaining the entrainment-air flow as low as possible, to reduce turbulence inside the reactor and ensure the proper air-fuel ratio inside the reactor. Issues of clogging, sticking, and adequate cooling (of the lance inside the reactor) had to be addressed. In addition, due to the nature of finely pulverized coal, problems with sticking and clumping had to be solved at the interface of the auger exit and the entrainment-air supply. Adhesion of coal to surfaces at the auger and entrainment-air interface also caused adverse feedback to the mass control system of the hopper. Several "open" and "closed" (to atmospheric pressure) systems were developed and tested. Ultimately, a closed pressurized system, including pressurization of the hopper, was found to work the best, and this was the system utilized. Some adhesion of coal immediately inside the interface box still occurred and affected the mass feed rate control. However, these effects were relatively minimal. For this work, coal was pulverized to pass 100% through a # 200 mesh (nominally 75 μm) using a Mikro-Pulverizer 1SH 9600 max pulverizer.

4.3 Coal Combustion

The MFR is a laboratory-scale unit with a drop-tube design. Compressed air enters the reactor from the top and through the fuel feed lance. The fuel lance is inserted in the upper part of the reactor, usually through one of the ports in the top one or two sections of the reactor. Air and pulverized coal enter through the lance and are injected downward in the center of the reactor. The coal and air rapidly mix and burn in the upper portions of the reactor and complete "burn-out" is obtained before the particles exit through the bottom. To produce reducing conditions in the reactor further downstream, an additional lance may be inserted through a side port. Methane may be injected, creating an overall rich stoichiometry. It was found that sooting, produced by insufficient oxygen and the addition of methane, could be eliminated by premixing the methane with a small amount of air. This process allowed sufficient additional oxygen to react with the carbon, producing carbon monoxide and reducing carbon-carbon bonding. When the reactor is operating under reducing conditions, a flame "sheet" will form at the exit, where the exhaust gases and room air mix before entering the exhaust fan intake.

4.4 Instrumentation

In addition to the MFR, other equipment and instrumentation hardware were required to make in-situ measurements for determining the effective thermal conductivity. An instrumented deposition probe was constructed to collect ash deposits, and other equipment was used to control and measure temperatures, flow rates, pressures, etc.

4.4.1 Deposition Probe

A smooth drawn tube of high-carbon steel was used to collect the ash deposits. The tube has an outside diameter of 19.05 mm (0.75 in) and a wall thickness of 2.108 mm. It is 1.067 meters long and is mounted in place using two high-temperature self-aligning pillow block bearings. Each bearing attaches to an adjustable mount which can be secured to the optical bench that surrounds the exhaust inlet. Figure 4-6 is a picture of the assembled probe, mounted at the edge of the optical bench.

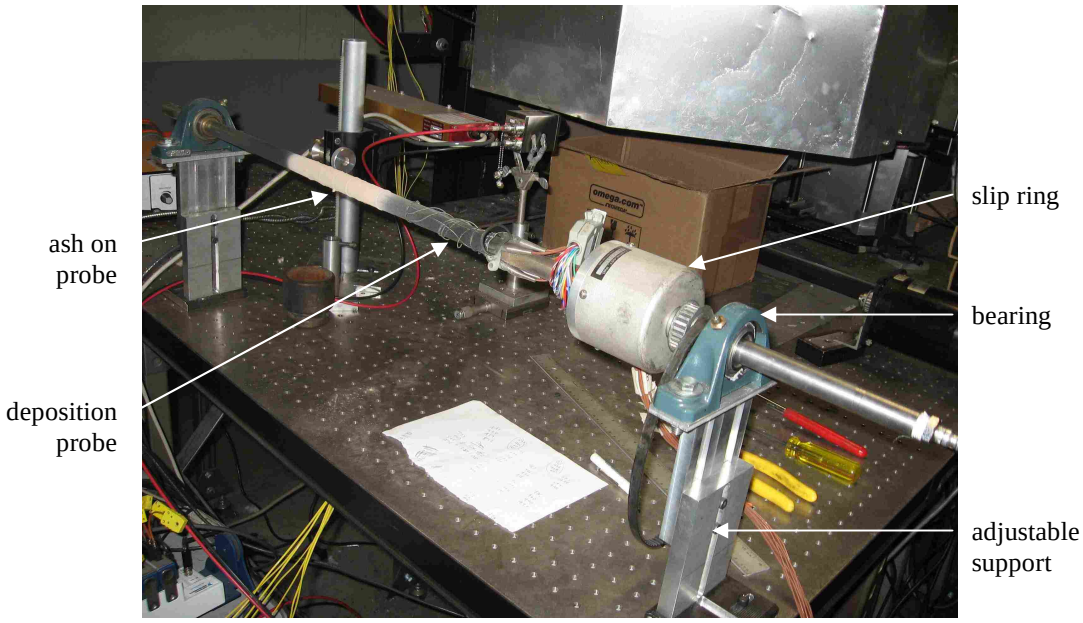

Figure 4-6. Assembled Deposition Probe, Mounted in Bearings on Adjustable Supports

4.4.2 Temperature Measurements

An array of K-type thermocouples provided numerous temperature measurements required for both the operation of the MFR and the calculation of thermal conductivity. Each section of the reactor contained one K-type thermocouple, the value of each being displayed on the main reactor control panel. These thermocouples measured the

temperature of the air gap, between the central ceramic tube and the surrounding layers of insulation, of each section (see Figure 4-1). Additionally, each section was instrumented with one thermocouple placed at the outer edge of the supporting silicon carbide plates. The temperature of the plate edges was monitored and recorded in order to track the temperature gradient across the plates. (The inner edge temperature was assumed to be approximately that of the air gap, as measured by the thermocouple in the air gap of each section.) These temperature measurements were necessary in order to safely operate the reactor. The temperature gradient across the supporting plates had to be controlled to ensure it did not exceed 200˚ C, thus avoiding any damage due to excessive thermal stresses.

The deposit probe was instrumented with eight thermocouples, four on the inside and four on the outside. All of the thermocouples were placed in a 0.0762-meter-long "test section," located in the middle of the probe. Figure 4-7 shows a picture of the test section in more detail.

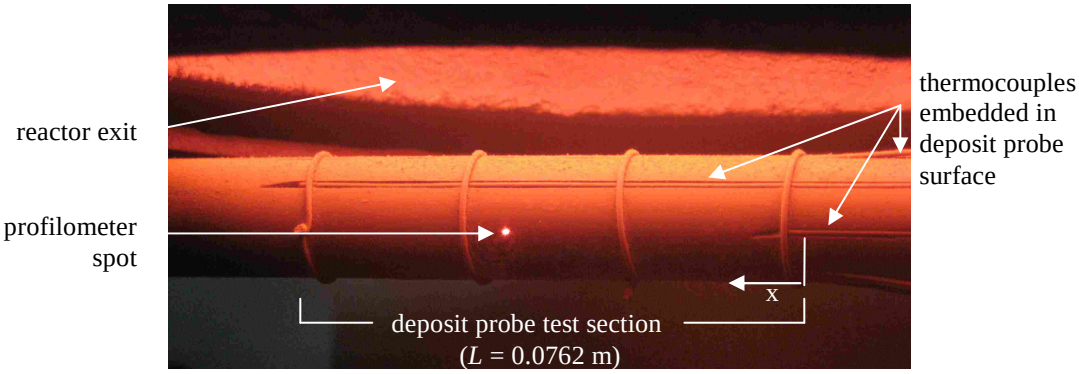

Figure 4-7. Test Section of Instrumented Deposition Probe

The four outside thermocouples were evenly spaced axially along the outside surface of the deposit probe at positions $x = 0$, $x = L/3$, $x = L \cdot 2/3$, and $x = L$. They were embedded in grooves machined into the probe's surface. Four thin (0.8-mm diameter) bands of wire secured the thermocouples, one placed near each thermocouple bead. These wire bands did not affect the temperature measurements of the thermocouples. In addition, the thermocouples were placed tangentially at 90 degree intervals around the probe. This can be seen clearly in Figure 4-8, which illustrates the positions of the thermocouples as they would appear by looking down the axis of the test section, from the upstream end of the deposit probe.

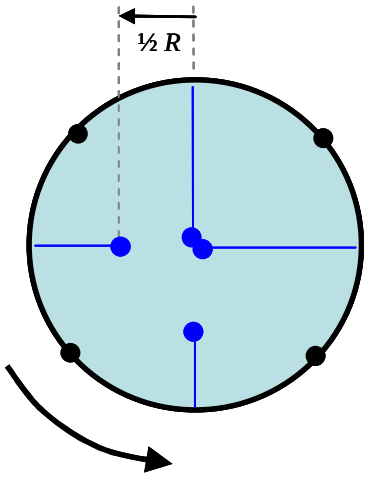

Figure 4-8. Schematic of Thermocouple Positions in the Deposit Probe Test Section: View Looking Down the Axis from the Upstream End of the Probe

This arrangement of the four outside probe thermocouples provided axial and radial temperature distribution data along the probe. The radial positions of the four internal thermocouples are also detailed in Figure 4-8. The two thermocouples placed at ½ of the inner radius ($r = R/2$) were located axially at the upstream and downstream ends of the probe test section (one at $x = 0$ and one at $x = L$). Likewise, the two thermocouples

positioned at the axis of the probe (r = 0) were placed at the upstream and downstream ends of the probe test section, to sample the centerline temperature of the cooling-air. The inner thermocouples provided data on the cooling-air temperatures. The inside cooling-air temperatures were used to determine the total heat transfer through the probe and ash deposit in the test section.

4.4.3 Additional Equipment

Surface temperature measurements of the ash deposit were obtained by analyzing spectral data taken using a Fourier Transform Infrared (FTIR) spectrometer. Also, several pressure transducers were employed, in conjunction with thermocouples and appropriate orifices, to obtain the flow rates of natural gas and air. These transducers were monitored by multiple data acquisition systems.

The rotation of the deposit probe was controlled using a stepper motor connected to a desktop computer. The motor was controlled by the computer using commands entered through a hyper-terminal connection.

A profilometer (Schmitt Measurement Systems, model Acuity AR600) was employed to measure the ash thickness on the deposit probe surface. The profilometer measures distance by emitting a laser beam and measuring the angle of reflection via a detection array. By determining the changes in the angle of reflection, the distance to a surface may be measured. The profilometer was also controlled by commands entered via a hyper-terminal connection. Data was fed back to the hyper-terminal and recorded as a simple text output file.

The flow of cooling-air through the deposition probe was regulated by an automatic mass flow controller. Equipped with a solenoid valve, the Omega FMA5544

mass flow controller has a local set point potentiometer which may be adjusted to provide the desired mass flow.

4.5 Experimental Set Up

Located in the B41 Lab, an experimental set up was designed to collect ash deposits and make all the necessary measurements to obtain the effective thermal conductivity in-situ. Pulverized coal was burned in the reactor and the stoichiometry was monitored and controlled by adjusting air, methane, and coal mass flow rates. The use of an auxiliary methane lance created a local fuel-rich region around the deposit probe when reducing conditions were desired. The deposit probe rotated (¼ rpm) about its axis beneath the exit of the reactor and above the exhaust fan inlet. Metered cooling-air entered one end of the probe and exited the other end. The FTIR spectrometer, thermocouples, and profilometer provided measurements of probe temperatures, ash deposit temperatures, cooling-air temperatures, and deposit thickness.

The deposit probe test section was positioned to be approximately in the center of the reactor exit opening and about 1.5 cm beneath the bottom of the octagonal support steel frame. Because the FTIR required precise alignment, its target spot on the deposit probe was located using two intersecting visible lasers. The deposit probe was finely positioned, using the lasers to locate the desired target point. On the opposite side of the probe from the FTIR, the profilometer was used to make measurements.

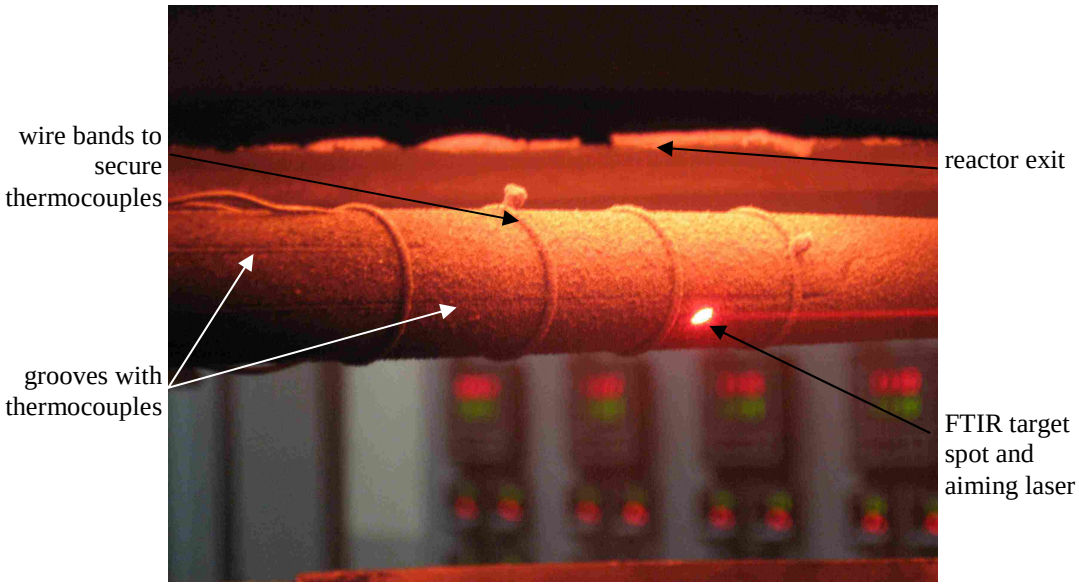

Figure 4-9. FTIR Aiming Laser and Target Spot on the Deposit Probe with a Thin Ash Deposit

The profilometer was mounted on an adjustable but rigid stand, about 13 inches from the probe. It was positioned with the measuring laser perpendicular to the probe axis, and measurements were taken at the vertical mid-point of the probe (equator) and at the same axial position as that of the target spot of the FTIR spectrometer. The visible laser spot in Figure 4-7 depicts the position that the profilometer typically saw on the deposit probe.

4.6 Experimental Procedure

Each experiment required about 14 to 18 hours to complete. Consequently, all of the experiments were performed on separate days. An experiment began by carefully warming up the MFR; then, coal was burned and the necessary measurements were taken. Afterward, the reactor had to be cooled down.

4.6.1 MFR Warm up and Preparation

The MFR was first heated electrically before burning coal and collecting ash. The reactor wall (tube wall) of each section was heated to approximately 1100˚ C. It was found that maintaining the walls at this temperature facilitated good combustion and burnout of the coal. However, the first, or top, section of the reactor lost heat to the surroundings considerably faster than the other sections. This loss caused it to warm up slower; therefore, it was typically heated to only 1050˚ C before burning coal. Once coal was burning, energy released from the coal continued to heat the first section, which was maintained at the same temperature as the other sections. Due to the sensitivity of the silicon carbide material to thermal shock, special care was exercised to control the thermal gradients created by electrical heating. The rate of temperature change (heating and cooling) of the tube walls was limited to a maximum of 300˚ C per hour and was monitored by noting the section wall temperatures displayed by each section controller on the control panel. Additionally, the temperature change across the support plates was monitored by thermocouples plugged into a DAQ system. The difference was not allowed to exceed 200˚ C. Particular diligence was needed when initially heating the tube walls so that they did not heat up too fast. Care was also required when heating the walls to the upper extreme temperatures (around 1000˚ C to 1100˚ C) to insure that the temperature gradient across the plates did not become too large. Proper heating of the entire reactor required about five hours.

While the reactor heated up, several other tasks were completed in preparing to burn coal. The exhaust filter was changed (typically once per run), the coal hopper was refilled, the probe cleaned off and positioned beneath the reactor exit, and the various

instruments turned on and positioned. The fuel lance was usually left installed in one of the reactor ports. Air to the fuel lance was generally left on the entire time to keep it cool, helping to extend its life. Before the MFR reached operating temperature, the air supplies to both the fuel lance and to the top of the reactor (necessary for burning the coal) were turned on and set at their approximate operating flow rates for when coal was burning.

4.6.2 Coal Combustion and Deposit Collection

To begin burning coal, the coal feed system was turned on using the solid fuel hopper controls. The feed rate was set, and the instantaneous readout of the coal mass feed rate monitored. It was the nature of the coal feeder to grossly over-shoot the target feed rate when initially starting. This problem typically only occurred for several seconds; then, the actual feed rate adjusted, at first rapidly and then more slowly, to the target feed rate. About five minutes was usually required to reach a steady feed rate. Changes were made to the feed set-point while the system was running. The gas analyzer was used to monitor the combustion products and help ensure that the desired conditions were met. For all of the experiments, complete burnout of the pulverized coal was desired. Experiments conducted previously on the burnout of coals in the MFR were performed by a fellow student in collaboration with this work. This investigation examined fly ash collected at various axial locations within the MFR and provided information about the appropriate ranges of temperature and about mass flow rates for air and fuel required to achieve burnout [21]. For the current study, burnout of the coal was ensured by monitoring the oxygen and carbon monoxide levels measured at the reactor exit by the gas analyzer. For experiments performed under reducing conditions, the coal

was fired in the same way as under oxidizing conditions, using the gas analyzer to monitor the stoichiometry. Then, by adding methane, reducing conditions were obtained around the ash deposit at the exit of the reactor.

Collecting ash on the deposit probe was straight forward when proper conditions were created and maintained. Much time and effort was spent in determining which conditions produced a more uniform and thicker deposit in less time. Several variables were directly modified to produce better quality deposits and provide better data: the probe diameter and material, probe positioning, shield geometry and positioning, exhaust and reactant flow rates, and the way the coal was injected and burned inside the reactor. The deposit probe was constructed of high-carbon steel, which resisted corrosion and was more easily machined than stainless steel. It was determined that smaller diameter probes result in greater capture efficiencies (deposition rate) [21]. A 19.05-mm (¾-inch) outer diameter tube was chosen as the smallest size which still provided enough space for placing all of the thermocouples. The deposit probe was placed as close to the reactor exit as possible. This minimized the effects of the atmospheric air entrained by the exhaust fan on the probe and it minimized the temperature difference observed across the diameter of the probe, from top to bottom. The exhaust fan "shield" was made of a sheet metal cylinder centered around the exhaust fan inlet and placed about eight centimeters below the exit of the reactor (see Figure 4-2). Also, to minimize the effects of entrained atmospheric air, the speed of the exhaust fan was maintained as low as possible. The fuel lance was constructed of ¼-inch inside diameter stainless steel tubing. A stainless steel diffuser was attached to the end, to direct the air and pulverized coal downward and reduced the turbulence.

Deposition rates on the probe were typically from 0.07 mm to 0.2 mm per hour. Consequently, a deposit of sufficient thickness to make good measurements of thermal conductivity (typically on the order of 1.0 mm) required five to ten hours of burn time. Because the hopper will hold only about eight kilograms of coal, periodic interruptions to the flow of coal had to be made in order to refill the hopper. Throughout each experiment all aspects and conditions of the reactor were carefully monitored while collecting an ash deposit.

4.6.3 Experimental Measurements

To make the measurements necessary for determining the effective thermal conductivity, coal was burned in the drop-tube reactor and ash collected on the deposit probe. With the reactor at operating temperature, the cleaned deposit probe was mounted beneath the reactor exit and positioned using the two visible lasers. This was done to determine where the FTIR spectrometer would be viewing the probe. The second surface thermocouple (from up stream, at axial location $x = L/3$), on the probe was positioned at the same location as the FTIR spectrometer target spot. Cooling-air was turned on to the probe and then, using the FITR spectrometer, several calibration measurements were taken of the clean deposit probe at various temperatures. The coal feed was then turned on and allowed to stabilize for about 5 minutes, and additional measurements with the FTIR spectrometer were taken. This process provided the calibration data needed for making surface temperature measurements using data collected by the FTIR spectrometer.

Next, the air and coal flow rates were adjusted to achieve the desired stoichiometry and the stepper motor started. The deposit probe temperatures were

recorded from this point onward. Also the profilometer was turned on. The exact start times of the motor, deposit probe temperature record, and profilometer record were noted so that all three could be synchronized later according to time. Coal was burned and temperature and profilometer data were recorded continuously at sample rates of ¼ Hz and ½ Hz respectively. The stepper motor was set to rotate the probe continuously at ¼ rpm.

The surface temperature of the ash deposit was obtained from low-resolution scans made with the FTIR spectrometer. These scans have a resolution of 32 wave numbers and required about five seconds to complete. Details of the scans and how the surface temperature was determined using the FTIR spectrometer are provided in "Ash Deposit Surface Temperature" in the following section (4.7.1). The scans were taken at selected times, usually about every 45 minutes. More accurate measurements from the FTIR spectrometer were made by turning off the coal feed and stopping the rotation of the probe, thus preventing interference from hot ash and exhaust gasses with the spectral measurements. Care was taken to stop the probe in exactly the same position (with respect to θ) it had been in when calibrating the FTIR spectrometer. This method resulted in better spectral measurements by decreasing the noise and improving the calibration accuracy. For measurements made under reducing conditions, the coal was necessarily left on and scans by the FTIR spectrometer were made through a nitrogen-purged "snorkel." Figure 4-10 illustrates the experimental set up with the snorkel in use. Exhaust gasses and ash were removed from the optical path of the FTIR spectrometer by using this snorkel. It was placed a few millimeters from the deposit probe surface and extended (perpendicular to the probe) beyond the reactor exit into the atmospheric air.

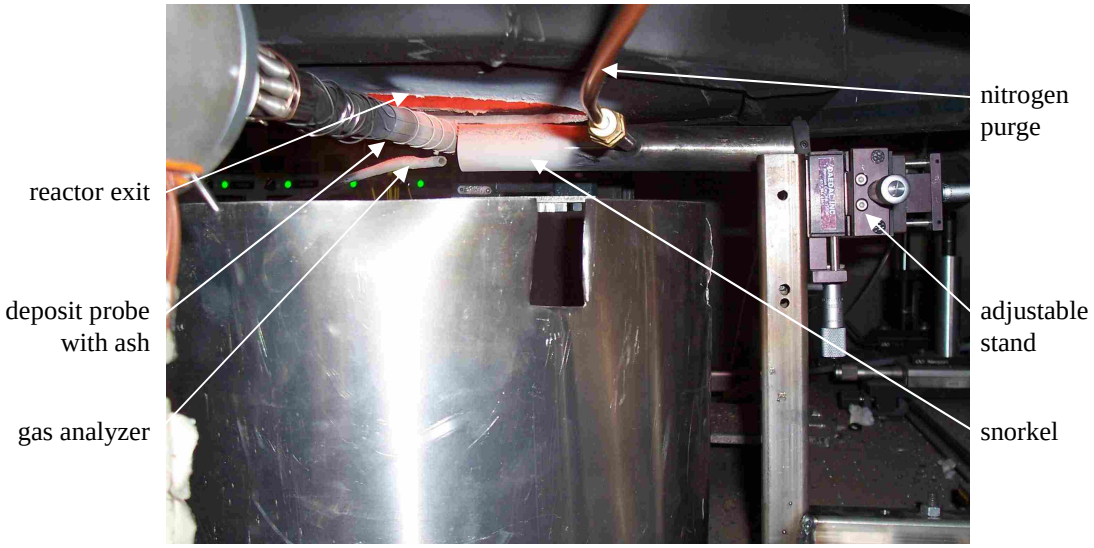

Figure 4-10. Experimental Set-up with the Snorkel, Reducing Conditions

The time, the temperature of each reactor section, and the measurements of the cooling-air meter were recorded each time an FTIR spectrometer scan was made. In this way the surface temperatures later obtained could be correlated to the appropriate probe temperatures and deposit thicknesses. While running an experiment, the mass flow rates, temperatures, coal feed rate, and exhaust fan were monitored to ensure the desired conditions were maintained and the equipment was functioning properly.

Upon completion of an experiment, the coal was turned off. The data acquisition system (for the probe temperatures) and profilometer were stopped, again taking note of the time for reference. However, the stepper motor was left on so that the probe continued to rotate until relatively cool (less than 100˚ C). The heating element controllers were then turned down to begin cooling the reactor. Air flowing into the reactor and through the probe and fuel lance was left on to help the reactor cool faster and to keep the probe and lance temperatures down. When the MFR was sufficiently cooled,

all of the air flows and the exhaust were turned off. Any equipment remaining on was also turned off.

4.7 Data Analysis

A successful experimental run resulted in data obtained for these primary measurements: surface temperature of the ash deposit on the probe at a single spot (one temperature), temperatures of the cooling-air upstream and downstream of the deposit probe test section (four temperatures, two at $r = 0$ and two at $r = R/2$), the thickness of the ash deposit, surface temperatures of the probe (four temperatures, separated axially by $L/3$ and tangentially by 90˚), and the volume flow rate of the cooling-air.

This section discusses how this raw data was processed in order to obtain an effective thermal conductivity. Data from the FTIR spectrometer, the profilometer, and the deposit probe, were analyzed to obtain values for the heat flux, deposit thickness, and temperature difference across the ash deposit. Two methods for determining the effective thermal conductivity from the in-situ data are presented.

4.7.1 Ash Deposit Surface Temperature

The surface temperature of the ash deposit was calculated from measurements taken by the FTIR spectrometer. The surface temperature was determined by another student working in collaboration on this project. This section summarizes how the surface temperature measurements were obtained.

Spectral measurements of the ash deposit surface were made by the FTIR spectrometer at selected sample times, usually about every 45 minutes during an experiment. These spectra were recorded using dedicated software. In order to make

accurate measurements with the FTIR spectrometer, a specific response function had to be determined for each experimental run. The emittance of the probe surface, coated with a high-temperature black paint, was previously determined by measurements using the FTIR spectrometer and also a black body source. Before each run, a section of the probe was cleaned and painted. The FTIR spectrometer was aimed to sample a point very close to (but not directly on top of) one of the surface thermocouples in the deposit probe. Several spectra were then taken of the probe at different known temperatures (from the thermocouple measurement), and these measurements were used to create the response function. The data obtained directly from the FTIR spectrometer was a spectral signal. The signal had to be processed using the response function to obtain a spectral emissive power. The emissive power at several wave numbers (more than 10) along a "gray" band of the spectra were examined. These emissive powers were ratioed to a reference value. The emissive power at corresponding wave numbers on a black body curve (from Planck's Function, based on a guessed surface temperature) was also ratioed to a corresponding reference value. A least-squares method was used to minimize (by varying the temperature) the difference between the sum of the ratios of the measured emissive powers and the Planck's Function emissive powers. The temperature resulting in the least error was the surface temperature of the ash deposit. By this procedure the surface temperature was determined from measurements made by the FTIR spectrometer.

Importantly, several preliminary experiments were conducted on how to accurately obtain the probe surface temperature from spectral measurements. It was determined that spectra obtained with ash and exhaust gasses present in the optical path could not be adequately filtered. Additionally, the exhaust products were found to add

significant emission within many of the spectral bands measured by the FTIR spectrometer, and these emission bands had to be effectively removed in order to obtain an accurate temperature. Although the probe was rotated relatively slowly, measuring the probe while it rotated resulted in more noisy and erroneous spectra. It is believed that some of this error resulted from the slight eccentricity of the probe which caused the probe's surface to move in and out of "focus" with the FTIR spectrometer. Finally, much better accuracy and consistency was obtained by carefully stopping the probe at the same tangential point (with respect to θ) each time to make measurements.

4.7.2 Cooling-air Mass Flow Rate

Measurements from the volumetric flow meter were periodically recorded by hand throughout each experimental run: the flow meter value and the time were usually noted at least every 40 to 60 minutes. The volume flow rate was typically set to 320 standard liters per minute. Little fluctuation (< 1.5 %) in the metered value was observed over the course of each experimental run.

The volumetric flow meter measures the flow of air in units of Standard Liters per minute (SLM). The recorded flow rates were input into data processing software and then converted to mass flow rates. The flow meter was calibrated for nitrogen at "standard" temperature and pressure of 21.1˚C and 101.325 kPa, respectively. The cooling-air temperature was found to be nominally 22˚C; however, the atmospheric pressure was an average of 85.5 kPa, and this change had to be accounted for. A coefficient, *C*, for pressure correction was multiplied by the meter value and was obtained by a simple ratio of the calibration pressure to the actual pressure:

$$C = \frac{P_{cal}}{P_{act}} = \frac{101.325}{85.5} = 1.185 \quad \textbf{(4-1)}$$

A corrected volumetric flow measurement (Actual Liters per minute, ALM) was obtained by Eq. (4-2).

$$ALM = C(SLM) \quad \textbf{(4-2)}$$

Multiplying the *ALM* by the density of air (at 21˚C and 85.5 kPa) and dividing by 1,000 (liters per cubic meter) and also by 60 (seconds per minute) yielded a mass flow rate in (kg/s), given by Eq. (4-3):

$$\dot{m} = \rho\left(\frac{ALM}{1000}\right)\left(\frac{1}{60}\right) \quad \textbf{(4-3)}$$

4.7.3 Ash Deposit Thickness

Measurements made by the profilometer were recorded to a text file. Controls for the profilometer were set to take a measurement every two seconds (½ Hz) continuously throughout each experiment. With the deposit probe rotating at a constant ¼ rpm, this sample rate resulted in 120 measurements per rotation, or one for every 3 degrees of rotation. Upon completion of an experimental run, the recorded data file from the profilometer was imported into data processing software. The noted start and stop times of the recording of the profilometer were then used to correlate each data point to a time.

The data was then graphed and analyzed as a function of time. Figure 4-11 shows the data recorded using the profilometer over a period of 15 minutes and is representative of the plots obtained for each experimental run.

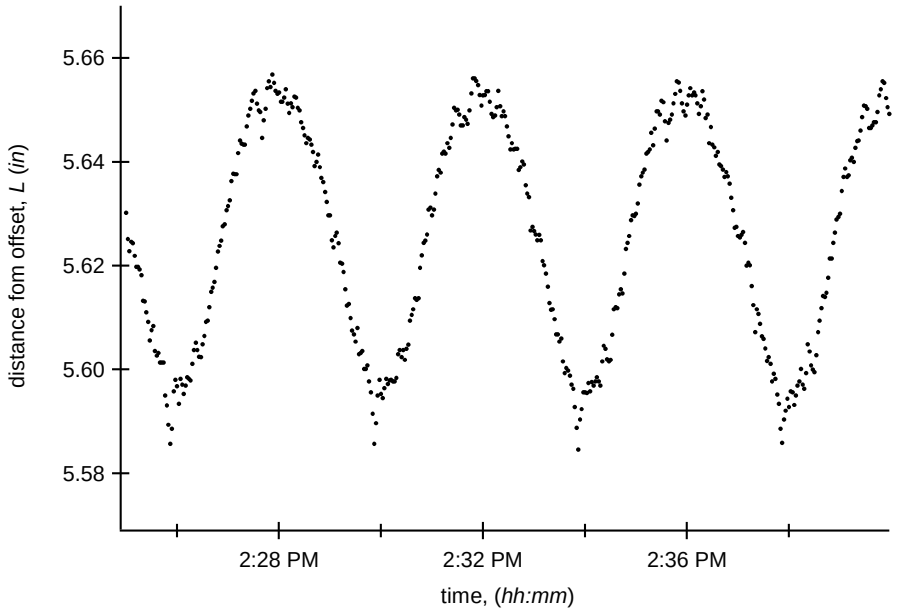

Figure 4-11. Profilometer Raw Data Plot for IL #6 Patiki Coal (Distance to the Probe Surface, *L*, is Shown vs. Time)

The data shown are the measured distance, in inches, from a zero-point to the surface of the probe. Note the cyclic behavior of the data is due to the deposit probe tube being slightly eccentric about its axis as it rotates. Inherent imperfections in the tube and the effects of thermal expansion, combined with the probe's rotation, were believed to contribute to the observed eccentricity. At selected times, when surface temperature was obtained using the FTIR spectrometer, the data from the profilometer was analyzed to determine the deposit thickness. The profilometer data was averaged over two full revolutions (240 data points or eight minutes) immediately prior to each surface

temperature sample time. This averaging accommodates the cyclic behavior of the rotating probe and any non-uniformity of the ash deposit surface. For each experiment, a "baseline" measurement was also determined, representing the average distance from the profilometer to the probe with no ash on it. This measurement was accomplished by averaging two full revolutions of the probe before, or immediately after, the coal was burned in the reactor. For the desired times, the average value of the profilometer data was then subtracted from the established baseline value to yield the thickness of the ash deposit.

4.7.4 Probe Surface Temperatures

Temperatures from the four surface thermocouples of the deposit probe were recorded continuously throughout every experiment. LabVIEW was used to record each of the temperatures once every four seconds (¼ Hz), or one measurement every 6 degrees of rotation. The temperatures were written to a text file. Deposit probe surface temperatures, recorded using LabVIEW for each experimental run, were imported into data processing software and correlated with time. Calculation of the effective thermal conductivity of the ash deposit required measurements of the probe surface temperature at the location of the FTIR spectrometer target spot.

For experiments with the IL #6 Crown III and WY Corederro coals, this temperature was obtained by stopping the rotation of the probe at the time of measurement, with one of the probe thermocouples aligned to the target spot (the same position used in calibration of the FTIR spectrometer). This alignment allowed the probe surface temperature at the desired location to be measured directly by the thermocouple. For experiments of the IL #6 Patiki coal, the rotating probe was not stopped to perform

measurements; therefore, the probe surface temperature at the FTIR spectrometer target spot had to be calculated The probe surface temperature was found as a function of θ and x, and then evaluated at the corresponding location of the FTIR spectrometer target spot. This was accomplished using the data from several minutes immediately before the desired sample time had to be analyzed. Figure 4-12 shows an interrogation period of 15 minutes. The four surface temperatures are identified by their positions along the deposit probe test section axis (x/L), where x is measured from the upstream start of the test section.

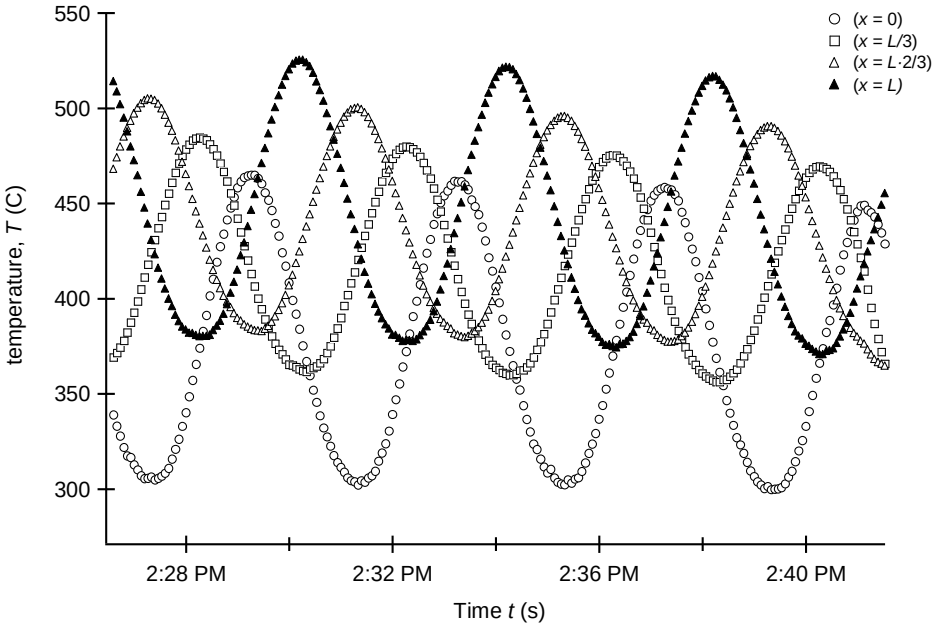

Figure 4-12. Representative Variation in Probe Surface Temperature vs. Time for IL #6 Crown III Coal.

The data, for eight minutes (two revolutions) previous to the time (14:46) a measurement of the deposit surface was taken using the FTIR spectrometer, was analyzed to obtain the necessary information to determine the distribution of the probe surface

temperature. Because of the location of the thermocouples on the deposit probe, the four surface temperatures have different phases. In order to compare these temperatures to each other and to the temperatures of the cooling-air, all of the recorded temperatures were then correlated by tangential position, θ. This was done by shifting the data sets (in time, with the thermocouple at $x = 0$ as a reference) so that the tangential positions of the four thermocouples on the deposit probe matched in space. Figure 4-13 shows the equivalent 15-minute interrogation window of the temperatures correlated by tangential position, θ.

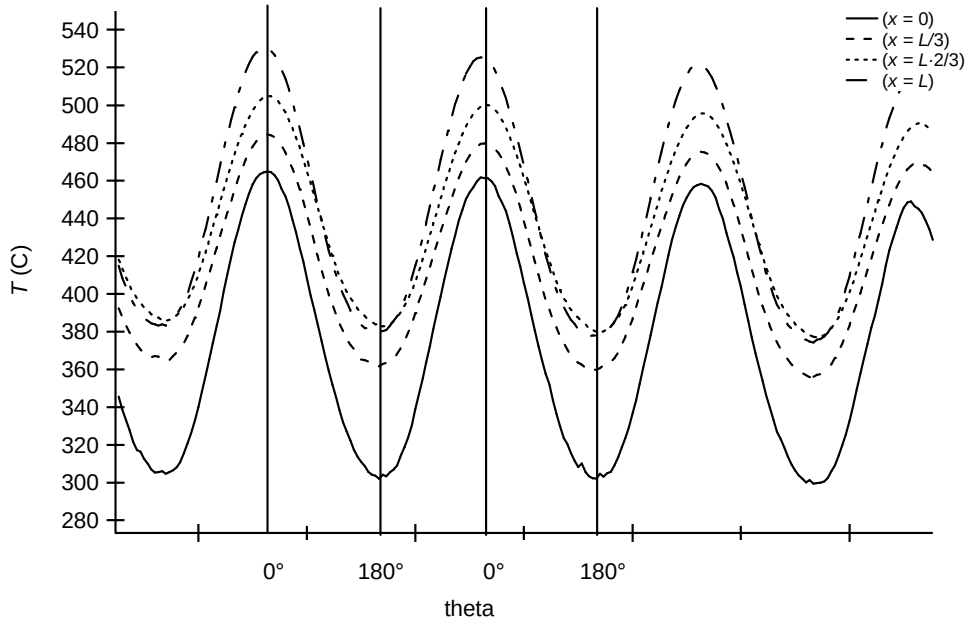

Figure 4-13. Representative Probe Surface Temperatures vs. Tangential Position, θ, for IL #6 Crown III Coal.

Consequently, the temperatures no longer corresponded with each other in time; however, the shift in space was made to minimize the discrepancy of the temperatures in time. The temporal offsets for the four thermocouples positioned at $x = 0$, $x = L/3$, $x =$

$L(2/3)$ and $x = L$ were ±0 s, -60 s, -120 s, and -180 s respectively. The average temperature (T_{avg}) of each probe surface thermocouple, at a time of interest, was then characterized by analyzing the data during a period of eight minutes (two revolutions) prior to the desired sample time. Figure 4-13 also shows that the probe temperatures vary in the axial direction, across the deposit probe test section. Approximation of this axial variation as a function of x, was obtained using a central difference between the thermocouple measurements made at corresponding tangential positions. The probe surface temperatures and the deposit surface temperature were determined for several times in each experimental run.

Figure 4-14 shows the probe surface temperature, T_p, and the ash deposit surface temperature, T_s, plotted vs. deposit thickness. T_p is the probe temperature at the same location as the target spot of the FTIR spectrometer. The temperatures are plotted for the three coals under oxidizing conditions. Because measurements were made of the deposit as it grew, data points represent the probe surface temperature and the ash deposit surface temperature when the deposit had grown to the thickness indicated (x-axis). Note that individual experimental runs are noted in each plot by the date they were performed (i.e. "10-13"). The temperature difference across the ash deposit can be seen to increase very rapidly with the formation of the first 0.2 mm of deposit. The WY Corederro coal shows the greatest temperature spread, at nearly 300˚ C for a deposit 0.055 mm thick.

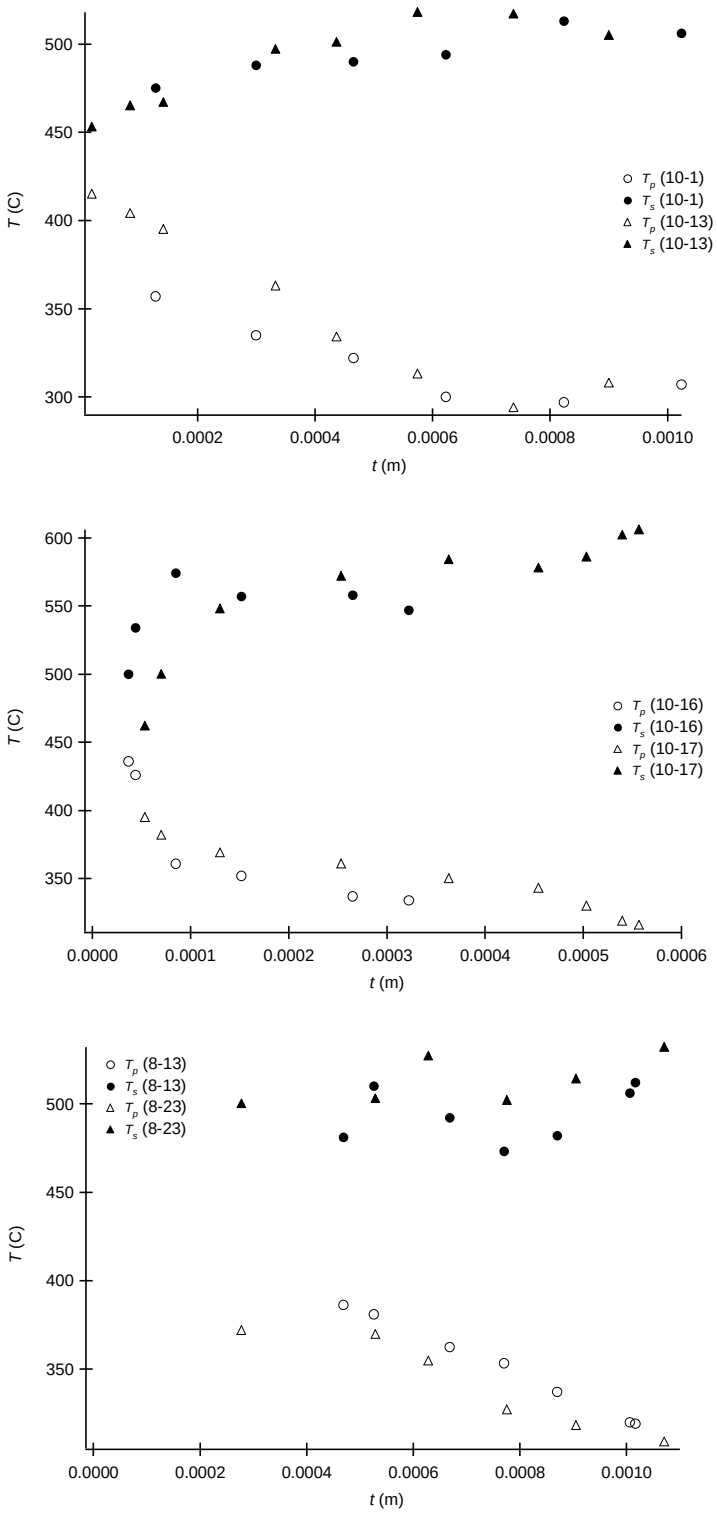

Figure 4-14. Temperatures of the Ash Deposit Surface and the Probe Surface vs. Deposit Thickness:
top panel - IL #6 Crown III Coal, Oxidizing Conditions
middle panel - WY Corederro Coal, Oxidizing Conditions
bottom panel - IL #6 Patiki Coal, Oxidizing Conditions

Figure 4-15 shows temperature plots of ash deposits of IL #6 Crown III and the WY Corederro coals formed under reducing conditions.

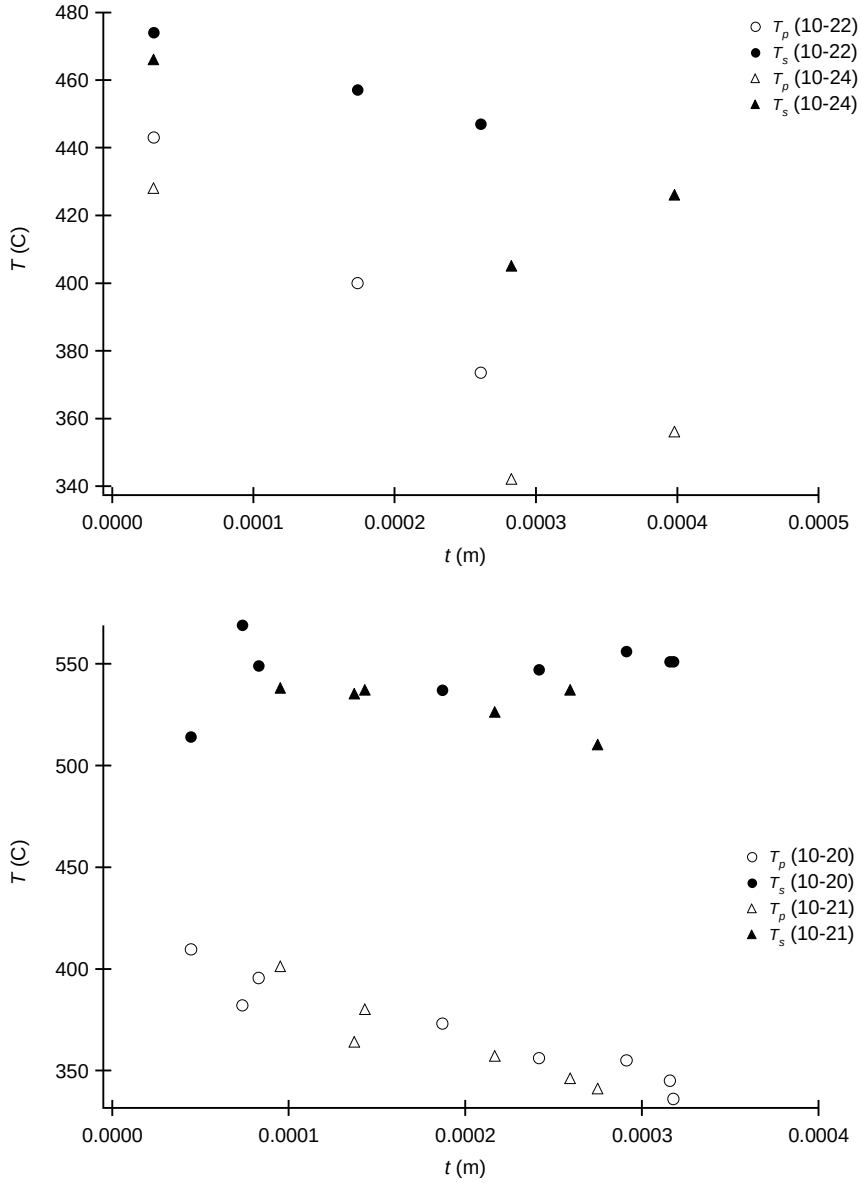

Figure 4-15. Ash Deposit Surface Temperatures and Probe Surface Temperatures vs. Deposit Thickness:
top panel - IL #6 Crown III Coal, Reducing Conditions
bottom panel - WY Corederro Coal, Reducing Conditions

The temperature difference shown in the top panel of Figure 4-15 is considerably less than for the corresponding coal under oxidizing conditions. Also, the deposit surface temperatures shown in Figure 4-15 for the IL #6 Crown III coal decrease with deposit thickness. This behavior is likely due to the lower heat flux into the probe, as compared with that measured for the same coal under oxidizing conditions. Under reducing conditions, cooler temperatures result from the increased fuel-to-air ratio. Figure 4-16 shows the heat flux plotted vs. deposit thickness for the IL #6 Crown III coal under reducing conditions, which is much less than the heat flux for the same coal under oxidizing conditions, shown in Figure 4-20.

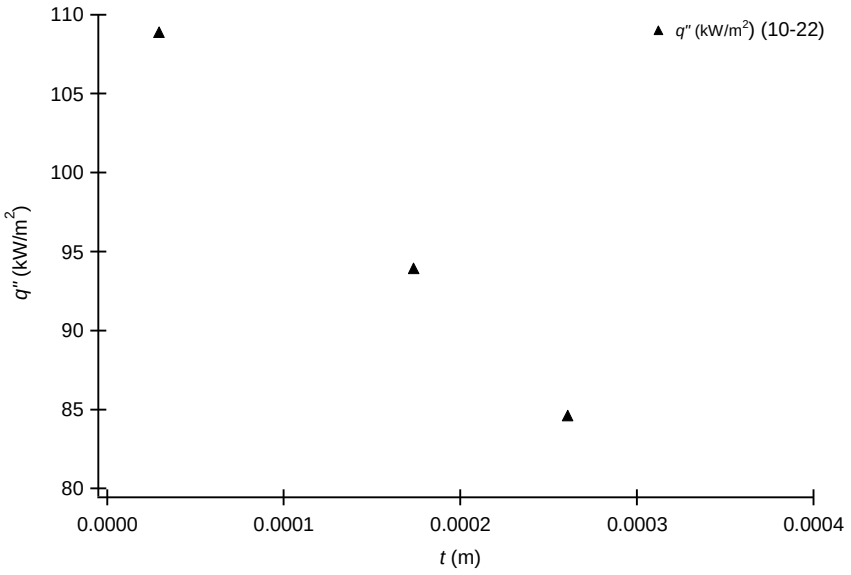

Figure 4-16. Heat Flux vs. Deposit Thickness for IL #6 Crown III Coal, Reducing Conditions

The two upstream and two downstream temperatures of the cooling-air inside the probe were also recorded by LabVIEW, together with the four surface temperatures. They were also correlated with θ and were then used to calculate a mixed mean

temperature at the upstream and downstream ends of the deposit probe test section. The mixed mean temperatures were used to determine the total energy transfer rate into the probe through the test section.

4.7.5 Thermal Conductivity

In order to calculate the effective thermal conductivity of the accumulated ash deposit, values for the total heat transfer rate, deposit thickness, probe temperature, and ash surface temperature were necessary.

Consider a control volume bound by the inside of the probe that is the length of the probe test section (0.00762 m), as illustrated in Figure 4-17. By assuming a sufficiently thin probe wall and that a uniform ash deposit thickness exists across the length of the test section (one-dimensional), the heat transfer through the probe wall by conduction was considered equal to the heat transfer to the air inside of the probe by convection.

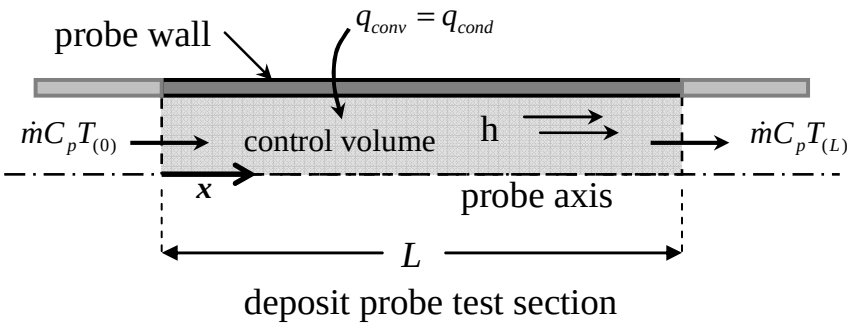

Figure 4-17. Control Volume for Energy Balance on Ash Deposit and Deposit Probe Test Section

The rate of heat transfer into the control volume was found by computing the change in the internal energy of air flowing through the control volume, and is expressed by

$$\dot{Q} = \dot{m} C_p \left(T_{m,0} - T_{m,L} \right) \tag{4-4}$$

where the mass flow rate, in kg/s, was determined by Eq. (4-3). $T_{m,0}$ and $T_{m,L}$ are the mixed-mean temperatures evaluated at the entrance ($x = 0$) and exit ($x = L$) of the deposit probe test section. The calculation of a mixed-mean air temperature T_m was not trivial and is described here:

The rate of energy entering the control volume was expressed as the product of the fluid's specific heat, temperature, velocity, and density, integrated over the cross-sectional area of the probe.

$$\dot{Q} = \int_A C_p T u \rho dA = \dot{m} C_p T_m \tag{4-5}$$

Noting that C_p remains nearly constant, Eq. (4-5) may be rearranged and T_m expressed as

$$T_m = \frac{\int_A T u \rho dA}{\dot{m}} \tag{4-6}$$

The mass flux was also defined as a product of the velocity and density integrated over the cross-sectional area of the probe:

$$\dot{m} = \bar{u}\bar{\rho}A = \int_A u\rho dA \tag{4-7}$$

By invoking the ideal gas law (relatively dry air), the density was rewritten in terms of pressure, the gas constant for air, and temperature:

$$\rho = \frac{P}{R_{air}T} \tag{4-8}$$

Substituting Eqs. (4-7) and (4-8) into Eq. (4-6) yielded a mixed-mean temperature written as

$$T_m = \frac{\int_A Tu\rho dA}{\int_A u\rho dA} = \frac{\int_A \left(\frac{P}{R_{air}T}\right) TudA}{\int_A \left(\frac{P}{R_{air}T}\right) udA} \tag{4-9}$$

Over the cross-sectional area of the probe, the pressure and the gas constant for air were constant and could be canceled out of the expression in Eq. (4-9):

$$\frac{\int_A \left(\frac{P}{R_{air}T}\right) TudA}{\int_A \left(\frac{P}{R_{air}T}\right) udA} = \frac{\int_A udA}{\int_A \left(\frac{1}{T}\right) udA} \tag{4-10}$$

The mixed-mean temperature was thus expressed as the integral over r and θ:

$$T_m = \frac{\int_A u dA}{\int_A \frac{u}{T} dA} = \frac{\int_0^{2\pi}\int_0^R u r dr d\theta}{\int_0^{2\pi}\int_0^R \frac{u}{T} r dr d\theta} \quad \textbf{(4-11)}$$

Eq. (4-11) can be evaluated at $x = 0$ and $x = L$ to determine $T_{m,0}$ and $T_{m,L}$. Subsequently, the total heat rate into the probe, $\dot{Q}$, may be determined from Eq. (4-4).

The cooling-air flow through the probe was turbulent, with Reynolds numbers (Re_D) in the range of 25000 to 30000. Buoyancy effects within the flow, due to asymmetric heating, can be quantified by comparing the computed Grashof and Reynolds numbers of the fluid. The Grashof number, Gr_L, based on a characteristic length, L, is defined in Eq. (4-12) [22].

$$Gr_L = \frac{g\beta(T_s - T_\infty)L^3}{\nu^2} \quad \textbf{(4-12)}$$

T_s is the surface temperature, T_∞ is the free stream fluid temperature, and ν is the dynamic viscosity of the fluid. For this case, the characteristic length was the diameter of the probe. The expansion coefficient, β, is defined for an ideal gas in Eq. (4-13).

$$\beta = -\frac{1}{\rho}\left(\frac{\partial \rho}{\partial T}\right)_P = \frac{1}{T} \quad \textbf{(4-13)}$$

The ratio given by Eq. (4-14) provides an appropriate comparison of the buoyancy force to the viscous force. A ratio much less than 1.0 indicates that the buoyancy effects within the flow may be considered negligible [22].

$$\frac{Gr_L}{\mathrm{Re}_D{}^2} << 1.0 \qquad \textbf{(4-14)}$$

The ratio calculated by Eq. (4-14) was determined to be $O(.0001)$. Consequently, the velocity distribution used in Eq. (4-11) is considered a function of radius (r) only and follows an assumed $1/6^{th}$ power law profile with respect to radius:

$$u(r) = u_{cl}\left(1 - \frac{r}{R}\right)^{1/6} \qquad \textbf{(4-15)}$$

This profile is for turbulent flow and n was determined from the empirical relation [23]:

$$n = -1.7 + 1.8 \log \mathrm{Re}_U \qquad \textbf{(4-16)}$$

For the typical Reynolds numbers computed (Re_U = 20000 to 30000), Eq. (4-16) yielded values for n of approximately 6.0. (Calculations of T_m, using the profile in Eq. (4-15), resulted in a 2% to 3% change with n varying from 5 to 7.) In Eq. (4-15) the centerline velocity, u_{cl}, was obtained using the known total mass flow rate, the average density, the inner diameter of the tube, and the profile given in Eq. (4-15).

The temperature of the cooling air, as a function of radius, was characterized by fitting a power-law profile through plotted data points of temperature vs. radial location across the inner diameter of the deposit probe. Figure 4-18 shows a plot of the measured temperature as a function of normalized radius at four theta locations.

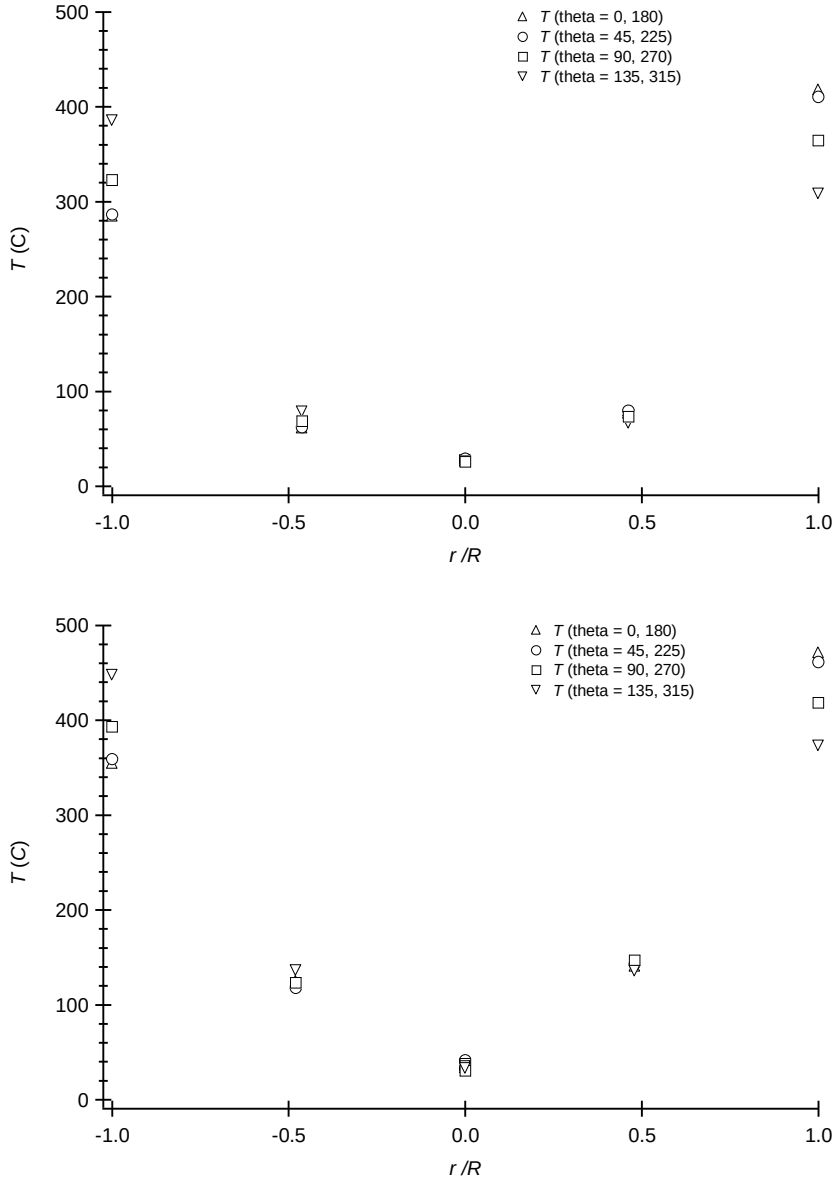

Figure 4-18. Cooling-Air Temperature vs. Normalized Radial Position at Tangential Locations θ = 0˚ and 180˚, 45˚ and 225˚, 90˚ and 270˚, 135˚ and 315˚; IL #6 Crown III Coal:
top panel – Upstream Location, x = 0
bottom panel – Downstream Location, $x = L$

Recall that three temperature measurements of the cooling-air were obtained with tangential position: at the inner probe surface ($r = R$), at ½ of the inner radius ($r = R/2$), and at the axis of the probe ($r = 0$). By aligning the temperatures recorded at tangential positions 180˚ apart from each other, the temperature distribution across the probe diameter was obtained, with known temperature measurements at five points. The corresponding measurements taken at 180˚ are also plotted to show the temperature distribution across the probe's internal diameter. The temperatures in the top panel of Figure 4-18 were measured at the upstream edge of the deposit probe test section ($x = 0$), and the temperatures shown in the bottom panel were for the downstream edge of the deposit probe test section ($x = L$). Notice that the temperature distributions in Figure 4-18 are asymmetric. This is due to the temperature variation across the probe, with the top of the probe being hotter than the bottom of the probe. The power-law, defined by Eq. (4-17), was fitted to the temperature data in Figure 4-18.

$$T(r) = T_{r=0} + \left(T_{r=R} - T_{r=0}\right)\left(1 - \frac{r}{R}\right)^{1/n} \qquad \textbf{(4-17)}$$

$T_{r=0}$ is the axial temperature, $T_{r=R}$ is the inner wall temperature of the probe, r is the radial location, and R is the inner radius of the deposit probe [22]. Figure 4-19 shows a comparison between the temperatures measured at the tangential locations of $\theta = 45^{\circ}$, 225˚ and the fitted power-law profiles, with $n = 2.15$ and $n = 3.8$ for the upstream and downstream axial locations, respectively.

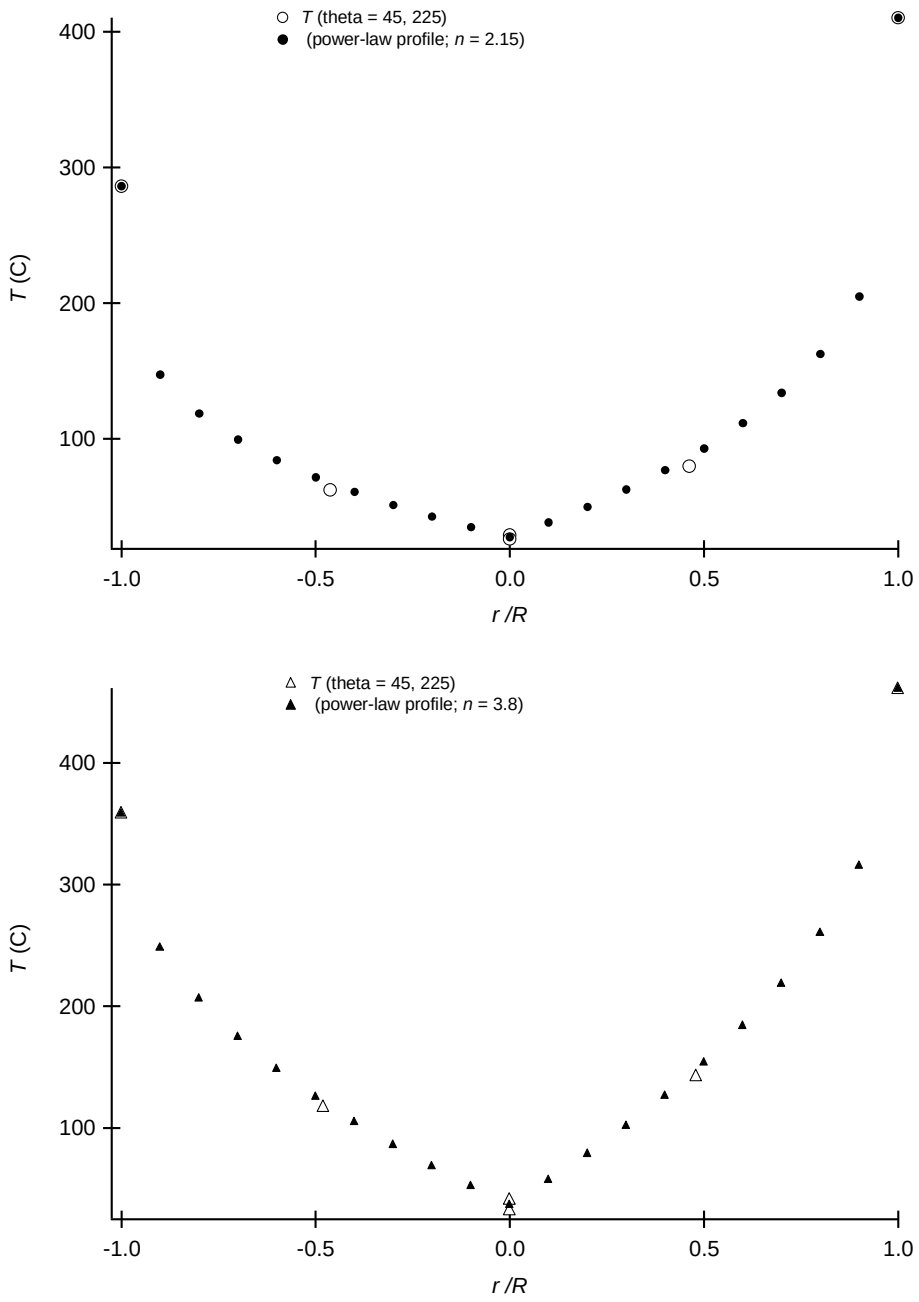

Figure 4-19. Cooling-Air Temperatures vs. Normalized Radial Position for Tangential Location θ = 45˚, 225˚; IL #6 Crown III Coal:
top panel - Upstream Location, x = 0
bottom panel - Downstream Location, $x = L$.

Power-law curves were fit to profiles across the probe diameter at four θ locations (as indicated in Figure 4-18): θ = 0˚ and 180˚, θ = 45˚ and 135˚, θ =90˚ and 270˚, and θ =135˚ and 315˚. Fit power-law profiles to at these four tangential locations resulted in

the same values for *n*, indicating little tangential variation and that the fitted power-law is adequately determined using data from the four tangential locations. The examination of a fit power-law profile to the data from separate experiments showed values of *n* which ranged from 2.0 to 2.2 for the upstream location ($x = 0$) and from 3.6 to 3.9 for the downstream location ($x = L$). Eq. (4-11) was numerically integrated using the measured temperatures and fitted power-law profile of Eq. (4-17).

The effective thermal conductivity was calculated using the computed heat transfer rate, $\dot{Q}$, the probe temperatures, the ash surface temperatures (from the FTIR spectrometer) and the deposit thickness. Two approaches to determine the effective thermal conductivity are presented. The first approach utilizes Eq. (4-18). Written, using cylindrical coordinates, k_e was defined as

$$k_e = \frac{q''(R+t)\ln\left(\frac{R+t}{R}\right)}{(T_s - T_p)} \qquad \textbf{(4-18)}$$

where R is the *outer* radius of the probe and t is the deposit thickness. The surface temperature of the ash deposit, T_s, and the surface temperature of the probe, T_p, are both evaluated at the FTIR spectrometer target spot. This calculation of effective thermal conductivity assumed a uniform heat flux through the deposit over the probe test section, defined by Eq. (4-19).

$$q'' = \frac{\dot{Q}}{\pi D_{in} L} \tag{4-19}$$

This approach is a first approximation of the heat flux and the resulting effective thermal conductivity. The heat flux, obtained using Eq. (4-19) and the recorded data for the IL #6 Crown III coal, is illustrated as a function of deposit thickness in Figure 4-20.

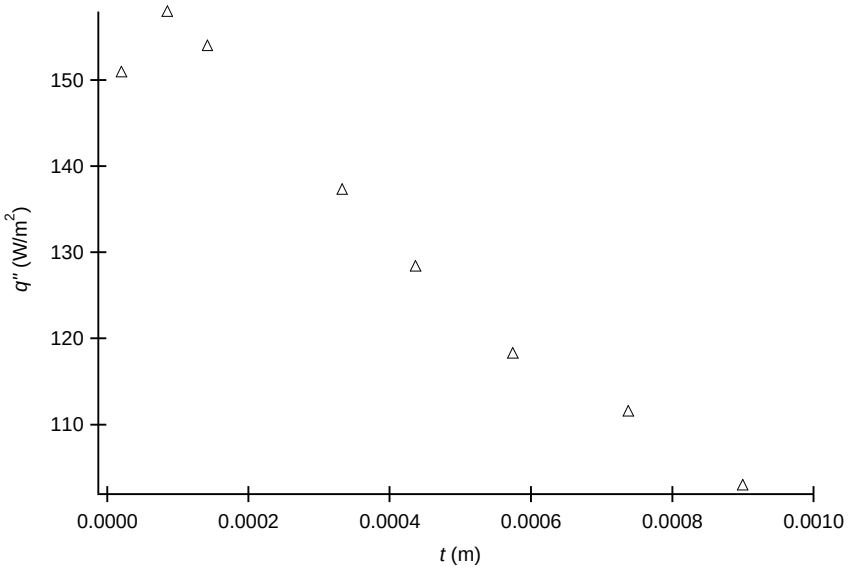

Figure 4-20. Average Heat Flux (calculated by Eq. (4-19)) vs. Deposit Thickness for IL #6 Crown III Coal, Oxidizing Conditions

The decrease in average heat flux shown in Figure 4-20 is consistent with the increase in thermal resistance due to a growing ash deposit. This plot is representative of the trends observed throughout experiments of the three coals.

A second approach to determine the effective thermal conductivity utilizes a better approximation of the heat flux. First, the heat transfer rate was equated to the total heat transfer by convection, within the probe test section:

$$\dot{Q} = \dot{m} C_p \left(T_{m,L} - T_{m,0} \right) = \int_0^L \int_0^{2\pi} \bar{h} R \left(T_p(\theta, x) - T_m(x) \right) d\theta dx \qquad \textbf{(4-20)}$$

In Eq. (4-20) $T_p(\theta, x)$ is a function of theta and axial position and $T_m(x)$ is the local mixed-mean temperature calculated by Eqs. (4-4) and (4-11). The mixed-mean temperature was assumed to be a linear function of axial position, x. In reality, the mixed-mean temperature does not vary linearly with axial position; however, analysis of flow through a pipe with a linearly-varying surface temperature (section 8.3 in Inrcopera and DeWitt [22]) showed linear behavior in T_m for the ranges of temperatures and convection coefficients in this study . The observed probe surface temperatures generally showed a linear relationship with axial position. The average convection coefficient, $\bar{h}$ was assumed to be constant and moved out of the integral of Eq. (4-20):

$$\bar{h} = \frac{\dot{m} C_p \left(T_{m,L} - T_{m,0} \right)}{\int_0^L \int_0^{2\pi} R \left(T_p(\theta, x) - T_m(x) \right) d\theta dx} \qquad \textbf{(4-21)}$$

A value for the average convection coefficient was then obtained by solving Eq. (4-21), numerically integrating the denominator. Assuming a constant value for the convection coefficient, $\bar{h}$, around the probe, the local heat flux was defined as a function of θ and x:

$$q'' = \bar{h} \left(T_p(\theta, x) - T_m(x) \right) \qquad \textbf{(4-22)}$$

In actuality the convection coefficient is not a constant over the probe test section area; however, it arguably varies less than the local heat flux. Therefore, the assumption of a constant convection coefficient in Eq. (4-20) is an improvement over the assumption of a constant heat flux utilized in Eq. (4-18) of the first approach. In the absence of conjugate heat transfer, the heat transferred to the cooling-air by convection (Eq. (4-22)) must equal the heat transferred by conduction through the uniform ash layer:

$$q'' = \bar{h}\left(T_p(\theta, x) - T_m(x)\right) = \frac{k_e\left(T_s - T_p(\theta, x)\right)}{(R+t)\ln\left(\frac{R+t}{R}\right)} \quad \textbf{(4-23)}$$

In order to determine the effective thermal conductivity using Eq. (4-23), the deposit probe temperature $T_p(\theta, x)$ was computed for the specific tangential location and axial location which corresponded to the measured ash surface temperature (obtained from the FTIR spectrometer). The effective thermal conductivity at that point could then be solved for, as expressed by Eq. (4-24):

$$k_e = \frac{\bar{h}(R+t)\ln\left(\frac{R+t}{R}\right)\left(T_p(\theta_{pt}, x_{pt}) - T_m(x_{pt})\right)}{T_s - T_p(\theta_{pt}, x_{pt})} \quad \textbf{(4-24)}$$

$T_p(\theta_{pt}, x_{pt})$ and $T_m(x_{pt})$ are the probe surface temperature and the mixed-mean temperature each evaluated at the location of the FTIR spectrometer target spot (where T_s is determined). Values for the measured surface temperature, T_s, the computed

convection coefficient, $\bar{h}$, the deposit thickness, *t*, and the probe temperature were used in Eq. (4-24) to yield an effective thermal conductivity at a particular point on the probe.

4.8 Uncertainty Analysis

The experimental uncertainty in the measurement of effective thermal conductivity was examined. The uncertainty in the effective thermal conductivity was computed by Eq. (4-25):

$$u_k = \sqrt{\left(\frac{\partial k}{\partial q''} u_{q''}\right)^2 + \left(\frac{\partial k}{\partial t} u_t\right)^2 + \left(\frac{\partial k}{\partial \Delta T} u_{\Delta T}\right)^2} \qquad \textbf{(4-25)}$$

The primary components of the uncertainty in effective thermal conductivity (Eq. (4-25) were the uncertainty in the heat flux $u_{q''}$, in the deposit thickness u_t, and in the temperature difference across the ash deposit $u_{\Delta T}$. Each of these components was further computed from other sources of uncertainty. Additional details and equations for the uncertainty calculations are provided in Appendix B. All of the components of uncertainty are summarized in Table 4-2. Note in the table that uncertainties are expressed as a percentage except for the instrument uncertainties. Also, the wide range of uncertainties reported for measurements such as the effective thermal conductivity and the heat transfer rate result from the range of deposit thicknesses measured: the lower uncertainty was computed for deposits on the order of 1.0 mm thick while the higher uncertainty was for deposits on the order of 0.1 mm thick.

Table 4-2. Components of Uncertainty in the Measurement of Effective Thermal Conductivity

Component Uncertainties		
measurement	**units**	**% uncertainty in measurement**
effective thermal conductivity		
for constant q''	W/m·K	19 to 50
for constant $\bar{h}$	W/m·K	13 to 50
heat transfer rate into probe test section		
for constant q''	kW	15.5 to 16.3
for constant $\bar{h}$	kW	6.7 to 8.8
mass flow	kg/s	3.5 to 3.7
specific heat of cooling-air	kJ/kg·K	2.0
mixed mean temp. diff. across probe test section	K	3 to 5
measurement of internal area of the probe	m^2	0.05
measurement of the internal radius of the probe	m	0.03
cooling-air inlet density	kg/m^3	7.6
correction factor for pressure calibration	kPa	2.5
atmospheric pressure meas.	kPa	2.5
temperature of cooling-air inlet	K	9.5
velocity of cooling-air through probe	m/s	11.6
temperature of cooling air inside probe	K	4.5 to 5.0
centerline velocity of cooling-air in probe	m/s	11.4
radial position inside probe	m	0.07
average cooling-air velocity inside probe	m/s	11.2
ash deposit thickness	m	9 to 50
uniformity of ash deposit thickness		7 to 33
Temperature difference across the ash deposit (from probe thermocouples and FTIR instrument)		
oxidizing	C	4 to 10
reducing with snorkel	C	11 to 42
oxidizing with coal on and probe rotation	C	17 to 33
Instrument Uncertainties		
instrument	**units**	**value**
cooling-air meter volume flow rate	standard liters/minute	7 (SLM)
profilometer instrument	m	0.0000609 (m)
position of the probe surface	m	0.0000381 (m)
thermocouple instrument	C	1.5 (C)

The analysis of error, due both to the instruments themselves and to the measurements, showed that uncertainty in the deposit thickness was the primary contributor to error in the measurements of effective thermal conductivity for deposits less than about 0.4 mm.

The majority of error in measuring the deposit thickness came from the uncertainty in the uniformity of the deposit thickness over the probe test section. For thicker deposits, uncertainty in the overall heat transfer rate became the greatest contributor of error in the effective thermal conductivity. (Uncertainty in the heat transfer rate stemmed mostly from uncertainty in the mixed-mean temperature difference across the deposit probe test section and uncertainty in the mass flow rate of the cooling-air). For deposits which were on the order of 1.0 mm thick, uncertainty in k_e ranged from 13% to about 20%. Similarly, the ranges presented in Table 4-2 reflect the lower uncertainty in thicker deposits and the higher uncertainty in thinner deposits. Importantly, the analysis showed that deposits thinner than about 0.10 mm generally could not be measured with a reasonable degree of uncertainty (less than ±50%).

5 Results

In-situ experimental measurements of the effective thermal conductivity were obtained for three different coals: Illinois #6 coal from the Patiki mine, Illinois #6 coal from the Crown III mine, and Wyoming coal from the Corederro mine. The two IL coals are bituminous while the WY coal is sub-bituminous. Analyses of each are included in Tables A-3, A-4, and A-5 in Appendix A. The ash content (% mass) is similar for the three coals. However, ash from the IL #6 coals contains significantly more silica and ferric oxide. The WY coal, in turn, has much more calcium oxide. A typical deposit is pictured in Figure 5-1.

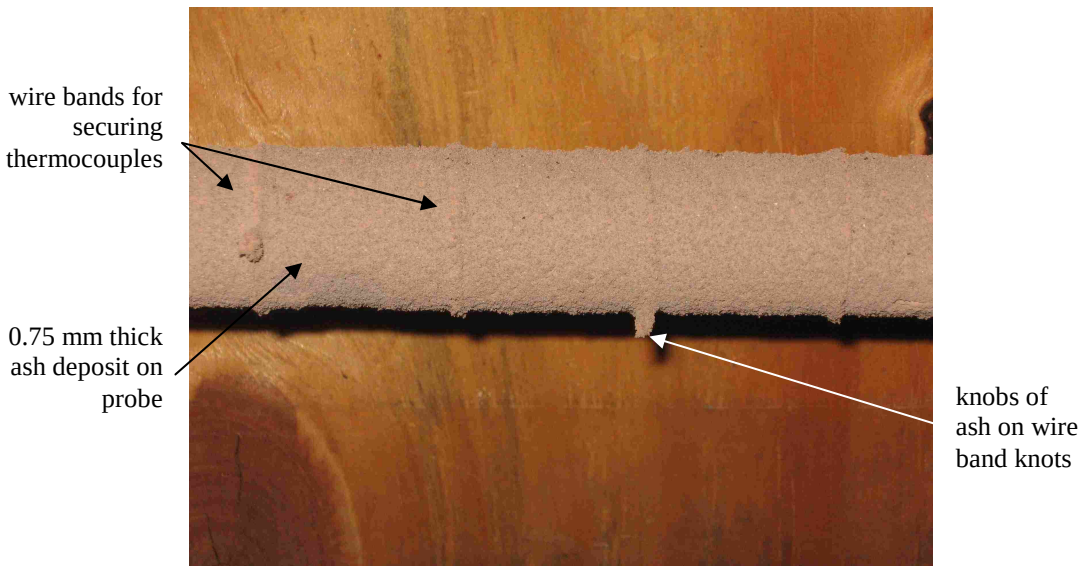

Figure 5-1. Photo of an Approximately 0.75-mm Thick Ash Deposit Collected on the Instrumented Deposit Probe: IL #6 Patiki Coal, Oxidizing Conditions

The large “knobs” on the deposit in the picture are ash collected on the knots of twisted wire where the wire bands secured the thermocouples around the deposit probe test section. Ash deposits from all three coals were characterized under oxidizing conditions, and deposits from the IL #6 Crown III and WY Corederro coals were measured under reducing conditions.

5.1 Effective Thermal Conductivity: Oxidizing Conditions

The effective thermal conductivity of ash deposits created under oxidizing conditions was determined for three coals. They were analyzed using the two approaches outlined in “Data Analysis” in Chapter 4. The effective thermal conductivity was computed from measurements of the deposition probe temperatures, the deposit surface temperatures acquired from the FTIR spectrometer, the cooling-air temperatures, and the cooling-air mass flow rates. Two experimental runs of the IL #6 Crown III and WY Corederro coals were conducted using the experimental procedure outlined previously. (See the section “Experimental Procedure” in Chapter 3.) The stoichiometry for each experiment was calculated using the $\%O_2$ measurement from the gas analyzer and the mass flow rates of air and coal. The stoichiometry was characterized by an equivalence ratio, defined by Eq. (5-1), as the stoichiometric air-to-fuel ratio divided by the actual air-to-fuel ratio. Thus, for fuel-lean conditions $\Phi < 1$ and for fuel-rich conditions $\Phi > 1$.

$$\Phi = \frac{\left(A/F\right)_{stoic}}{\left(A/F\right)_{act}} \qquad \textbf{(5-1)}$$

Figure 5-2 plots the results for the measured effective thermal conductivity, k_e vs. deposit thickness for the two coals.

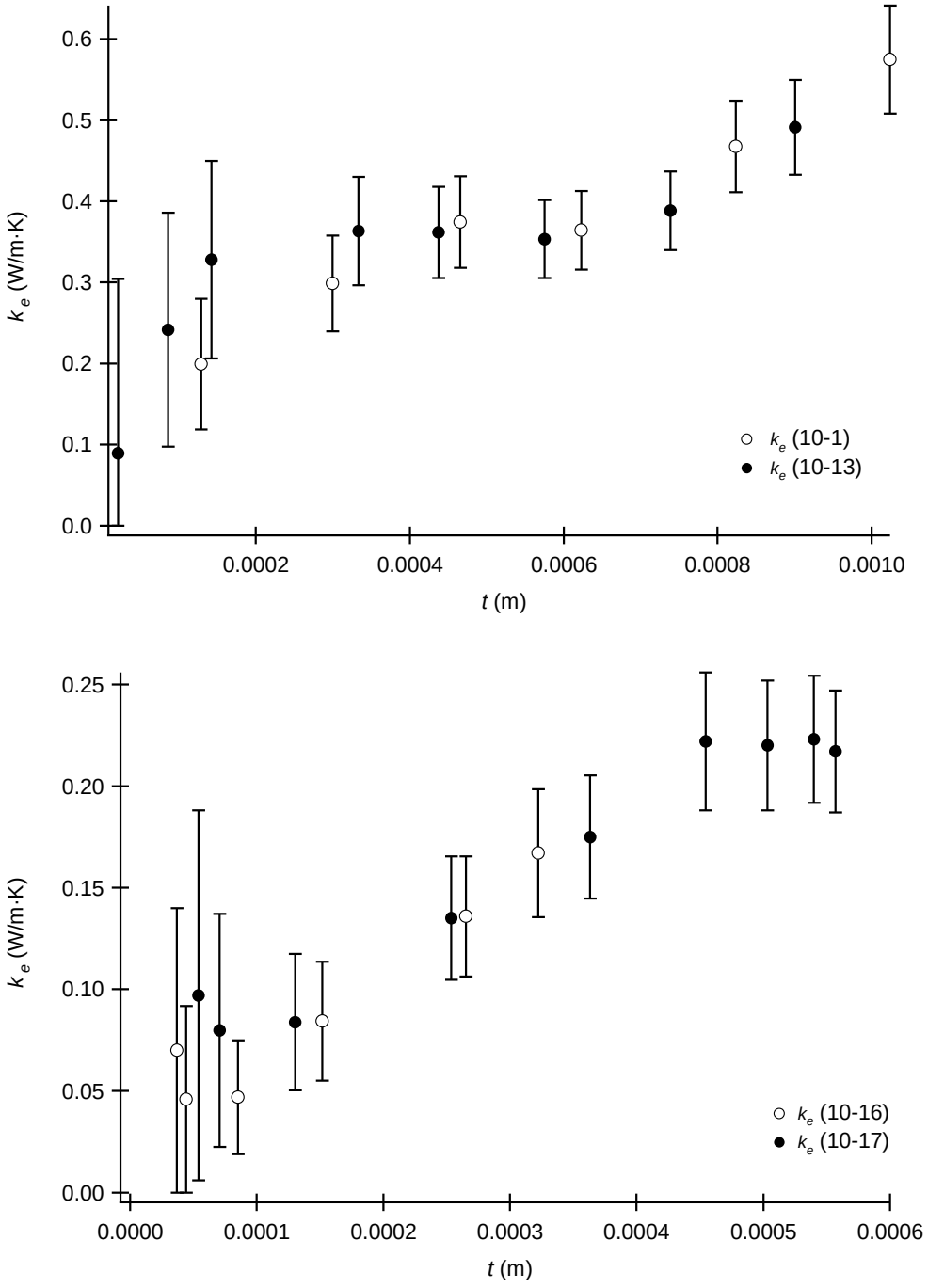

Figure 5-2. Effective Thermal Conductivity (Eq. (4-18)) vs. Deposit Thickness:
top panel - IL #6 Crown III Coal, Oxidizing Conditions (Φ = 0.73)
bottom panel - WY Corederro Coal, Oxidizing Conditions (Φ = 0.71)

The IL #6 Crown III and WY Corederro coals were fired fuel-lean, with equivalence ratios of 0.73 and 0.71 respectively. Two experiments using the IL#6 Patiki coal were also conducted under oxidizing conditions (equivalence ratio of 0.92); however, the surface temperature measurements made by the FTIR spectrometer differed in two important ways. First, the measurements were made with the probe rotating, and second, they were made with the coal being fired in the reactor. No snorkel was used to view the probe through the ash and gas. These differences produced a slight increase in the uncertainty of the measured effective thermal conductivity of this coal.

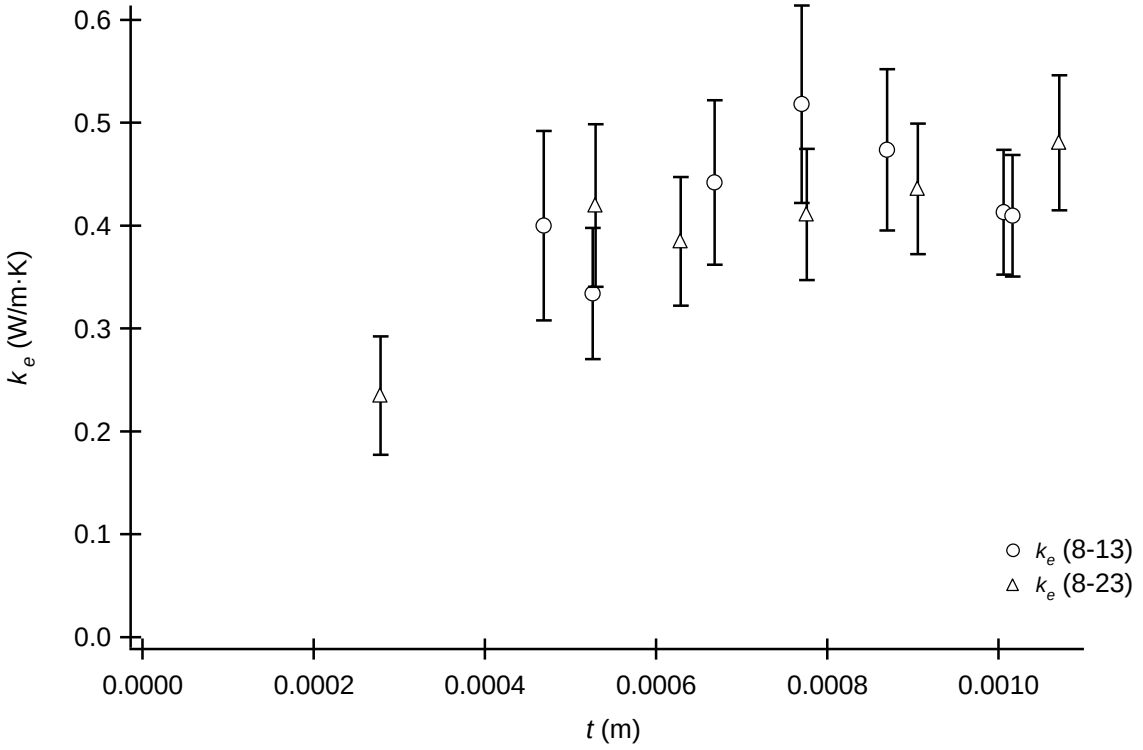

Figure 5-3. Effective Thermal Conductivity (Eq. (4-18)) vs. Deposit Thickness: IL #6 Patiki Coal, Oxidizing Conditions (Φ = 0.92)

The effective thermal conductivity, calculated by the second approach (using the heat flux derived as a function of θ and x; see Eq. (4-24)), was also determined from the same data for the six experiments (three coals). For comparison of the effective thermal conductivity computed using both approaches, the data from the two experimental runs of IL #6 Crown III coal are presented in Figure 5-4.

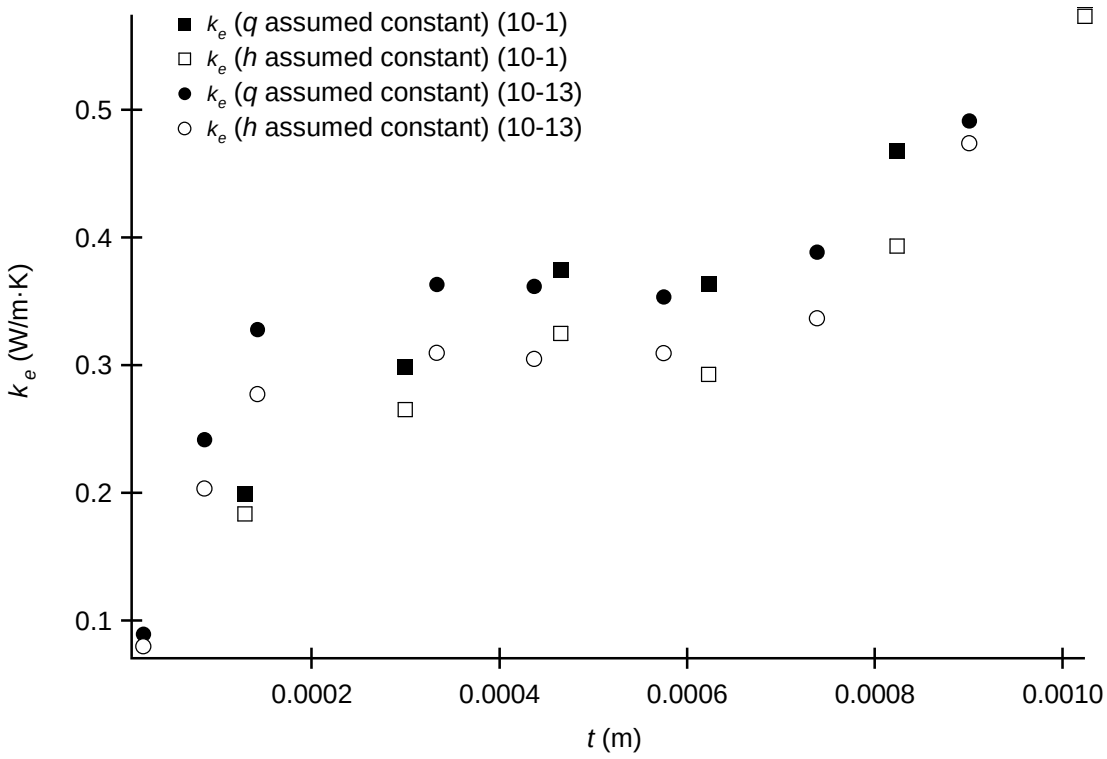

Figure 5-4. Comparison of Effective Thermal Conductivity Calculated using Both Approaches (Eqs. (4-18) and (4-24)): IL #6 Crown III Coal, Oxidizing Conditions (Φ = 0.73)

Comparison of the trends in k_e vs. t shows good agreement between the effective thermal conductivity obtained using both approaches. The magnitude of the effective thermal conductivities calculated by the second approach (from q'' as a function of θ and x) is observed to average 14% less than that calculated by the first approach (from a constant

q''). This behavior is consistent for the IL #6 coals, while for the WY Corederro coal, under oxidizing conditions, the average decrease was closer to 18%. The difference in k_e between the two approaches exists because the second approach utilizes the local heat flux at the point on the probe where the FTIR spectrometer measures the deposit surface temperature. This point is below the center of the probe. The heat flux and temperature difference across the ash deposit at this point are, therefore, less than their average values (which are used in the first approach). This second approach results in a more robust characterization because variations in the local heat flux are more appropriately accounted for.

Figure 5-5 shows the results of effective thermal conductivity for the WY Corederro and IL #6 Patiki coals, computed using the second approach. Note in Figure 5-5 that the thickness range (x axis) is smaller for the WY Corederro coal compared with that of the IL #6 Crown III coal. The WY Corederro coal exhibited different deposition characteristics, including ash particle size (smaller), from those of the IL #6 coals. While differences in the ash particles and deposit microstructure among the coals were not directly measured, they were clearly observed in the experimental runs, and they are thought to account for the discrepancy in deposit thicknesses obtained in comparable amounts of time for the IL #6 and WY coals. The slower deposition rate for the WY Corederro coal can be seen clearly, compared with the IL #6 Crown III coal, in Figure 5-6.

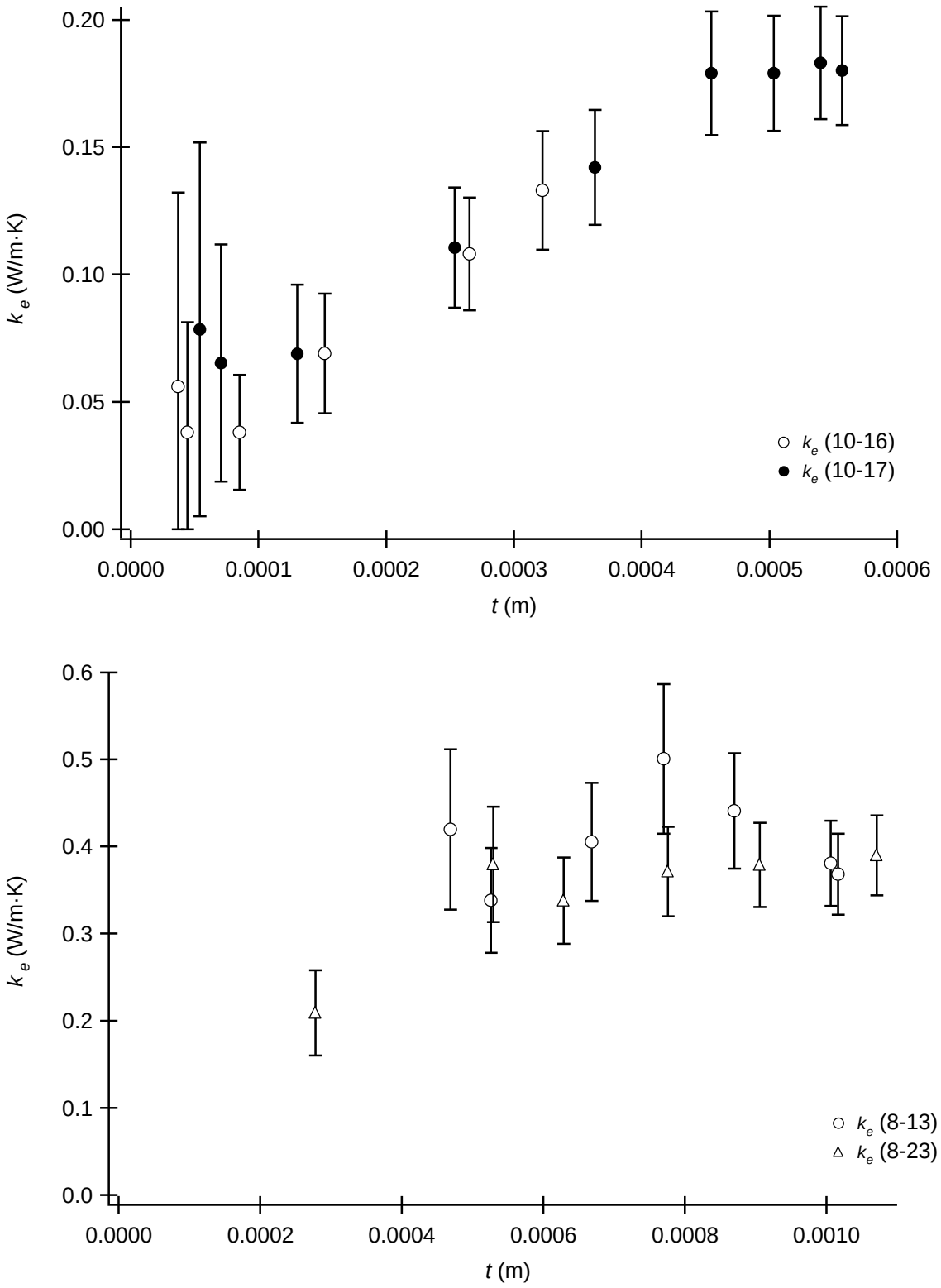

Figure 5-5. Effective Thermal Conductivity (Eq. (4-24)) vs. Deposit Thickness: top panel - WY Corederro Coal, Oxidizing Conditions (Φ = 0.71), bottom panel - IL #6 Patiki Coal, Oxidizing Conditions (Φ = 0.92)

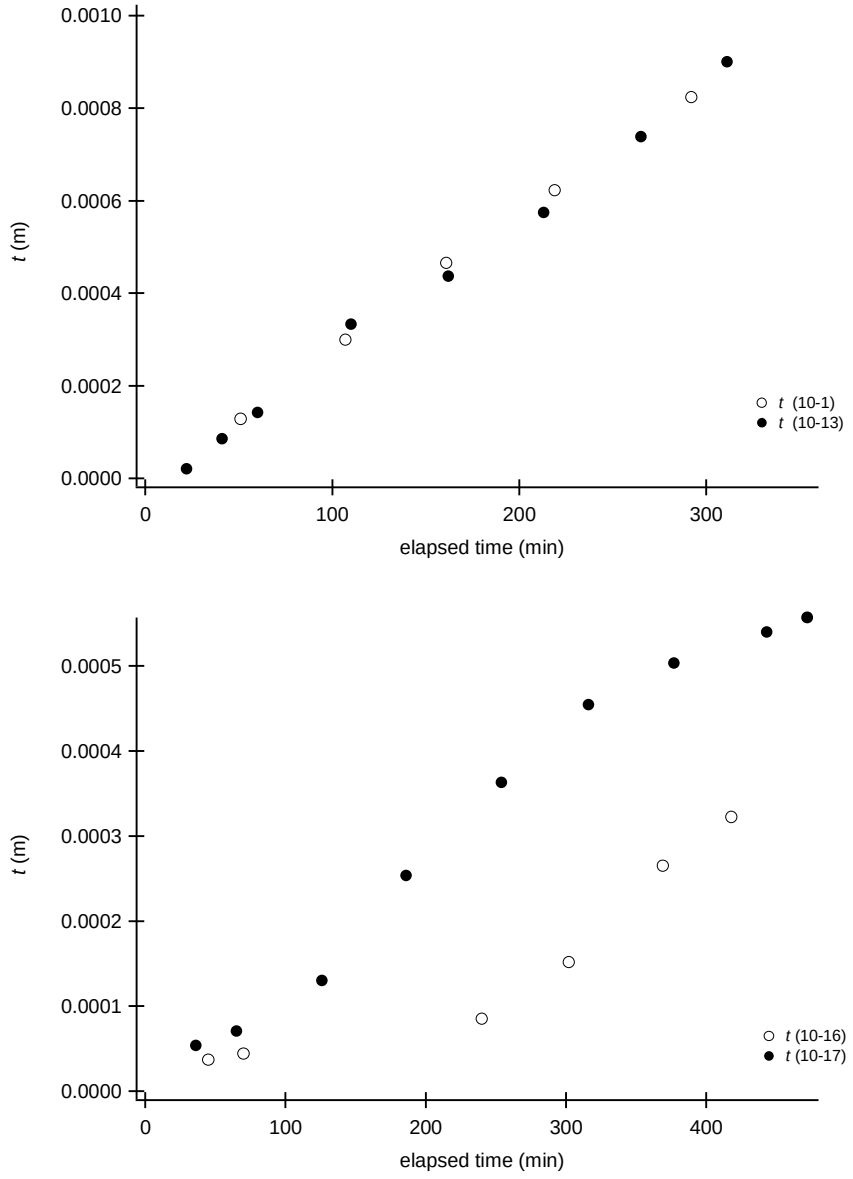

Figure 5-6. Deposit Thickness vs. Elapsed Time:
top panel - IL #6 Crown III Coal, Oxidizing Conditions
bottom panel - WY Corederro Coal, Oxidizing Conditions

Due to limitations in the time required to perform an experiment, generally thinner deposits were collected for the WY Corederro coal. Over the range of thicknesses measured, the WY Corederro coal has a lower effective thermal conductivity (0.05 to 0.20), measuring an average of 60% lower than that of the IL #6 Crown III coal.

The behaviors of the k_e vs. t data for the IL #6 Patiki and the IL #6 Crown III coal follow each other relatively well, with the IL #6 Patiki coal showing a slightly lower effective thermal conductivity for thinner deposits. This close correlation can be expected since these two coals are both bituminous, and they share more in common with each other than with the sub-bituminous WY Corederro coal.

Each of the three coals exhibited an upward trend in effective thermal conductivity with thickness. This behavior is physically realistic, since it is likely that some degree of sintering occurred as the ash deposits grew. Sintering could occur due to both the increase in temperature of the deposit (nearer the surface) and the increased length of time the deposit had been subject to its high-temperature surroundings. In his work with ash deposits obtained from IL #6 coals fired in the same laboratory reactor, Blanchard performed experiments on particle size and deposition rates. He reported ash particle distributions (for ash collected on a deposit probe similar to the one used in this study) and for fly ash. The distribution data showed larger ash particles on the probe than in the sampled fly ash, indicating that sintering did occur [21]. Also, Anderson reported light sintering in deposits of fly ash, subject to temperatures similar to those observed in this work, which resulted in a few percent increase in k_e [17]. Reasonably, similar sintering occurred in the ash deposits investigated in this work. Possibly, settling of the loose ash particles in the deposit contributed to the increase in k_e with time and deposit thickness. The effective thermal conductivity was observed to increase with deposit thickness for all coals and conditions explored. Effective thermal conductivities of the IL #6 Crown III coal ranged from about 0.3 to 0.5 W/m·K over the range of deposit thicknesses measured. The IL #6 Patiki coal had a range from 0.2 to 0.4 W/m·K. The

effective thermal conductivities of the WY Corederro coal exhibited the smallest magnitudes and ranged from 0.05 to 0.175 W/m·K. Notably, the rate of increase in k_e with deposit thickness decreases significantly around 0.4 mm.

5.2 Effective Thermal Conductivity: Reducing Conditions

Experimental data was taken for deposits formed under reducing conditions for two of the coals, IL #6 Crown III and WY Corederro. Two experiments for each coal were performed. The equivalence ratios obtained before adding methane were 0.90 and 0.93 for the IL #6 Crown III and WY Corederro coals, respectively. The reducing equivalence ratios at the reactor exit for the two coals were 2.33 and 3.1, respectively. The results for the effective thermal conductivity, determined using the first approach (Eq. (4-18)), are presented in Figure 5-7. The same data was again analyzed to determine the effective thermal conductivity by the second approach (Eq. (4-24)), and the results are displayed in Figure 5-8. Note that these plots show a similar average decrease of about 14% in the effective thermal conductivity from their corresponding values computed using the first approach. Time restrictions and the challenges of producing (and maintaining) reducing conditions resulted in fewer measurements for both of the coals in reducing conditions. Note in Figure 5-7 the greater uncertainty in k_e for the reducing data than for the oxidizing data. The added uncertainty resulted from measurements with the FITR spectrometer made with the coal burning (necessary for maintaining reducing conditions).

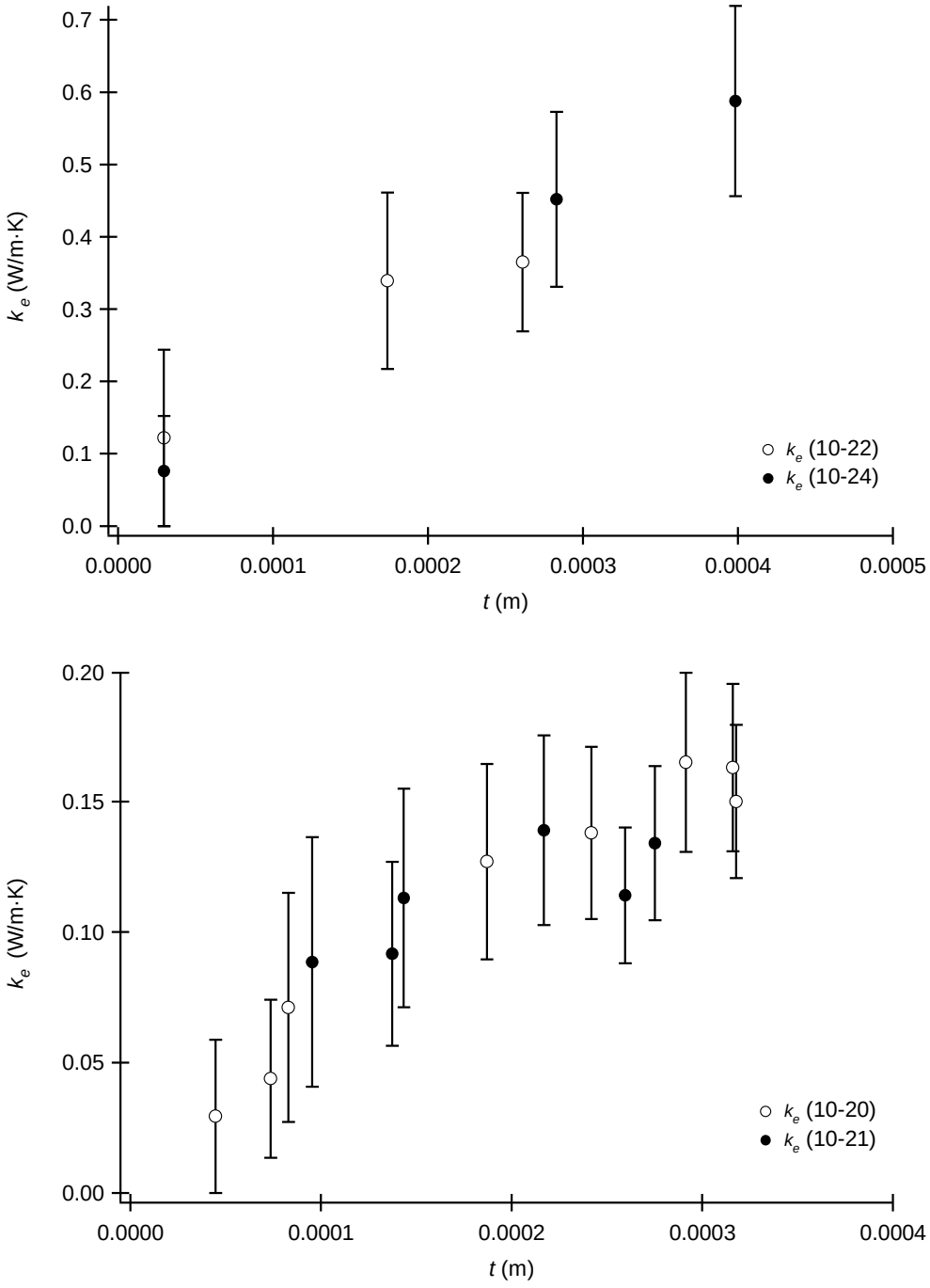

Figure 5-7. Effective Thermal Conductivity (Eq. (4-18)) vs. Deposit Thickness:
top panel - IL #6 Crown III Coal, Reducing Conditions (Φ = 2.33)
bottom panel - WY Corederro Coal, Reducing Conditions (Φ = 3.10)

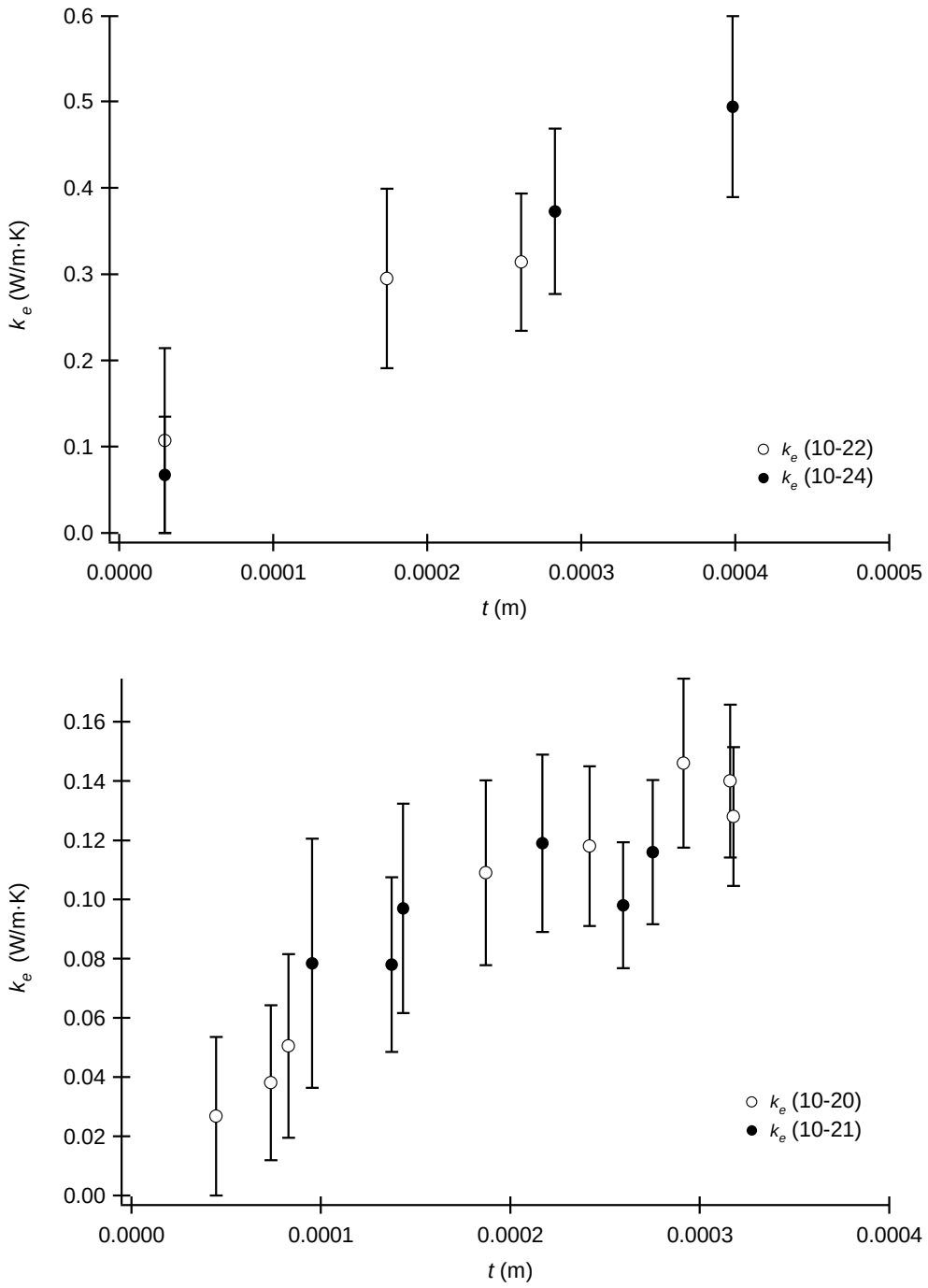

Figure 5-8. Effective Thermal Conductivity (Eq. (4-24)) vs. Deposit Thickness:
top panel - IL #6 Crown III Coal, Reducing Conditions (Φ = 2.33)
bottom panel - WY Corederro Coal, Reducing Conditions (Φ = 3.10)

The use of a snorkel allowed the FTIR spectrometer to measure the ash surface through the coal. While the snorkel eliminated most of the ash and exhaust gases in the

optical path, some combustion products still flowed through the path, between the end of the snorkel and the deposit. This interference in the optical path contributed additional error to the measurement of the deposit surface temperature. In order to quantify the error in the measured surface temperature under these conditions, measurements of the clean deposit probe where taken using the FTIR spectrometer, with one of the surface thermocouples directly next to the target spot. Measurements of the probe, while coal was burning (reducing conditions) and with no coal, were compared.

In a comparison of the two coals, the WY Corederro coal again exhibited a much lower effective thermal conductivity (k_e = 0.05 to 0.14, calculated by the first approach). For the IL #6 Crown III in reducing conditions, the data show a marked increase of 15% to 60% in effective thermal conductivity compared with that observed in oxidizing conditions. The WY Corederro coal compared more closely in both oxidizing and reducing conditions, but the effective thermal conductivity was also slightly greater (5% to 15%) in the reducing case. These data suggest that the effective thermal conductivity of particulate ash deposits is influenced by the stoichiometry, with reducing conditions producing deposits with higher effective thermal conductivity. Additionally, the difference in k_e between oxidizing and reducing conditions was observed to increase with thickness. This behavior indicates the possibility that sintering, and other mechanisms by which k_e increases, are accelerated in deposits under reducing conditions.

5.3 Experiment Repeatability

The degree of repeatability for the three coals tested was found to be good, as the experimental values of repeat runs fall within their respective error limits. However, due

to time restraints and to the challenges of in-situ measurements, only two experimental runs of the IL#6 Crown III and WY Corederro coals were performed under oxidizing and reducing conditions. Two experiments of the IL#6 Patiki coal were performed under oxidizing conditions.

5.4 Summary

The effective thermal conductivity was determined experimentally for three coals under oxidizing conditions and for two of the same coals under reducing conditions. A summary of the ranges of k_e for the deposits investigated is presented in Table 5-1.

Table 5-1. Summary of Ranges of Measured Effective Thermal Conductivity

oxidizing conditions	
coal	k_e
IL #6 Crown III	0.2 to 0.5
IL #6 Patiki	0.2 to 0.45
WY Corederro	0.04 to 0.18
reducing conditions	
coal	k_e
IL #6 Crown III	0.1 to 0.5
WY Corederro	0.03 to 0.15

Under oxidizing conditions, the WY Corederro coal showed a much lower effective thermal conductivity (k_e = 0.05 to 0.2) than the two IL #6 coals (k_e = 0.2 to 0.5), with similar results obtained under reducing conditions. This behavior is most likely the result of differences in the microstructure and in the chemical constituents of the ash from the IL #6 and WY coals. All of the coals exhibited an upward trend in effective thermal conductivity with increasing deposit thickness. The increase in magnitude of k_e was observed to range from 0.125 to 0.3 W/m·K. This behavior accords with the sintering

which likely occurred in the ash deposits. Also, it was found that deposits formed under reducing conditions had a higher effective thermal conductivity. Data for both coals showed an increase in k_e under reducing conditions. The IL #6 Crown III coal exhibited the greater increase, ranging from 15% to 60% of that measured for oxidizing conditions.

Values of effective thermal conductivity obtained (by using the second approach, Eq. (4-24)) in this study and values reported in literature, for comparable ash deposits at comparable temperatures (300˚ C to 600˚ C), are shown in Table 5-2.

Table 5-2. Values of Effective Thermal Conductivity

reported in literature			
k_e	**coal**	**deposit**	**reported by**
2.5 to 3.0	not specified	particulate	Wall, T. F. et al. [7]
0.10 to 0.25	blend 65% / 35% (by mass) IL #6 coal / wheat straw	particulate	Robinson A. L. et al. [11]
0.2 to 3.1	blend 65% / 35% (by mass) IL #6 coal / wheat straw	sintered	Robinson A. L. et al. [11]
0.4 to 0.5	not specified		Rezaei, H. R. et al. [10]
0.1 to 0.25	not specified	particulate	Anderson, D. W. et al. [17]
0.25 to 0.5	not specified	various crushed ("particulate")	Anderson, D. W. [5]
present work			
k_e (Eq. (4-24))	**coal**	**deposit**	
0.2 to 0.5	IL #6	particulate	
0.04 to 0.18	WY	particulate	

The IL #6 coals compare well with the values found in literature for particulate ash deposits. The effective thermal conductivity determined for the WY Corederro coal is lower, but it is still comparable to the low range of values reported by Robinson et al. and Anderson et al. [11, 17].

6 Summary and Conclusions

This work included two main objectives: 1) the development of a simple thermal transport model of an ash deposit and 2) experimental in-situ measurements of effective thermal conductivity in coal ash deposits.

The thermal transport model, which was developed supplementary to the primary focus on experimentation, was created to serve as a framework for incorporating separate existing models of thermal properties of ash deposits. The thermal transport model is unique in that it approximates a morphologically complex ash deposit using four regimes with distinct thermal characteristics. These four regimes were particulate, sintered, solidified slag, and molten slag. The model was developed to be exercised in the CFD package FLUENT, and it requires, as inputs, the thermal properties of each layer. The model then computes the heat flux, deposit surface temperature, and deposit thickness distributions with time, along a vertical boundary.

The main focus of this work was on experimental measurements of the effective thermal conductivity in ash deposits. An approach for obtaining in-situ experimental measurements of ash deposits was developed. This approach was successfully employed to measure values of effective thermal conductivity in deposits of loosely-bound particulate ash obtained from three different coals. The approach could be useful in performing future investigations of in-situ thermal properties of ash deposits. The

effective thermal conductivity for the three coals tested was determined to be quite low. The two bituminous IL #6 coal ash deposits yielded effective thermal conductivities which increased from 0.2 to 0.5 W/m·K over deposit thicknesses from 0.1 to 1.1 mm. The ash deposits of the sub-bituminous coal, WY Corederro, exhibited lower effective thermal conductivities, from about 0.06 to 0.18 W/m·K. A comparison of the effective thermal conductivity of ash deposits in either oxidizing or reducing conditions revealed a lower thermal resistance in those formed under reducing conditions. The deposits for IL #6 Crown III showed a greater increase (compared to the WY Corederro coal) of 15% to 60% in effective thermal conductivity over deposits of the same coal made under oxidizing conditions. This increase in k_e indicated that some significant differences existed in the ash thermal transport characteristics of the two coals – likely a difference in deposit morphology.

The effective thermal conductivities studied also showed that they will increase with time and deposit thickness. Data in each of the experiments exhibited this increase, strongly suggesting that the deposits underwent some degree of sintering. Comparison of the increase in k_e, for deposits under oxidizing and reducing conditions, indicates that sintering, and other mechanisms by which k_e increases, had a greater effect on the IL #6 coal than on the WY Corederro coal. Furthermore, the extent that k_e increased with thickness suggested that reducing conditions exerted a greater influence on the IL #6 coal.

Significantly, the relatively low thermal conductivity of these particulate ash deposits will dominate the thermal resistance in commercial boilers. Even very thin deposits will have a large insulative impact on heat-exchanging surfaces. The results for

the effective thermal conductivity of ash deposits from these three coals can help characterize the effects the ash has on thermal transport in boilers. The results, together with predictive models, could be used to improve the design, economize the operation, and streamline the maintenance of commercial boilers. Even small gains in the efficiency of coal-fired boilers, obtained from an increased understanding of the thermal transport behavior of ash, can have a large positive impact on this critical energy source.

6.1 Future Work

Future work involving the model for effective thermal conductivity could include a more complete hydrodynamic model for the molten slag layer. Accounting for the mass transport throughout the development of the molten slag layer (not just the steady-state) would improve the accuracy of predictions of the molten slag and solidified slag behavior. Additionally, the model could be modified to calculate the temperature throughout the entire deposit when each layer (time step) is added. This would result in a more robust model of temperature and heat flux, both spatially and temporally.

Future experiments of the effective thermal conductivity of ash deposits could be improved by reducing the measurement uncertainty. In particular, measurements of the ash deposit thickness could be improved by obtaining a more uniform deposit across the probe and by reducing the eccentricity of the rotating probe. Measurements of effective thermal conductivity would also benefit from thicker deposits. Methods could be developed to improve deposition rates, producing thicker deposits in less time.

Further investigation could focus on the effects of stoichiometry by examining more ash deposits from the same coals under different oxidizing and reducing conditions.

Microstructure and deposition behavior could be investigated to determine their effects on effective thermal conductivity. Additional work might investigate the cause of the significantly lower effective thermal conductivities observed for the WY Corederro coal. This investigation could include more experiments to determine the extent of sintering in deposits of different coals under similar conditions. Future work might also include experiments on additional types of coal.

The author would like to especially acknowledge GE Global Research for their generous funding of this work.

7 REFERENCES

1. *Generation and Consumption of Fuels for Electricity Generation, April 2007*. Electric Power Monthly 2007 April 2007 [cited 2007 7/12/2007]; Statistical information on energy consumption in the United States]. Available from: http://www.eia.doe.gov/cneaf/electricity/epm/epm_sum.html.

2. Kaer, S.K., L.A. Rosendahl, and L.L. Baxter, *Towards a CFD-Based Mechanistic Deposit Formation Model for Straw-Fired Boilers.* Fuel, 2006. **85**: p. 833-848.

3. Herzog, H., *The Economics of CO2 Capture*, ed. B.E. P Reimer, A Wokaum. 1999: Oxford: Elsevier Science Ltd. 6.

4. *Coal Gasifier*. 2008, Idaho National Laboratory.

5. Anderson, D.W., *Heat Transfer Through Coal Ash Deposits*. 1985, Purdue: West Lafayette. p. 305.

6. Benson, S.A., *Laboratory Studies of Ash Deposit Formation during the Combustion of Western U.S. Coals*. 1986, Pennsylvania State University: University Park, PA. p. 293.

7. Wall, T.F., S.P. Bhattacharya, D.K. Zhang, R.P. Gupta, and X. He, *The Properties and Thermal Effects of Ash Deposits in Coal-Fired Furnaces.* Progress in Energy and Combustion Science, 1993. **19**: p. 487-504.

8. Bockelie, M.J., M.K. Denison, Z. Chen, T. Linjewile, C.L. Senior, and A.F. Sarofim, *CFD Modeling for Entrained Flow Gasifiers*, in *Gasification Technologies Conference*. 2002: San Francisco, CA.

9. Robinson, A.L., S.G. Buckley, N. Yang, and L.L. Baxter, *Experimental Measurements of the Thermal Conductivity of Ash Deposits: Part 1. Measurement Technique*. 2000, Sandia National Laboratories: Albuquerque, NM. p. 1-26.

10. Rezaei, H.R., R.P. Gupta, G.W. Bryant, J.T. Hart, G.S. Liu, C.W. Bailey, T.F. Wall, S. Miyamae, K. Makino, and Y. Endo, *Thermal Conductivity of Coal Ash and Slags and Models Used.* Fuel, 2000. **79**: p. 1697-1710.

11. Robinson, A.L., S.G. Buckley, N. Yang, and L.L. Baxter, *Experimental Measurements of the Thermal Conductivity of Ash Deposits: Part 2. Effects of Sintering and Deposit Microstructure*. 2000, Sandia National Laboratories: Albuquerque, NM. p. 1-29.

12. Benyon, P.J., *Computational Modeling of Entrained Flow Slagging Gasifiers*. 2002, University of Sydney: Sydney.

13. Senior, C.L. and J.J. Sangiovanni, *Numerical Model of Slag Flow in a Novel Coal-fired Furnace.* International Journal of Heat and Mass Transfer, 2001.

14. Kweon, S.C., *Computational Model for Microstructure and Effective Thermal Conductivity of Ash Deposits in Utility Boilers*. 2002, Carnegie Mellon University: Pittsburgh, PA. p. 92.

15. Zbogar, A., F.J. Frandsen, P.A. Jensen, and P. Glarbord, *Heat Transfer in Ash Deposits: A Modeling Toolbox.* Progress in Energy and Combustion Science, 2005. **31**: p. 371-471.

16. Rushdi, A. and R.P. Gupta, *Investigation of Coals and Blends Deposit Structure: Measuring the Deposit Bulk Porosity Using Thermomechanical Analysis Technique.* Fuel, 2005. **84**: p. 595-610.

17. Anderson, D.W., R. Viskanta, and F.P. Incropera, *Effective Thermal Conductivity of Coal Ash Deposits at Moderate to High Temperatures.* Journal of Engineering for Gas Turbines and Power, 1987. **109**: p. 215-221.

18. Butler, B.W. and B.W. Webb, *Measurement of Radiant Heat Flux and Local Particle and Gas Temperatures in a Pulverized Coal-Fired Utility-Scale Boiler*. Energy and Fuels, 1993. **7**: p. 835-841.

19. Hwang, Y.-L. and J.R. Howell, *Local Furnace Data and Modeling Comparison for a 600-MWe Coal-Fired Utility Boiler.* journal of Energy Resources Technology, 2002. **124**: p. 56-66.

20. Vargas, S., F.J. Frandsen, and K. Dam-Johansen, *Rheological Properties of High-Temperature Melts of Coal Ashes and Other Silicates.* Progress in Energy and Combustion Science, 2001. **27**: p. 237-429.

21. Blanchard, R.P., *Measurements and Modeling of Coal Ash Deposition in an Entrained-Flow Reactor*. 2008, Brigham Young University: Provo.

22. Incropera, F.P. and D.P. DeWitt, *Fundamental of Heat and Mass Transfer*. 5 ed. 2002, Danvers: John Wiley & Sons, Inc. 981.

23. Fox, R.W., A.T. McDonald, and P.J. Pritchard, *Introduction to Fluid Mechanics*. 6 ed. 2004, Danvers: John Wiley & Sons, Inc. 787.

24. Lokare, S., *Mechanistic Investigation of Ash Deposition in Pulverized-Coal and Biomass Combustion*. 2008, Brigham Young University: Provo.

Appendix A. Supplementary Tables

Table A-1. Required Inputs for the Thermal Transport UDF

Variable	Value	Units	Description
T_{sint}	1000	K	effective sintering temperature
T_{slag}	1600	K	effective slagging temperature
k_{part}	0.5	$W/m \cdot K$	particulate ash thermal conductivity
k_{sint}	2	$W/m \cdot K$	sintered ash thermal conductivity
k_{solid}	5	$W/m \cdot K$	solidified slag thermal conductivity
k_{slag}	5	$W/m \cdot K$	molten slag thermal conductivity
$\dot{m}''$	0.00166	$kg/s \cdot m^2$	ash mass deposition rate
y_{part}	0.5	---	particulate ash mass capture fraction
y_{sint}	0.7	---	sintered ash mass capture fraction
y_{slag}	1	---	molten slag mass capture fraction
ρ_{part}	800	kg/m^3	particulate ash density
ρ_{sint}	1500	kg/m^3	sintered ash density
ρ_{solid}	2000	kg/m^3	solidified slag density
ρ_{slag}	2200	kg/m^3	molten slag density
ε_{part}	0.7	---	particulate ash emittance
ε_{sint}	0.5	---	sintered ash emittance
ε_{slag}	0.95	---	molten slag emittance
σ	5.67E-08	$W/m^2 \cdot K^4$	Boltzmann's constant

Table A-2. Fuel Analysis for the WY Corederro Coal: Proximate Analysis (% Mass Fraction), as Received [24]

Fuel (maf)	Corederro
	Untreated
C	71.45
H	6.02
N	1.1
S	0.17
O	21.26
Total	100
Ash % (mf)	7.12
Moist. % (ar)	13.64
HV, MJ/kg (maf)	29.89
SiO_2	28.7
Al_2O_3	15.5
Fe_2O_3	10.2
CaO	15.1
MgO	3.6
Na_2O	1.5
K_2O	0.8
TiO_2	1.2
MnO_2	NA
P_2O_5	1.2
SrO	NA
BaO	NA
SO_3	22
Total	100

Table A-3. Analysis for the IL #6 Crown III Coal (% Mass Fraction): Standard Laboratories
8451 River King Drive, Freeburg, IL 62243
Date Sampled: 6/27/2007
Lab # 2007-01454-001

Proximate (As Received)	Moisture	16	Mineral Analysis	SiO2	51.17
	Ash	8.52		Al203	17.33
	Volatile	35.16		Fe2O3	17.73
	Fixed Carbon	40.32		CaO	4.26
	BTU	10655		MgO	0.99
	Total Sulfur	3.33		Na2O	1.7
Proximate (Dry)	Ash	10.14		K2O	2.21
	Volatile	41.86		TiO2	0.83
	Fixed Carbon	48		MnO2	0.07
	BTU	12684		P2O5	0.25
	Total Sulfur	3.97		SrO	0.04
	MAF BTU	14115		BaO	0.04
				SO3	4.4
Ultimate (As Received)	Moisture	16		Undetermined	-1.38
	Carbon	57.95		Type of Ash	Bituminous
	Hydrogen	4.27		Silica Value	68.68
	Nitrogen	1.08		T250	2421
	Chlorine			Base/Acid	0.39
	Sulfur	3.33		lb Ash /mm BTU	
	Ash	8.52		lb SO2/mm BTU	6.25
	Oxygen (Diff.)	8.85		Fouling Index	0.66
Ultimate (Dry)	Carbon	68.99		Slagging Index	1.55
	Hydrogen	5.08			
	Nitrogen	1.29			
	Chlorine		Reducing Fusion Temp.	I.D.	1954
	Sulfur	3.97		H=W	2042
	Ash	10.14		H=1/2W	2143
	Oxygen (Diff.)	10.53		Fluid	2221
			Oxidizing Fusion Temp.	I.D.	2256
				H=W	2379
				H=1/2W	2433
				Fluid	2579
				Browning T250	2337
				B&W T250	2421

Table A-4. Analysis for IL #6 Patiki Coal (% Mass Fraction): Standard Laboratories
8451 River King Drive, Freeburg, IL 62243
Date Sampled: 6/18/2007
Lab # 2007-01334-001

Proximate (As Received)	Moisture	11.09	Mineral Analysis	SiO2	50.55
	Ash	7.17		Al203	18.23
	Volatile	37.46		Fe2O3	20.6
	Fixed Carbon	44.29		CaO	2.92
	BTU	11755		MgO	0.81
	Total Sulfur	2.9		Na2O	1.01
Proximate (Dry)	Ash	8.06		K2O	2.17
	Volatile	42.13		TiO2	0.95
	Fixed Carbon	49.81		MnO2	0.04
	BTU	13221		P2O5	0.17
	Total Sulfur	3.26		SrO	0.03
	MAF BTU	14380		BaO	0.04
				SO3	1.85
Ultimate (As Received)	Moisture	11.09		Undetermined	0.63
	Carbon	65.21		Type of Ash	Bituminous
	Hydrogen	4.59		Silica Value	67.51
	Nitrogen	1.32		T250	2421
	Chlorine			Base/Acid	0.39
	Sulfur	2.9		lb Ash /mm BTU	
	Ash	7.17		lb SO2/mm BTU	4.93
	Oxygen (Diff.)	7.72		Fouling Index	0.39
Ultimate (Dry)	Carbon	73.34		Slagging Index	1.27
	Hydrogen	5.16	Reduc. Fusion Temp.	I.D.	1942
	Nitrogen	1.49		H=W	2049
	Chlorine			H=1/2W	2213
	Sulfur	3.26		Fluid	2256
	Ash	8.06	Oxid. Fusion Temp.	I.D.	2309
	Oxygen (Diff.)	8.69		H=W	2451
				H=1/2W	2528
				Fluid	2584
				Browning T250	2380
				B&W T250	2421

Appendix B. Uncertainty Analysis

Table B-1. Components of Uncertainty

symbol	description	units
u_k	effective thermal conductivity	W/m·K
u_t	deposit thickness	m
$u_{\Delta T}$	temp. difference across ash deposit	C
$u_{\dot{m}}$	mass flow rate	kg/s
u_{C_P}	specific heat of air	kJ/kg·K
$u_{\Delta T_m}$	mixed mean temp. difference across probe test section	C
u_A	internal cross-sectional area of probe	m^2
u_{probe}	probe position with respect to the profilometer	m
u_{unif}	uniformity of the ash deposit across the probe test section	m
u_{T_p}	surface temperature of the deposit probe	C
u_ρ	density of air	kg/m^3
u_C	pressure correction coefficient	---
$u_{T_{pro}}$	cooling-air temperature profile	---
u_u	cooling-air velocity profile	---
u_r	radius of the probe	m
u_{Pact}	actual atmospheric pressure	kPa
u_{Pcal}	calibration atmospheric pressure	kPa
u_T	thermocouple measurement	C
u_{SLM}	cooling-air volume flow rate	standard liters/min
u_{prof}	profilometer instrument	m
u_{T_s}	surface temperature of the ash deposit (from FTIR)	C

Uncertainty in the overall effective thermal conductivity is expressed by

$$u_k = \sqrt{\left(\frac{\partial k}{\partial q''} u_{q''}\right)^2 + \left(\frac{\partial k}{\partial t} u_t\right)^2 + \left(\frac{\partial k}{\partial \Delta T} u_{\Delta T}\right)^2} = \frac{u_k}{k}\sqrt{\left(\frac{u_{q''}}{q''}\right)^2 + \left(\frac{u_t}{t}\right)^2 + \left(\frac{u_{\Delta T}}{\Delta T}\right)^2} \quad \textbf{(B-1)}$$

The primary components of u_k are uncertainty in the heat flux, $u_{q''}$

$$\frac{u_{q''}}{q''} = \sqrt{\left(\frac{u_{\dot{m}}}{\dot{m}}\right)^2 + \left(\frac{u_{C_P}}{C_p}\right)^2 + \left(\frac{u_{\Delta T_m}}{\Delta T_m}\right)^2 + \left(\frac{u_A}{A}\right)^2} \quad \textbf{(B-2)}$$

uncertainty in the deposit thickness, u_t,

$$\frac{u_t}{t} = \sqrt{\left(\frac{u_{prof}}{t}\right)^2 + \left(\frac{u_{probe}}{t}\right)^2 + \left(\frac{u_{unif}}{t}\right)^2} \quad \textbf{(B-3)}$$

and uncertainty in the temperature difference across the ash deposit, $u_{\Delta T}$

$$\frac{u_{\Delta T}}{\Delta T} = \sqrt{\left(\frac{u_{T_p}}{\Delta T}\right)^2 + \left(\frac{u_{T_s}}{\Delta T}\right)^2} \quad \textbf{(B-4)}$$

These primary components (Eqs. (B-2) through (B-4)) are further composed of the following compound uncertainties:

the uncertainty in $u_{\dot{m}}$

$$\frac{u_{\dot{m}}}{\dot{m}} = \sqrt{\left(\frac{u_{\rho}}{\rho}\right)^2 + \left(\frac{u_{SLM}}{SLM}\right)^2 + \left(\frac{u_C}{C}\right)^2} \qquad \textbf{(B-5)}$$

the uncertainty in the mixed mean temperature difference (through the deposit probe test section), $u_{\Delta T_m}$

$$\frac{u_{\Delta T_m}}{\Delta T_m} = \sqrt{\left(\frac{u_{T_{Pro}}}{\Delta T_m}\right)^2 + \left(\frac{u_u}{u}\right)^2 + \left(\frac{u_r}{r}\right)^2} \qquad \textbf{(B-6)}$$

and the uncertainty in the internal cross-sectional area of the probe, u_A

$$\frac{u_A}{A} = \sqrt{\left(\frac{2u_r}{r}\right)^2} \qquad \textbf{(B-7)}$$

Additional compound uncertainty in the mass flow, $u_{\dot{m}}$, is the uncertainty of the pressure correction coefficient, u_C, defined by

$$\frac{u_C}{C} = \sqrt{\left(\frac{u_{P_{cal}}}{P_{cal}}\right)^2 + \left(\frac{u_{P_{act}}}{P_{act}}\right)^2} \qquad \textbf{(B-8)}$$

Additional compound uncertainty in the velocity measurement inside the probe, u_u, is the uncertainty in the average velocity, $u_{\bar{u}}$ given by Eq. (B-9).

$$\frac{u_{\bar{u}}}{\bar{u}} = \sqrt{\left(\frac{u_{\dot{m}}}{\dot{m}}\right)^2 + \left(\frac{u_\rho}{\rho}\right)^2 + \left(\frac{u_A}{A}\right)^2} \qquad \textbf{(B-9)}$$

Appendix C. Thermal Transport UDF Supplemental Information

Appendix C1 - Execution and Integration of the Thermal Transport UDF and FLUENT

The thermal transport UDF was designed to iterate once for every iteration performed by FLUENT. It was also designed to operate with FLUENT's steady-state solver. Convergence criteria were set, tested, and tracked within the UDF. Because the UDF has its own built-in convergence criteria and the UDF continually updates the deposit surface temperature, (which is passed directly to FLUENT as a boundary condition) convergence monitors should be disabled in FLUENT. The UDF will echo back information to inform the operator of its progress. Technically, the UDF is executed all the way through each time it is called. However, by storing values using FLUENT's "user-defined memory," the UDF keeps track (from iteration to iteration) of which sections have been completed, and only certain portions are actually executed as needed. When the UDF has fully completed, a message is displayed on the GUI, and FLUENT must then be manually stopped.

The Thermal Transport UDF is employed by first opening FLUENT and importing the meshed domain of interest. Next FUENT should be set to use its steady-state solver with the automatic residual monitors turned off. Continue by selecting the desired domain and fluid conditions. Set the appropriate boundary conditions and also

temporarily set the boundary condition temperature to a fixed value (at the boundary on which the UDF is to operate). The temperature where the UDF is to operate must be initially specified or the UDF will not run properly with FLUENT. The scenario should then be run, allowing FLUENT to iterate at least once. Now, variables required by the Thermal Transport UDF must be read into FLUENT from a text file. This is done by executing a separate UDF named "hard_ inputs." This UDF is executed only once by using the "execute on demand" option in FLUTENT and selecting the "read_hard_inputs" file. Input values and a message indicating successful reading of the input file will be echoed to the GUI terminal. The Thermal Transport UDF can now be hooked to FLUENT by changing the boundary condition of interest from a fixed temperature to a temperature controlled by the UDF, using the dropdown menu and choosing the name of the UDF, "calc_surf_temp." Immediately the UDF will be called and executed one time. The UDF is now hooked, and it will proceed to iterate once for each of FLUENT's iterations. The residuals and the GUI terminal may be monitored for progress and completion of the UDF. Two output files will be created: one contains recorded data from each converged time step (deposit layer) and the second is created only after successful convergence of the entire UDF and contains data of the completed ash deposit.

Appendix C2 - Detailed Flow Chart of the Thermal Transport UDF

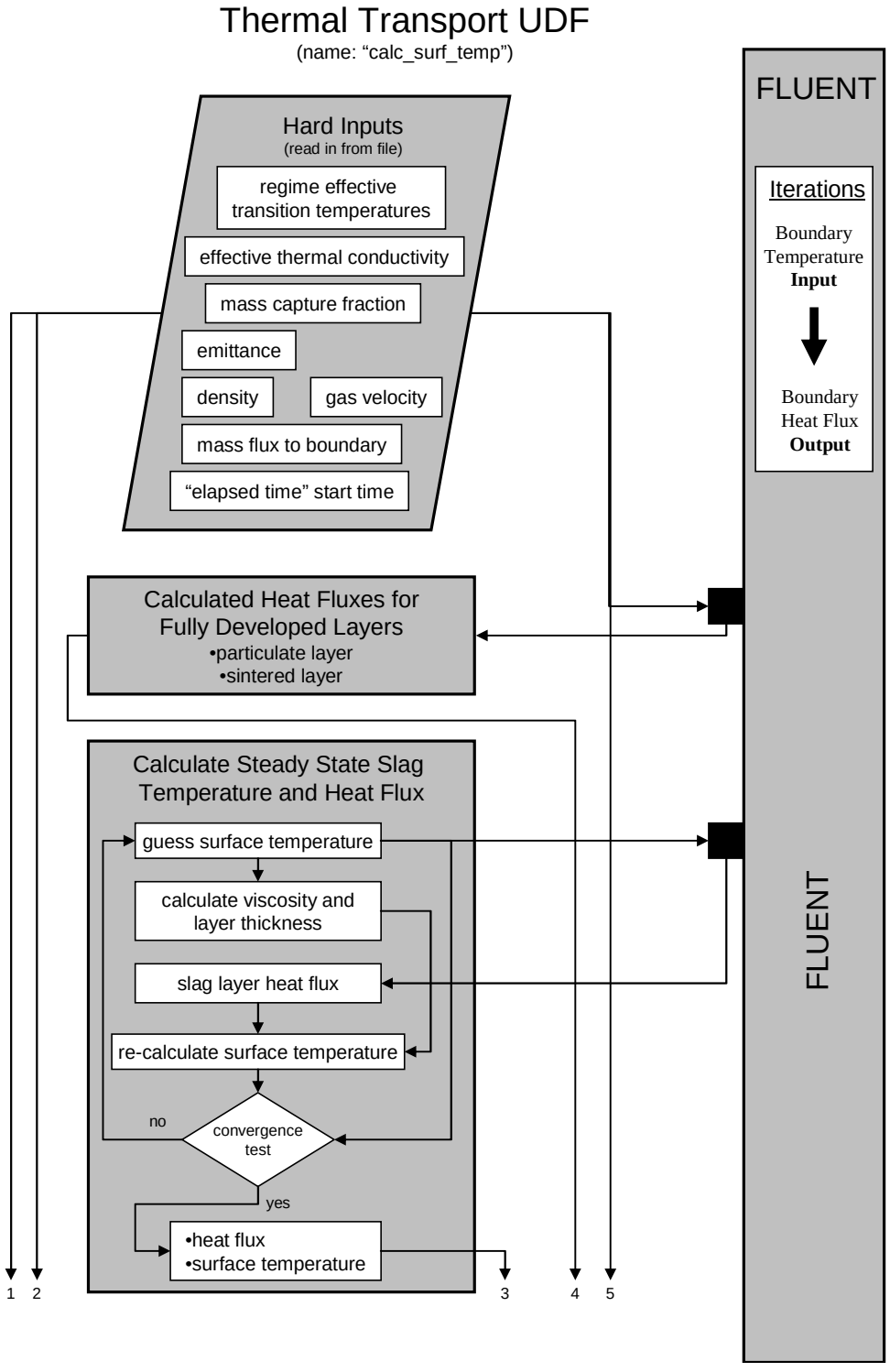

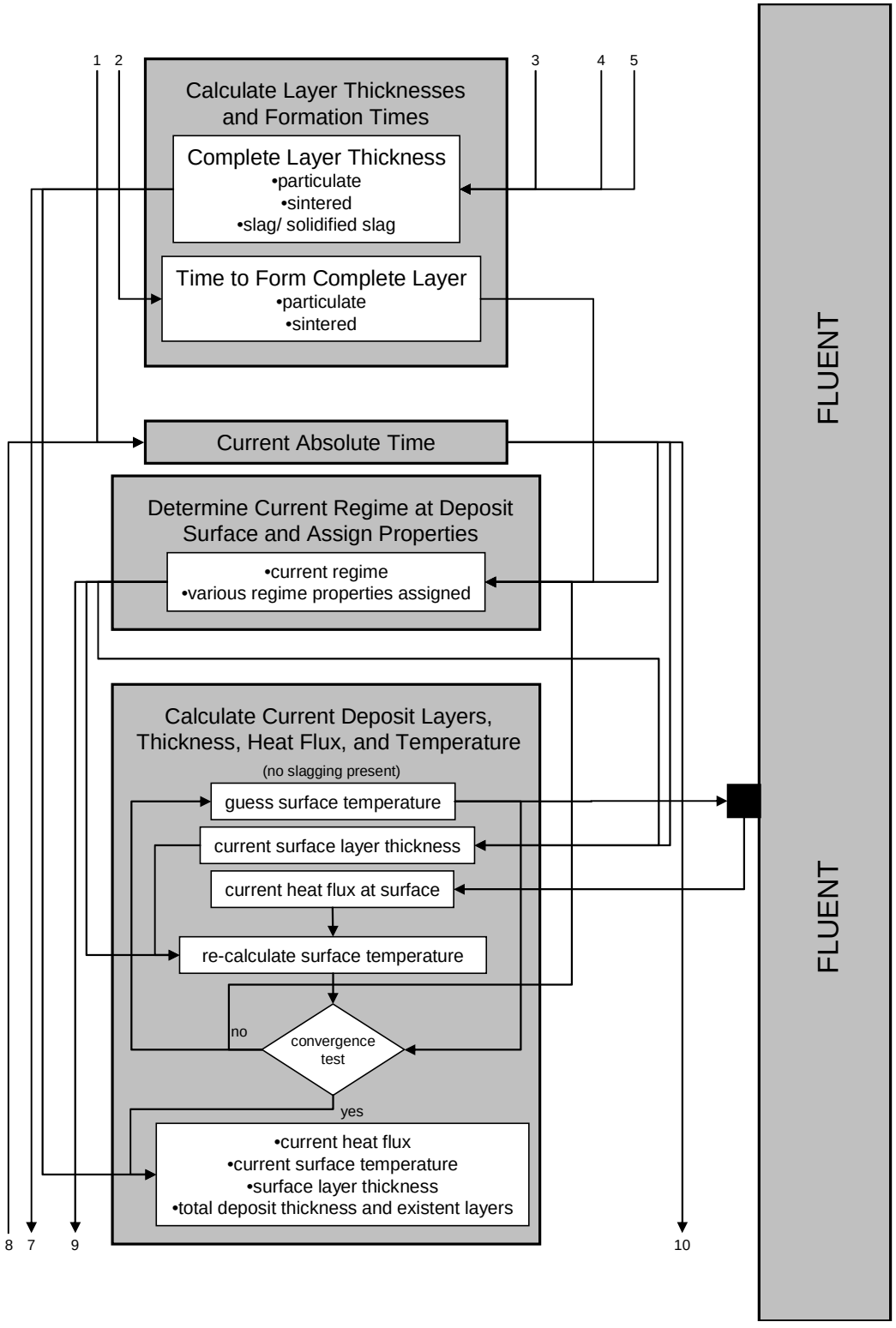
1
2
3
4
5
Calculate Layer Thicknesses and Formation Times
Complete Layer Thickness
•particulate
•sintered
•slag/ solidified slag
Time to Form Complete Layer
•particulate
•sintered
Current Absolute Time
Determine Current Regime at Deposit Surface and Assign Properties
•current regime
•various regime properties assigned
Calculate Current Deposit Layers, Thickness, Heat Flux, and Temperature
(no slagging present)
guess surface temperature
current surface layer thickness
current heat flux at surface
re-calculate surface temperature
no
convergence test
yes
•current heat flux
•current surface temperature
•surface layer thickness
•total deposit thickness and existent layers
FLUENT
FLUENT
8
7
9
10

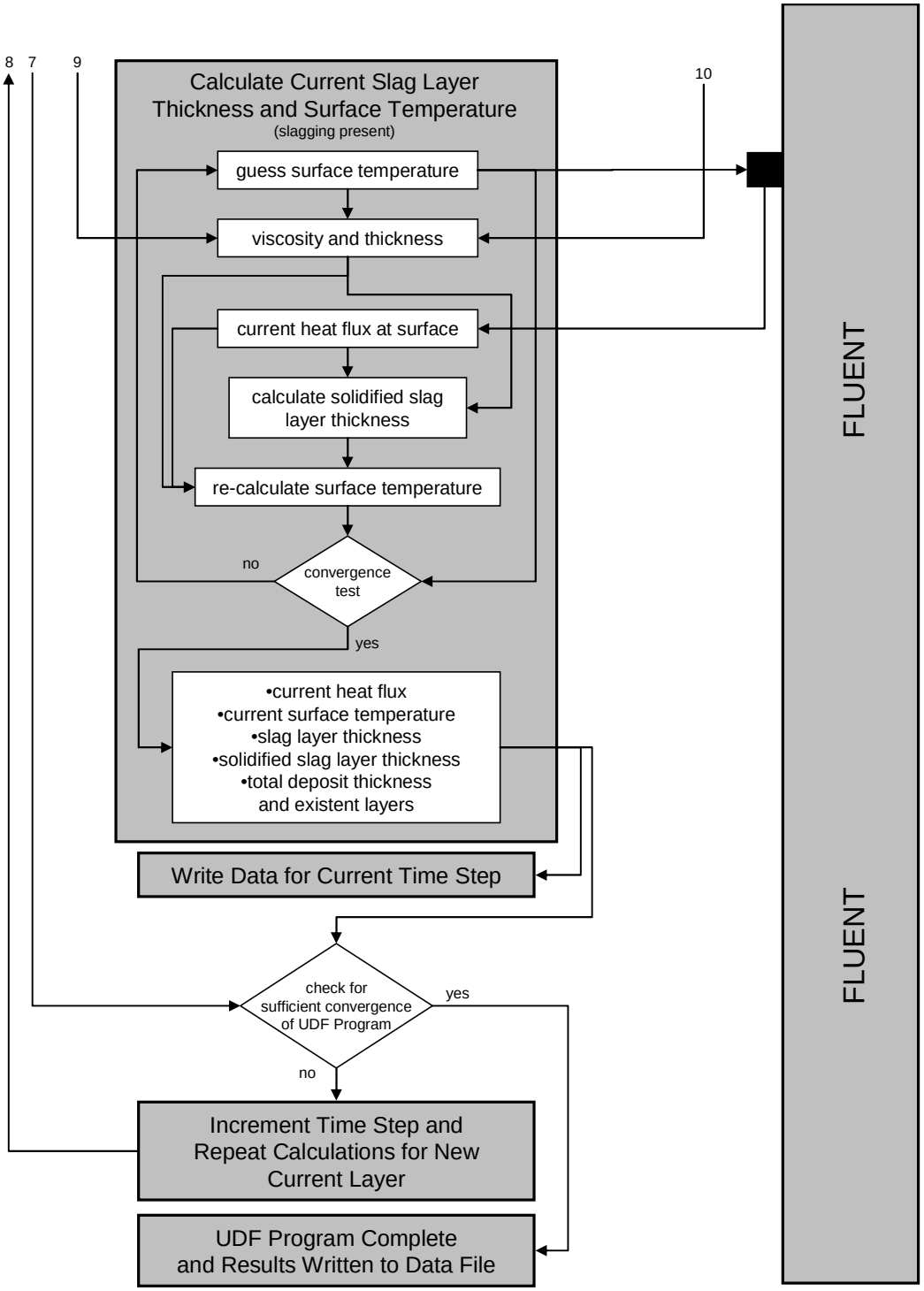
8
7
9
10
Calculate Current Slag Layer Thickness and Surface Temperature
(slagging present)
guess surface temperature
viscosity and thickness
current heat flux at surface
calculate solidified slag layer thickness
re-calculate surface temperature
no
convergence test
yes
•current heat flux
•current surface temperature
•slag layer thickness
•solidified slag layer thickness
•total deposit thickness
and existent layers
Write Data for Current Time Step
check for sufficient convergence of UDF Program
yes
no
Increment Time Step and Repeat Calculations for New Current Layer
UDF Program Complete and Results Written to Data File
FLUENT
FLUENT

Appendix C3 – Thermal Transport UDF Source Code

```
/*  Thermal Transport User Defined Function (TTUDF) for a coal ash
      deposit.
    Darron Cundick
    Dr. Daniel Maynes
    July 26, 2006
    Brigham Young University
    This UDF is written for FLUENT 6.2.16 and calculates the deposit
     surface temperature
    using the net heat flux as calculated by FLUENT, at a given time,
     for points
    along a vertical boundary.  The program updates the surface
     temperature and iterates
    in parallel with FLUENT until converged.
    It also models a fully developed ash layer with slagging, given the
     set of input
    conditions (read in from a file).
    **NOTE: this UDF converges in parallel with FLUENT and thus the
     operator must ensure
     that FLUENT has iterated a sufficient number of times to fully run
     and complete
     the UDF program. "SURFACE TEMPERATURE UDF PROGRAM ITERATION IS
     COMPLETE" will
     be printed to the FLUENT user console when the UDF has completed
     developing an
     ash deposit with steady-state slaging.

    Last Modified: Jan, 2007
*/

#include "udf.h"
#include "math.h"

/* declare program variables    */
   int regime, num_face, faces_total, case1, case2, case3, count,
   flux_count3, flux_count1, flux_count2;
   int count_Tsur1, num_faces, count_regime2, count_regime3,
   count_regime3a, faceID, faceIDa;
   int count_finish, delta_time;
   real centroid_array[ND_ND];
   real temp_one, temp_sint, temp_slag, temp_inf, k_particulate,
   k_frozen, roe_frozen;
   real k_sint, k_slag, mass_flux, y_particulate, y_sint, y_slag,
   roe_particulate;
   real roe_sint, roe_slag, sigma, convection_vel, size, size_prime,
   face_size, x_face_size;
   real y_face_size, xy_face_size, x_vector, y_vector;
   real thick_particulate_t, thick_sint_t, thick_slag_t,
   thick_slag_initial_t;
   real thick_total_t, temp_sint_new_t, temp_slag_new_t,
   temp_four_initial_t;
   real temp_four_modify_t, temp_four_left_t, temp_four_right_t,
   temp_four_t;
   real time_particulate_t, time_sint_t, time_slag_t, time_total_t,
   q_sint_t, q_slag_t;
```

```
   real k_gas, roe_gas, mu_gas, prandtl_num, time_sint_only_t;
   real reynolds_num, nusselt_num, convection_coef, store_one,
   store_two;
   real thick_particulate, thick_sint, thick_slag, thick_total;
   real temp_surface_initial, temp_surface_modify, temp_surface_left,
   temp_surface_right;
   real temp_surface, q_actual, var_one, var_two, var_three,
   mu_slag_avg, x_size, y_size, xy_size;
   real x_direction, y_direction, num_1, num_2;
   real num_1x, num_1y, num_2x, num_2y, x_total, y_total, xy_total,
   temp_sint_calc, q_use, T_gradient, ke, a, b;
   real mu_slag1, mu_slag2, emissivity_particulate, emissivity_sint,
   emissivity_slag;
   real check, fluxfluent1, fluxfluent2, thick_sint_only_t,
   temp_four_mu;
   real flux_sint, flux_sint_new, flux_slag, flux_slag_new, flux_T4,
   Tsur_avg;
   real temp_top, temp_bottom, increment, fluxfun, mu_one, mu_two,
   thick_slag_prime;
   real thick_slag_other, thick_frozen_added, thick_frozen_current,
   thick_frozen_total;
   real previous_time, mass_current, check_converge, power, parameter,
   flux_normalized;
   real Tsur=1200;
   int count_all=0, count_initialize=0, current_abs_time=10, count_part
   = 0;

/* read in hard inputs from file
*****************************************/
DEFINE_ON_DEMAND(read_hard_inputs)
{
    FILE *fp1;
    fp1=fopen("hardinputs-qinA.dat", "r");

    /* read inputs from file  */
    fscanf(fp1,"%g %g %g",&temp_one, &temp_sint, &temp_slag);
    fscanf(fp1,"%g %g %g %g %g",&temp_inf, &k_particulate, &k_sint,
     &k_frozen, &k_slag);
    fscanf(fp1,"%g %g %g %g",&mass_flux, &y_particulate, &y_sint,
     &y_slag);
    fscanf(fp1,"%g %g %g %g %g",&roe_particulate, &roe_sint,
     &roe_frozen, &roe_slag, &sigma);
    fscanf(fp1,"%g %g %g %g",&emissivity_particulate, &emissivity_sint,
     &emissivity_slag, &convection_vel);

    /* echo back values to FLUENT's console for feedback    */
      Message("\nHard inputs read from \"hardinputs-ginA.dat\"");
      Message("\n*Note: current_abs_time has been initialized to 10 sec.
       and will increment with iterations");
      Message("\ntemp_one = %g", temp_one);
      Message("\ntemp_sint = %g", temp_sint);
      Message("\ntemp_slag = %g", temp_slag);
       Message("\ntemp_inf = %g", temp_inf);
       Message("\nk_particulate = %g", k_particulate);
       Message("\nk_sint = %g", k_sint);
       Message("\nk_frozen = %g", k_frozen);
       Message("\nk_slag = %g", k_slag);
```

```
      Message("\nmass_flux = %g", mass_flux);
      Message("\ny_particulate = %g", y_particulate);
      Message("\ny_sint = %g", y_sint);
      Message("\ny_slag = %g", y_slag);
      Message("\nroe_particulate = %g", roe_particulate);
      Message("\nroe_sint = %g", roe_sint);
      Message("\nroe_frozen = %g", roe_frozen);
      Message("\nroe_slag = %g", roe_slag);
      Message("\nsigma = %g", sigma);
      Message("\nemissivity_particulate = %g", emissivity_particulate);
      Message("\nemissivity_sint = %g", emissivity_sint);
      Message("\nemissivity_slag = %g", emissivity_slag);
      Message("\nconvection gas velocity is %g", convection_vel);

     fclose(fp1);
}

/* calculate surface temperature and other outputs.  This UDF is to be
   "hooked" to temperature
   in the boundary conditions for the ash boundary
   *********************************/
   DEFINE_PROFILE(calc_surf_temp,t,i)
   {
       face_t f;  /* declare face identifier for FLUENT.
                     **Note this must be first thing declared! */
       FILE *fp2;  /* pointers should be declared next or FLUENT's
       compiler may give errors */
       FILE *fp3;
       x_size = 0.0;
       y_size = 0.0;
       xy_size = 0.0;
       x_direction = 0.0;
       y_direction = 0.0;
       x_vector = 0.0;
       y_vector = 0.0;
       num_face = 0;
       num_1x = 0.0;
       num_1y = 0.0;
       a = 0.000000000208112;
       b = 30.886901;

       mu_two = b*1000/temp_slag;
            mu_slag1 = a*temp_slag*exp(mu_two);

      /* initialize user defined memory variables, first time (only)
         through the UDF .
         These values are for initialization only and will not be used
         in calculations */
         if(count_initialize == 0)
         {
            Message("\nnow initializing UDM variables . . .");
            begin_f_loop(f,t)
            {
                  F_UDMI(f,t,0) = 90;     /* flux through developed
                  particulate layer */
                  F_UDMI(f,t,1) = 90;     /* flux through developed
                  sintered layer */
```

```
                F_UDMI(f,t,2) = 1591;   /* T4 of fully developed ash
                deposit */
                F_UDMI(f,t,3) = 0.001;  /* thickness of slag layer in
                fully developed deposit */
                F_UDMI(f,t,4) = 90;     /* flux through fully
                developed deposit */
                F_UDMI(f,t,5) = 1101;   /* surface temperature for
                given current time */
                F_UDMI(f,t,6) = 1000;   /* flux of entire ash layer
                formed at given current time */
                F_UDMI(f,t,7) = 1;      /* relative position along
                the boundary face, as measured from one end */
                F_UDMI(f,t,8) = 1;      /* absolute position, "y" of
                face (FLUENT's coordinates) */
                F_UDMI(f,t,9) = 0.001;  /* thickness of particualate
                layer at given current time */
                F_UDMI(f,t,10) = 0.001; /* thickness of sintered
                layer at given current time */
                F_UDMI(f,t,11) = 0.0;   /* thickness of slag layer at
                given current time */
                F_UDMI(f,t,12) = 0.005; /* thickness of entire ash
                deposit at given current time */
                F_UDMI(f,t,13) = 0.001; /* thickness of particulate
                layer in fully developed deposit model*/
                F_UDMI(f,t,14) = 0.001; /* thickness of sintered
                layer in fully developed deposit model*/
                F_UDMI(f,t,15) = 0.001; /* thicknes of fully
                developed sintered layer, before transition to
                slagging */
                F_UDMI(f,t,16) = 0.005; /* total thickness of fully
                developed deposit model*/
                F_UDMI(f,t,17) = 200;   /* particulate layer
                formation time of fully developed model */
                F_UDMI(f,t,18) = 5000;  /* sintered layer formation
                time of fully developed model */
                F_UDMI(f,t,19) = 10000; /* entire deposit formation
                time of fully developed model */
                F_UDMI(f,t,20) = 0;         /* current regime for the
                face on the boundary */
                F_UDMI(f,t,21) = 0;     /* total mass composed of
                frozen slag and slag layers at given current time */
                F_UDMI(f,t,22) = 0;         /* thickness of frozen
                slag layer at given current time  */
                F_UDMI(f,t,23) = 0;     /* iteration counter for each
                layer */
                F_UDMI(f,t,24) = 1;     /* absolute position, "x" of
                face (FLUENT's coordinates)   */
        }
        end_f_loop(f,t)
        count_initialize = 1;
        Message("\nCheck: UDM variables initialized.");

}

Message("\nCheck: current time is %i", current_abs_time);
/* determine number of faces and physical domain size of ash
boundary (loop over all faces)      */
```

```
begin_f_loop(f,t)
{
      fluxfun = BOUNDARY_HEAT_FLUX(f,t);
      Message("\nflux = %g", fluxfun);          /* echo back
      current flux value, calculated by FLUENT  */
      num_face = num_face + 1;            /* counter for faces
      along boundary    */
      num_2x = centroid_array[0];   /* holds previous
      centroid_array[0] value */
      num_2y = centroid_array[1];   /* holds previous
      centroid_array[1] value */

      /* centroid_array[0,1,2] (x, y, and z absolute coordinates)
      gets assigned here      */
      F_CENTROID(centroid_array,f,t);

      if(num_face == 1)
      {
            num_1x = centroid_array[0];   /* allows x_size to
      begin at zero */
            num_1y = centroid_array[1];   /* allows y_size to
      begin at zero */
            num_2x = centroid_array[0];
            num_2y = centroid_array[1];
      }
      x_size = x_size + fabs(num_1x - centroid_array[0]);   /*
      x_size stores the domain size in x direction */
      y_size = y_size + fabs(num_1y - centroid_array[1]);   /*
      y_size stores the domain size in y direction */
      xy_size = xy_size + sqrt(pow((num_1x -
      centroid_array[0]),2) + pow((num_1y -
      centroid_array[1]),2));
      num_1x = centroid_array[0];
      num_1y = centroid_array[1];
      x_direction = x_direction + (centroid_array[0] - num_2x);
      /* Message("\nCheck: x_direction value is %g",
      x_direction);     */
      y_direction = y_direction + (centroid_array[1] - num_2y);
      x_vector = x_vector + F_U(f,t);
      y_vector = y_vector + F_V(f,t);
}
end_f_loop(f,t)

x_total = x_size;
y_total = y_size;
xy_total = xy_size;
x_face_size = fabs(num_1x - centroid_array[0]);
y_face_size = fabs(num_1y - centroid_array[1]);
xy_face_size = sqrt(pow((num_1x - centroid_array[0]),2) +
pow((num_1y - centroid_array[1]),2));
faces_total = num_face; /* total number of faces along boundary
*/

/* determine FLUENT calculation sequence and boundary domain
orientation.
This is used for calculating length_x and length_y    */
if(x_direction != 0)
```

```
{
      case3 = 1;
            Message("\nBoundary orientation is horizontal,
            x_direction value is %g", x_direction);
            if(x_direction > 0)
            {
                  case1 = 1;              /* face calculations in
                  positive x order  */
                  Message("\nFluent calculations (within surface
                  temp UDF) are in positive \"x\" order.");
            }
            else
            {
                  case1 = 2;              /* face calculations in
                  negative x order  */
                  Message("\nFluent calculations (within surface
                  temp UDF) are in negative \"x\" order.");
            }
      }
      if(y_direction != 0)
      {
            case3 = 2;
            Message("\nBoundary orientation is vertical,
            y_direction value is %g", y_direction);
            if(y_direction > 0)
            {
                  case2 = 1;              /* face calculations in
                  positive y order  */
                  Message("\nFluent calculations (within surface
                  temp UDF) are in positive \"y\" order.");
            }
            else
            {
                  case2 = 2;              /* face calculations in
                  negative y order  */
                  Message("\nFluent calculations (within surface
                  temp UDF) are in negative \"y\" order.");
            }
      }
      if(x_direction != 0 && y_direction != 0)
      {
            case3 = 3;
            Message("\nBoundary orientation is in the xy plane");
      }
      if(x_direction == 0 && y_direction == 0)
      {
            Message("\nERROR: Boundary orientation was not
            determined!");
            Message("\nThis must be resolved before obtaining
            valid results.");
      }
      Message("\nCheck: boundary thread faces numbered and
      calculation-order case determined.");
      Message("\nnumber of faces = %i, case1 is %i, and case2 is
      %i", faces_total, case1, case2);
```

```
/* calculate heat flux at particulate/sintered transition
for  use in creating
full model thickness and formation time data        */
/* determine particulate layer heat fluxes      */
Message("\nCheck: first count_all value is %i", count_all);
if(count_all == 0)
{
      /* reset convergence counter each time the UDF runs
      and condition is satisfied.  */
      flux_count1 = 0;

      if(flux_count1 < faces_total)
      {
            Message("\ncalculating particulate layer flux.
            . .");
            begin_f_loop(f,t)
            {
                  F_PROFILE(f,t,i) = temp_sint;       /*
                  assign sint temperature to boundary */
                  Message("\nCheck: temp assigned is %g,
                  face temp read is %g", temp_sint,
                  F_T(f,t));

                  flux_sint = BOUNDARY_HEAT_FLUX(f,t);  /*
                  extract heat flux calculated by FLUENT*/
                  if(flux_sint < 0)
                        flux_sint = flux_sint*(-1);
                        /* keep heat flux positive for
                        calculations */
                  if(fabs(flux_sint - F_UDMI(f,t,0)) < 1)
                        /* check for sufficient convergence
                        */
                        flux_count1 = flux_count1 + 1;
                        /* increment counter to track
                        convergence checks */
                  Message("\nCheck: flux sint = %g, and UDM
                  0 = %g temp = %g", flux_sint,
                  F_UDMI(f,t,0), F_T(f,t));
                  F_UDMI(f,t,0) = flux_sint;          /*
                  store flux value for each face      */
            }
            end_f_loop(f,t)
            Message("\nflux_count1 is %i", flux_count1);
            count_part = count_part + 1;
      }

      /* check for flux convergence (by FLUENT) for each
      face  and then increment overall
      counter when the condition is met, i.e. all faces'
      flux convereged   */
      if(flux_count1 >= faces_total)
      {
            if(count_part > 2)
            {
                  count_all = count_all + 1;
                  Message("\nCheck: particulate layer flux
                  converged.");
```

```
            }
      }
}

/* determine sintered layer heat fluxes   */
if(count_all == 1)
{
      flux_count2 = 0;
      if(flux_count2 < faces_total)
      {
            Message("\ncalculating sintered layer flux. .
            .");
            begin_f_loop(f,t)
            {
                  F_PROFILE(f,t,i) = temp_slag;
                  Message("\nCheck: temp read is %g",
                  F_T(f,t));
                  flux_slag = BOUNDARY_HEAT_FLUX(f,t);
                  if(flux_slag < 0)
                        flux_slag = flux_slag*(-1);
                  if(fabs(flux_slag - F_UDMI(f,t,1)) < 1)
                        flux_count2 = flux_count2 + 1;
                  F_UDMI(f,t,1) = flux_slag;
            }
            end_f_loop(f,t)
            Message("\nflux_count2 is %i", flux_count2);
      }
      if(flux_count2 >= faces_total)
      {
            count_all = count_all + 1;
            Message("\nCheck: sintered layer flux
            converged.");
      }
}

/* determine slag surface temperatures and heat fluxes
*/
if(count_all == 2)
{
      flux_count3 = 0;
      if(flux_count3 < faces_total)
      {
            Message("\ncalculating slag layer flux. . .");
            num_face = 0;
            x_size = 0;
            y_size = 0;
            begin_f_loop(f,t)
            {
                  /* determine position within domain */
                  num_face = num_face + 1;
                  F_CENTROID(centroid_array,f,t);
                  /* centroid_array[] gets assigned here
                  */
                  if(num_face == 1)
                  {
                        num_1x = centroid_array[0];
                        num_1y = centroid_array[1];
```

```
}
x_size = x_size + fabs(num_1x -
centroid_array[0]);
y_size = y_size + fabs(num_1y -
centroid_array[1]);
xy_size = xy_size + sqrt(pow((num_1x -
centroid_array[0]),2) + pow((num_1y -
centroid_array[1]),2));
num_1x = centroid_array[0];
num_1y = centroid_array[1];
if(case3 == 1)
{
      if(case1 == 1)
            size = x_size;
      else
            size = x_total - x_size;
}
if(case3 == 2)
{
      if(case2 == 1)
            size = y_size;
      else
            size = y_total - y_size;
}
if(case3 == 3)
{
      if(x_vector > y_vector)
      {
            if(case1 == 1)
                  size = xy_size;
            else
                  size = xy_total -
                  xy_size;
      }
      else
      {
            if(case2 == 1)
                  size = xy_size;
            else
                  size = xy_total -
                  xy_size;
      }
}
if(size == 0)
      size = 0.1;


/* calculate steady state slag thickness
and resulting temperature and heat flux
*/
flux_T4 = BOUNDARY_HEAT_FLUX(f,t);
Message("\nCheck: flux_T4 value is %g",
flux_T4);
if(flux_T4 < 0)
      flux_T4 = flux_T4*(-1);
if(fabs(flux_T4 - F_UDMI(f,t,4)) < 1)
{
```

```
                        temp_four_mu =
                        F_UDMI(f,t,3)*flux_T4/k_slag +
                        temp_slag;
                        if(fabs(F_UDMI(f,t,2) -
                        temp_four_mu) < 2)
                              flux_count3 = flux_count3 +
                              1;
                        else
                        {
                              if(temp_four_mu <
                              F_UDMI(f,t,2))
                              {
                                    temp_four_mu =
                                    F_UDMI(f,t,2) -
                                    fabs(temp_four_mu -
                                    F_UDMI(f,t,2))*0.3;
                              }
                              else
                              {
                                    temp_four_mu =
                                    F_UDMI(f,t,2) +
                                    fabs(temp_four_mu -
                                    F_UDMI(f,t,2))*0.3;
                              }
                              mu_one = b*1000/temp_four_mu;
                              mu_slag2 =
                              a*temp_four_mu*exp(mu_one);
                              mu_slag_avg = (mu_slag1 +
                              mu_slag2)/2;
                              var_one =
                              mu_slag_avg*y_slag*mass_flux*
                              size*3.0;
                              var_two =
                              pow(roe_slag,2)*9.81;
                              var_three = var_one/var_two;
                              thick_slag_initial_t =
                              pow(var_three,0.33333);
                              F_UDMI(f,t,3) =
                              thick_slag_initial_t;
                              F_UDMI(f,t,2) = temp_four_mu;
                              F_PROFILE(f,t,i) =
                              temp_four_mu;
                              /* Message("\nCheck:
                              temp_four_mu value is %g",
                              temp_four_mu); */
                        }
                  }
                  F_UDMI(f,t,4) = flux_T4;
            }
            end_f_loop(f,t)
            Message("\nflux_count3 is %i", flux_count3);
      }
      if(flux_count3 >= faces_total)
      {
            count_all = count_all + 1;
            Message("\nCheck: slag layer flux converged.");
      }
```

```
}

if(count_all == 3)
{
      /* calculate layer thicknesses and formation times at
      each regime boundary face     */
      num_face = 0;
      x_size = 0;
      y_size = 0;
      count_Tsur1 = 0;
      count_regime2 = 0;
      count_regime3 = 0;
      size_prime = 0;
      count_finish = 0;
      fp3 = fopen("UDFparameters.txt","a");

      /*fprintf(fp3,"Convergence magnitude data");    */
      Message("\nCalculating current temperatures, fluxes,
      thicknesses, and times. . .");
      begin_f_loop(f,t)
      {
            Message("\ncalculations for height y = %g",
            F_UDMI(f,t,7));
            fluxfluent1 = BOUNDARY_HEAT_FLUX(f,t);

            /* these values get calculated for each face
            loop as they are face dependent    */
            thick_particulate_t = k_particulate*(temp_sint
            - temp_one)/F_UDMI(f,t,0); /* from flux_sint */
            F_UDMI(f,t,13) = thick_particulate_t;
            time_particulate_t =
            thick_particulate_t*roe_particulate/(y_particul
            ate*mass_flux);
            F_UDMI(f,t,17) = time_particulate_t;
            thick_sint_only_t = (k_sint*(temp_slag -
            temp_sint))/F_UDMI(f,t,1); /* from flux_slag */
            F_UDMI(f,t,15) = thick_sint_only_t;
            time_sint_only_t =
            thick_sint_only_t*roe_sint/(y_sint*mass_flux);
            F_UDMI(f,t,18) = time_sint_only_t;
            thick_sint_t = k_sint*(temp_slag -
            temp_sint)/F_UDMI(f,t,4);  /* from flux_T4 */
            F_UDMI(f,t,14) = thick_sint_t;
            thick_total_t = thick_particulate_t +
            thick_sint_t + F_UDMI(f,t,3);
            F_UDMI(f,t,16) = thick_total_t;
            time_total_t = time_particulate_t +
            time_sint_only_t; /* time to reach slagging
            condition */
            F_UDMI(f,t,19) = time_total_t;
            Message("\nCheck: time_total_t value is %g",
            time_total_t);

            /* determine regime (particulate =1, sintered
            =2, slagging =3)  */
            if(current_abs_time < time_particulate_t)
                  regime = 1;
```

```
else
{
      if(current_abs_time >= (time_total_t))
      {
            regime = 3;
            count_regime3 = count_regime3 + 1;
      }
      else
      {
            regime = 2;
      }
}
num_face = num_face + 1;
F_CENTROID(centroid_array,f,t);     /*
centroid_array[] gets assigned here */
if(num_face == 1)
{
      num_1x = centroid_array[0];
      num_1y = centroid_array[1];
}
x_size = x_size + fabs(num_1x -
centroid_array[0]);
y_size = y_size + fabs(num_1y -
centroid_array[1]);
xy_size = xy_size + sqrt(pow((num_1x -
centroid_array[0]),2) + pow((num_1y -
centroid_array[1]),2));
num_1x = centroid_array[0];
num_1y = centroid_array[1];
if(case3 == 1)
{
      if(case1 == 1)
            size = x_size;
      else
            size = x_total - x_size;
      face_size = x_face_size;
}
if(case3 == 2)
{
      if(case2 == 1)
            size = y_size;
      else
            size = y_total - y_size;
      face_size = y_face_size;
}
if(case3 == 3)
{
      if(x_vector > y_vector)
      {
            if(case1 == 1)
                  size = xy_size;
            else
                  size = xy_total - xy_size;
      }
      else
      {
            if(case2 == 1)
```

```
                  size = xy_size;
            else
                  size = xy_total - xy_size;
      }
      face_size = xy_face_size;

}
if(size == 0)
      size = 0.1;
F_UDMI(f,t,7) = size;
F_UDMI(f,t,8) = num_1y;
F_UDMI(f,t,24) = num_1x;

if(fluxfluent1 < 0)
      fluxfluent1 = fluxfluent1*(-1);
if(fabs(fluxfluent1 - F_UDMI(f,t,6)) < 1)
{
      /* set soft inputs: determine model
      regime and material properties    */
      /* assign convective gas properties by
      regime    */
      if(regime == 1)    /* particulate regime
      */
      {
            prandtl_num = 0.721;
            mu_gas = 0.0000404;
            k_gas = 0.063;
            roe_gas = 0.379;
            reynolds_num =
            convection_vel*size*roe_gas/mu_gas;
            nusselt_num =
            0.0308*pow(reynolds_num,
            0.8)*pow(prandtl_num, 0.33333);
            convection_coef =
            nusselt_num*k_gas/size;
      }
      if(regime == 2)        /* sintered regime
      */
      {
            count_regime2 = count_regime2 + 1;
            prandtl_num = 0.705;
            mu_gas = .0000531;
            k_gas = 0.0934;
            roe_gas = 0.2709;
            reynolds_num =
            convection_vel*size*roe_gas/mu_gas;
            nusselt_num =
            0.0308*pow(reynolds_num,
            0.8)*pow(prandtl_num, 0.33333);
            convection_coef =
            nusselt_num*k_gas/size;
      }
      if(regime == 3)    /* slagging regime
      */
      {
            /* determine x' position and size
            as applied to slagging portion of
```

```
      boundary layer */
      if(count_regime3 == 1)
            size_prime = 0.5*face_size;
      else
      {
            size_prime =
            count_regime3*face_size -
            0.5*face_size;
      }
      prandtl_num = 0.675;
      mu_gas = .0000676;
      k_gas = 0.134;
      roe_gas = 0.1796;
      reynolds_num =
      convection_vel*size_prime*roe_gas/m
      u_gas;
      nusselt_num =
      0.0308*pow(reynolds_num,
      0.8)*pow(prandtl_num, 0.33333);
      convection_coef =
      nusselt_num*k_gas/size_prime;
}
Message("\nRegime is %i", regime);
Message("\nface ID is %i", f);
F_UDMI(f,t,20) = regime;

/* calculate layer thicknesses and
formation times from input current time
*/
if(regime == 1)
{
      /* calculate thicknesses   */
      thick_particulate =
      current_abs_time*y_particulate*mass
      _flux/roe_particulate;
      F_UDMI(f,t,9) = thick_particulate;
      thick_sint = 0;
      F_UDMI(f,t,10) = thick_sint;
      thick_slag = 0;
      F_UDMI(f,t,11) = thick_slag;
      thick_total = thick_particulate;
      F_UDMI(f,t,12) = thick_total;

      /* calculate surface temperature
      using FLUENT's flux for comparison
      */
      Tsur =
      fluxfluent1*thick_particulate/k_par
      ticulate + temp_one;

      Tsur_avg = F_UDMI(f,t,5);
      /* test for sufficient convergence
      and record it using counter */
      if(fabs(Tsur - F_UDMI(f,t,5)) < 2)
            count_Tsur1 = count_Tsur1 +
            1;
      else
```

```
        {
              if(Tsur < Tsur_avg)
              {
                    Tsur_avg = Tsur_avg -
                    fabs(Tsur_avg -
                    Tsur)*0.3;
              }
              /* Tsur will otherwise be
              greater than Tsur_avg;
              increment Tsur_avg */
              else
              {
                    Tsur_avg = Tsur_avg +
                    fabs(Tsur_avg -
                    Tsur)*0.3;
              }
              F_UDMI(f,t,5) = Tsur_avg;
              F_PROFILE(f,t,i) = Tsur_avg;
              Message("\nCheck: Tsur_avg
              value is %g and has been
              updated within regime 1",
              Tsur_avg);
        }
  }
  if(regime == 2)
  {
        thick_particulate =
        thick_particulate_t;
        F_UDMI(f,t,9) = thick_particulate;
        thick_sint = (current_abs_time -
        time_particulate_t)*y_sint*mass_flu
        x/roe_sint;
        F_UDMI(f,t,10) = thick_sint;
        thick_slag = 0;
        F_UDMI(f,t,11) = thick_slag;
        thick_total = thick_particulate +
        thick_sint;
        F_UDMI(f,t,12) = thick_total;

        /* calculate surface temperature
        using FLUENT's flux for comparison
        */
        Tsur =
        fluxfluent1*thick_sint/k_sint +
        temp_sint;
        Tsur_avg = F_UDMI(f,t,5);
        if(fabs(Tsur - F_UDMI(f,t,5)) < 2)
              count_Tsur1 = count_Tsur1 +
              1;
        else
        {
              if(Tsur < Tsur_avg)
              {
                    Tsur_avg = Tsur_avg -
                    fabs(Tsur_avg -
                    Tsur)*0.3;
              }
```

```
                /* Tsur will otherwise be
                greater than Tsur_avg;
                increment Tsur_avg */
                else
                {
                      Tsur_avg = Tsur_avg +
                      fabs(Tsur_avg -
                      Tsur)*0.3;
                }
                F_UDMI(f,t,5) = Tsur_avg;
                F_PROFILE(f,t,i) = Tsur_avg;
                Message("\nCheck: Tsur_avg
                value is %g and has been
                updated within regime 2",
                Tsur_avg);
          }
    }
    if(regime == 3)
    {
          faceID = f;
          f = count_regime3-1;
          /* Message("\nCheck: face f changed
          to %i", f); */
          thick_slag_other = F_UDMI(f,t,3);
          Message("\nCheck: steady state slag
          thickness is %g",
          thick_slag_other);
          f = faceID;

          if (F_UDMI(f,t,11) <=
          thick_slag_other)
          {
                thick_particulate =
                thick_particulate_t;
                F_UDMI(f,t,9) =
                thick_particulate;
                thick_sint =
                thick_sint_only_t;
                F_UDMI(f,t,10) = thick_sint;
                delta_time = current_abs_time
                - previous_time;

                /* (mass = slag mass + frozen
                mass + added mass during time
                step)   */
                mass_current = F_UDMI(f,t,21)
                + mass_flux*delta_time;

                thick_frozen_total =
                k_frozen*((temp_slag -
                temp_sint)/fluxfluent1 -
                thick_sint/k_sint));
                /*
                if(thick_frozen_total < 0)
                {
                      thick_frozen_total = 0;
```

```
      Message("\nNOTE t
      frozen total value is
      negative! t frozen
      total value set to
      0.");

}*/

/* by mass balance  */
thick_slag = (mass_current -
thick_frozen_total*roe_frozen
)/roe_slag;
power = pow((1850 -
F_UDMI(f,t,5)),4);
/*

flux_normalized =
(fluxfluent1 -
130000)/120000;
check_converge =
(1/log(flux_normalized+.9))*.
000007;
*/
/*Message("\nCheck: power
value is %g", power);
/*
if(power < 1000000000)
{
      check_converge =
      0.00007;
}
else
{
      check_converge =
      0.000007;
}
*/
/*
if(thick_slag > 0.0045)
{
      check_converge =
      0.00007;
}
else
{
      check_converge =
      0.000007;
}
*/
check_converge = 0.000007;
if(fluxfluent1 < 125000)
{
      check_converge =
      0.0005;
}
```

```
/* Message("\nCheck:
convergence check value is
%g", check_converge); */
if(fabs(thick_slag
F_UDMI(f,t,11)) <
check_converge)
{
      /* store values for
      converged condition for
      current time step   */
      count_Tsur1 =
      count_Tsur1 + 1;
      F_UDMI(f,t,22) =
      thick_frozen_total;
      thick_total =
      thick_particulate +
      thick_sint +
      F_UDMI(f,t,22) +
      thick_slag;
      F_UDMI(f,t,12) =
      thick_total;
      /*Message("\nCheck:
      thick_frozen_total
      value stored is %g",
      thick_frozen_total); */
      F_UDMI(f,t,11) =
      thick_slag;
      Tsur =
      (fluxfluent1*F_UDMI(f,t
      ,11))/k_slag +
      temp_slag;
      F_UDMI(f,t,5) = Tsur;
      /*Message("\nCheck:
      thick_slag value stored
      is %g", thick_slag);
      Message("\nCheck:
      current converged Tsur
      value is %g",
      F_T(f,t)); */
}
else
{
      Tsur =
      (fluxfluent1*F_UDMI(f,t
      ,11))/k_slag +
      temp_slag;
      /*Message("\nCheck:
      Tsur first value is
      %g", Tsur); */
      F_UDMI(f,t,11) =
      thick_slag;
      Tsur =
      (fluxfluent1*F_UDMI(f,t
      ,11))/k_slag +
      temp_slag;
```

```
                        /*Message("\nCheck: Tsur
                        current value is %g", Tsur);
                        */

                              if(Tsur <
                              F_UDMI(f,t,5))
                                    Tsur =
                                    F_UDMI(f,t,5) -
                                    fabs(Tsur -
                                    F_UDMI(f,t,5))*0.
                                    43;
                              if(Tsur >
                              F_UDMI(f,t,5))
                                    Tsur =
                                    F_UDMI(f,t,5) +
                                    fabs(Tsur -
                                    F_UDMI(f,t,5))*0.
                                    43;
                              F_UDMI(f,t,5) = Tsur;
                              F_PROFILE(f,t,i) =
                              Tsur;
                              /*Message("\nCheck:
                              thick_slag value
                              updated and Tsur; Tsur
                              new value is %g",
                              Tsur); */
                              F_UDMI(f,t,23) =
                              F_UDMI(f,t,23) + 1;
                        }
                  }
                  else
                  {
                        count_Tsur1 = count_Tsur1 +
                        1;
                        count_finish = count_finish
                        + 1;
                        Message("\nCurrent steady
                        state slag thickness reached
                        and count_Tsur1
                        incremented");
                  }
            }
      }
      F_UDMI(f,t,6) = fluxfluent1;    /* store flux
      value into memory */
}
end_f_loop(f,t)
/* Message("\nCheck: count_Tsur1 value is %i",
count_Tsur1); */
if(count_Tsur1 >= faces_total)
{
      Message("\nCheck: converged current surface
      temperatures have been calculated from input
      time.");
      Message("\nUpdating the frozen layer
      thicknesses. . .");
      count_regime3a = 0;
```

```
            begin_f_loop(f,t)
            {
                  if(F_UDMI(f,t,20) == 3)
                  {
                        if (F_UDMI(f,t,11) <=
                        thick_slag_other)
                        {
                              F_UDMI(f,t,21) =
                              F_UDMI(f,t,21) +
                              mass_flux*delta_time;
                              Message("\nCheck:
                              mass_current value stored
                              into memory is %g",
                              F_UDMI(f,t,21));
                        }
                        parameter = F_UDMI(f,t,21) -
                        pow(F_UDMI(f,t,6),3)*pow(F_UDMI(f,t
                        ,11),4) + F_UDMI(f,t,10);
                        fprintf(fp3,"\n%g, %i, %g, %g, %g,
                        %g", F_UDMI(f,t,7),
                        current_abs_time, parameter,
                        F_UDMI(f,t,23), F_UDMI(f,t,6),
                        F_UDMI(f,t,5));
                  }
                  else
                  {
                        /* mass of frozen slag and slag
                        layers will otherwise be zero (for
                        regime != 3)   */
                        F_UDMI(f,t,21) = 0;
                  }
            }
            end_f_loop(f,t)
            count_all = count_all + 1;
      }
fclose(fp3);
}

if(count_all == 4)
{
      /* write data for current time step */
      fp2 = fopen("ashUDFresults-time.txt","a");
      fprintf(fp2,"\n\nThe ash layer model results for
      current time = %i (sec)\n", current_abs_time);
      fprintf(fp2,"\nmodel y , regime , Tsur , ");
      fprintf(fp2,"flux , t part , t sint , ");
      fprintf(fp2,"t slag , t frozen current , t total ,
      Tsur from FLUENT");

      Message("\nCurrent time condition cacluations have
      been completed. Data written to \"ashUDFresults-
      time.txt\"");
      begin_f_loop(f,t)
      {
            fprintf(fp2,"\n%g , %g , %g , ", F_UDMI(f,t,7),
            F_UDMI(f,t,20), F_UDMI(f,t,5));
```

```
                fprintf(fp2,"%g , %g , %g , ", F_UDMI(f,t,6),
                F_UDMI(f,t,9), F_UDMI(f,t,10));
                fprintf(fp2,"%g , %g , %g , %g",
                F_UDMI(f,t,11), F_UDMI(f,t,22), F_UDMI(f,t,12),
                T_F(f,t));

                /* reset iteration counter for each layer */
                F_UDMI(f,t,23) = 0;
           }
           end_f_loop(f,t)
           fprintf(fp2,"\nEnd time step\n");

           /* assign time step increment according to changes in
           model regimes (smaller time steps near/during regime
           changes and slagging conditions)   */
           previous_time = current_abs_time;
    if(count_regime2 >= faces_total)
    {
       if(count_regime3 > 0)
       {
           if(count_regime3 >= faces_total)
               current_abs_time = current_abs_time + 900;
            else
            {
                current_abs_time = current_abs_time + 60;
            }
     }
     else
     {
        current_abs_time = current_abs_time + 60;
     }
}
else
{
    current_abs_time = current_abs_time + 60;
}

    Message("\nCheck: count_finish value is %i", count_finish);
    if(count_finish >= faces_total)
    {
      /* entire deposit has formed, steady slagging conditions
      reached and the
      current time will stop incrementing */
      count_all = 5;
      Message("\nFull model has been built.  Time progression
      has stopped.");
    }
    else
    {
          /* the current time has been incremented and the ash
          layer surface temp
         will be recaclculated (return back to Tsur
         calculations)  */
            count_all = 3;

     }
```

```
      /*Message("\nCheck: current time incremented to %i",
      current_abs_time); */
      fclose(fp2);
}

if(count_all == 5)
{
      fp2 = fopen("ashUDFresults-time.txt","a");
      fprintf(fp2,"\n**The full model ash layer results are-\n");
      fprintf(fp2,"\nmodel y , abs y , abs x , ");
      fprintf(fp2,"flux , model t part , model t sint , model t
      sint only , ");
      fprintf(fp2,"model t frozen total , model t slag , model t
      total , ");
      fprintf(fp2,"model time part , model time sint , ");
      fprintf(fp2,"model time total , model T4");

      Message("\nFull model cacluations have been completed. Data
      will now be written to \"ashUDFresults-time.txt\"");
      begin_f_loop(f,t)
      {
            fprintf(fp2,"\n%g , %g , ", F_UDMI(f,t,7),
            F_UDMI(f,t,8), F_UDMI(f,t,24));
            fprintf(fp2,"%g , %g , %g , %g , ", F_UDMI(f,t,4),
            F_UDMI(f,t,13), F_UDMI(f,t,14), F_UDMI(f,t,15)) ;
            fprintf(fp2,"%g , %g , %g , ", F_UDMI(f,t,22),
            F_UDMI(f,t,3), F_UDMI(f,t,16));
            fprintf(fp2,"%g , %g , ", F_UDMI(f,t,17),
            F_UDMI(f,t,18));
            fprintf(fp2,"%g , %g , ", F_UDMI(f,t,19),
            F_UDMI(f,t,2));
      }
      end_f_loop(f,t)

      fprintf(fp2,"\nAbove results from given data:");
      fprintf(fp2,"\nT1=%g, \nTsint=%g, \nTslag=%g", temp_one,
      temp_sint, temp_slag);
      fprintf(fp2,"\nTinf=%g, \nmass flux=%g, \nsigma=%g",
      temp_inf, mass_flux, sigma);
      fprintf(fp2,"\nemissivity_particulate=%g,
      \nemissivity_sint=%g, \nemissivity_slag=%g",
      emissivity_particulate, emissivity_sint, emissivity_slag);
      fprintf(fp2,"\nconvection vel=%g, \nk part=%g",
      convection_vel, k_particulate);
      fprintf(fp2,"\nk sint=%g, \nk slag=%g, \nk gas=%g, \nroe
      part=%g", k_sint, k_slag, k_gas, roe_particulate);
      fprintf(fp2,"\nroe sint=%g, \nroe frozen=%g, \nroe slag=%g,
      \nroe gas=%g", roe_sint, roe_frozen, roe_slag, roe_gas);
      fprintf(fp2,"\ny part=%g, \ny sint=%g, \ny slag=%g,
      \n*mu_slag_avg=%g, \nEND", y_particulate, y_sint, y_slag,
      mu_slag_avg);
      count_all = count_all + 1;
      fclose(fp2);
      Message("\nAll model data has been writen.");
}
```

```
      /*Message("\nCheck: Sixth count_all value is %i\n", count_all);
      */
      if(count_all == 6)
            Message("\nSURFACE TEMPERATURE UDF PROGRAM ITERATION IS
            COMPLETE\n.");

}

DEFINE_PROFILE(centerline_temp,t,i)
{
      face_t f;
      num_faces = 0;
      begin_f_loop(f,t)
      {
            num_faces = num_faces + 1;
            num_2 = centroid_array[1];    /* holds previous
            centroid_array[1] value */
            F_CENTROID(centroid_array,f,t);     /* centroid_array[]
            gets assigned here      */
            if(num_faces == 1)
                  num_1 = centroid_array[1];
            num_1 = centroid_array[1];
      }
      end_f_loop(f,t)
      faces_total = num_faces;

      /* determine FLUENT's calculation sequence      */
      if(num_2 < centroid_array[1])
      {
      case1 = 1;              /* face calculations from bottom up */
            /* Message("\nFluent face calculations are from bottom
            up.");      */
      }
      else
      {
            case1 = 2;              /* face calculations from top down
            */
            /* Message("\nFluent face calculations are from top
            down."); */
      }

      /* Message("\nBoundary faces numbered: there are %i faces",
      faces_total); */
      temp_bottom = 2000;
      temp_top = 1700;
      increment = (temp_bottom - temp_top)/faces_total;
      count = 0;

      begin_f_loop(f,t)
      {
            if(case1 == 1)
                  F_PROFILE(f,t,i) = temp_bottom - count*increment;
            else
                  F_PROFILE(f,t,i) = temp_top + count*increment;
            temp = F_PROFILE(f,t,i);
            count = count + 1;
```

```
            /*Message("\nAssigned temperature is %g and face thread is
            %i",temp, t); */
      }
      end_f_loop(f,t)

      Message("\nCheck: temperatures assigned to center boundary;
centerline UDF complete.");
}
```